

Dissertation zur Erlangung des Doktorgrades
der Fakultät für Chemie und Pharmazie
der Ludwig-Maximilians-Universität München

3D Particle Tracking

in

Cellular Systems

Yoshihiko Katayama

aus

Wiesbaden

2008

Erklärung

Diese Dissertation wurde im Sinne von §13 Abs. 3 der Promotionsordnung vom 29. Januar 1998 von Herrn Prof. Don C. Lamb betreut.

Ehrenwörtliche Versicherung

Diese Dissertation wurde selbständig, ohne unerlaubte Hilfe erarbeitet.

München, am

Yoshihiko Katayama

Day of submission: 21.11.2008

1st referee: Prof. Don C. Lamb

2nd referee: Prof. Achim Hartschuh

Day of oral exam: 12.12.2008

”It is your mind that creates this world”

Buddha

Abstract

The observation of particle dynamics in three dimensions is a growing field in fluorescence microscopy. To reveal the mechanisms behind biological processes in a volume, ingenious and sophisticated methods have to be applied.

In the first part of this work, a newly developed three-dimensional tracking microscope will be presented. Its power lies in the ability to track fluorescent particles during measurement. Based on confocal microscopy, the vicinity of the tracked particle scanned with the laser. Then, through a fast intensity analysis, the particle position is determined. Furthermore, the re-centering of the investigated volume adjusted according to the measured particles position is being used to refocus an additionally attached widefield setup, which can be used to observe the surroundings of the particle. The system has been tested and applied on fast microtubular movement of endosomes. Additionally it was tested for refocussing capabilities on slow artificial movement of whole cells.

The second part, in cooperation with Susanne Lange from the group of Prof. Jansen, deals with the co-transport of mRNA particles in budding yeast. With a commercial *spinning-disc confocal microscope* (SDM), the mechanism of mRNA localisation in *Saccharomyces cerevisiae* was revealed. Different localising mRNA species are packed into common packages to become transported to the bud, a protrusion of the cell where the progeny develops. For the first time it was shown with 3D live-cell imaging that the cell utilises single versatile vehicles to ensure proper mRNA distribution.

The third part, in cooperation with Lily Wang, from Prof. Nigg, the involvement of *Plk1-Interacting Checkpoint Helicase* (PICH) during chromosome segregation in mitotic HeLa cells. The outstanding resolution properties of the SDM enabled live-cell observation of dividing cells in meta- and anaphase and resolved the faint signal from PICH associated DNA threads invisible to common microscopy. The results uncovered that separating sister chromatids were connected by PICH associated DNA threads until anaphase which affirms the role of PICH in proper chromatid segregation.

Contents

Abstract	i
Table of Contents	iii
List of Figures	vii
List of Tables	ix
1 Introduction	1
2 Theory and Basics	3
2.1 Introduction to Fluorescence	3
2.1.1 Fluorescence Properties	4
2.1.2 Dyes	6
2.2 Introduction to Microscopy	8
2.2.1 Lenses	10
2.2.2 Objectives	10
2.2.3 Dichroic Mirrors and Filters	12
2.2.4 Detectors	14
2.2.5 Lasers	15
2.2.6 Beam Steering Devices	16
2.2.7 Heaters	16
2.3 Microscopy Techniques	16
2.3.1 Brightfield Microscopy	17
2.3.2 Widefield Illumination Microscopy	18
2.3.3 Confocal Microscopy	21
2.3.4 Additional Microscopy Techniques	22
2.4 Cell Biology and Biochemistry	22
2.5 Data Acquisition	23
2.6 Introduction to the following Chapters	24

I	The 3D Orbital Tracking Microscope	25
3	Introduction to part I: Tracking Microscopy	27
4	Basics: Tracking	29
4.1	Tracking	29
4.2	Particle Movement: Diffusion and Transport Mechanisms	30
5	Methods:	
	Two Confocal Pinhole Tracking with Simultaneous Widefield Imaging	33
5.1	Confocal Scanning	33
5.1.1	XY-Tracking	33
5.1.2	Z-Tracking	35
5.2	Simultaneous Widefield Observation	35
5.3	Optical Design	36
5.4	Technical description	39
5.4.1	Confocal Beampath	39
5.4.2	Widefield Beampath	40
5.5	Design of the Computerised Control	41
5.6	Selected Custom Programs	42
6	Calibration and Characterisation	45
6.1	Alignment	45
6.1.1	Spatial Calibration	46
6.1.2	Synchronisation	53
6.1.3	Calibration Curve for spatio-temporal correction	56
6.2	Setup Characterisation	57
6.2.1	Tracking Speed and Accuracy	59
7	Applications	61
7.1	Endosome Tracking	61
7.1.1	Cell Culture and Sample Preparation	62
7.1.2	Experiment	63
7.1.3	Results	63
7.2	Focus Readjustment	65
7.2.1	Experiment	65
7.2.2	Results	66
8	Outlook	69
8.1	Software Improvements	69
8.2	Hardware Improvements	70

II	mRNA Transport in <i>Saccharomyces cerevisiae</i>	73
9	Introduction to part II: mRNA Transport	75
10	Theory: mRNA Transport	77
10.1	Cell Biology	77
10.1.1	Gene Expression	78
10.1.2	mRNA Targeting	78
10.1.3	DNA Transformation	78
10.2	Microscopy	79
10.2.1	Spinning Disc Confocal Principle	80
10.3	Image Stacking	81
10.4	Microscope Setup	83
10.5	Data Acquisition	84
11	Experiment: mRNA Tracking in <i>Saccharomyces Cerevisiae</i>	87
11.1	mRNA	87
11.2	Tagging	88
11.3	Cloning	89
11.4	Image Analysis	89
12	Results	91
12.1	mRNA Tagging with MS2 and boxB	91
12.2	Localisation	93
12.3	Colocalisation	94
12.4	mRNA Transport	95
12.5	The Influence of Unmatured RedStar RFP	97
13	Summary and Outlook	99
III	PICH Dynamics during Meta- and Anaphase	101
14	Introduction to part III: PICH	103
15	Theory: Chromosome Segregation	105
15.1	Mitosis	105
15.2	Cohesin and DNA Catenation	106
15.3	PICH	107
16	Experiment:	

Table of Contents

PICH Dynamics in Metaphase	109
16.1 Setup	109
16.2 Cell Biology	109
16.2.1 Cell Preparation	110
16.3 Image Acquisition	110
16.4 Analysis	110
16.4.1 Gaussian Blur Filter	111
16.4.2 Kalman Stack Filter	111
17 Results	113
17.1 Chromosome Separation	113
17.2 PICH colocalises with centromere DNA	115
17.3 The dynamics of PICH associated threads	116
17.4 PICH in Walker A mutant deficient cells	116
17.5 Supplementary biochemical results	117
18 Outlook	119
19 Summary and Conclusion	121
Bibliography	127
Appendix	129
Confocal Tracking Microscope	129
Spinning Disc Microscope	132
Dyes	132
Bio	134
List of Software and Programs	134
Abbreviations	137
Publications	139
Acknowledgements	141

List of Figures

2.1	Jablonski scheme for Luminescence	5
2.2	Structures of Different Fluorophores	7
2.3	Numerical Aperture	11
2.4	Airy discs	13
2.5	Transmission and Epi Illumination	17
2.6	Difference Interference Contrast Schematic	18
2.7	Köhler Principle	19
2.8	Confocal Beampath	21
4.1	Types of Diffusion	31
5.1	Tracking Routine	34
5.2	Pinhole Arrangement for z-Scanning	36
5.3	Tracking Microscope Setup	39
6.1	Autocorrelation Function of Properly Aligned Pinholes	47
6.2	Autocorrelation Function of Misaligned Pinholes	48
6.3	Physical Angle	49
6.4	Focal Intensity Distribution for Different Beam Diameters	50
6.5	Raytracing with Matrix methods	51
6.6	Rays in Shifted Pinholes	51
6.7	Calculation for Mirror-Based Beam Positioning	54
6.8	Track Meander- and Circletrajectory	54
6.9	Confocal and Widefield Image Comparison	55
6.10	Calibration Curves for z	57
6.11	Axial Moving Bead in Widefield	58
6.12	Trajectory Post-analysis	59
6.13	Dynamical Tracking Accuracy	60
7.1	Programs: msdGuide and Slider	63
7.2	Particle Transport along Microtubules	64
7.3	msd-Plot over Trajectory	65

List of Figures

7.4	Trajectory of a Cell Movement	66
7.5	Cell Tracking of Axial Movement	68
10.1	Spinning Disc Confocal Principle	81
10.2	Images obtained with Widefield and Confocal	82
10.3	Image Stack	83
10.4	Spinning Disk Setup	84
12.1	<i>ASH1</i> with Tag Sequence	93
12.2	<i>IST2</i> with Tag Sequence	93
12.3	Trajectory of a mRNA Localisation	96
12.4	Crosstalk Issue	97
15.1	Cellcycle	106
17.1	Chromosome Segregation	114
17.2	Ripping PICH Thread	115
17.3	PICH-Centromer Colocalisation	116
17.4	PICH thread dynamics	117
17.5	Walker A mutant	118
19.1	Filter Confocal Tracking	131
19.2	Filter Widefield Tracking	131
19.3	Filters used for part II	133
19.4	Filters used for part III	133

List of Tables

12.1 mRNA constructs with MS2	92
12.2 mRNA constructs with λ -pep	92
12.3 Results	94
19.1 Technical Equipment Confocal Tracking Microscope	129
19.2 Filters used for Confocal Tracking Microscope	130
19.3 Technical Equipment for Spinning Disc Microscope	132
19.4 Filters used for Spinning Disc Microscope	132
19.5 Fluorescent Probes and Samples	132
19.6 Consumables: Biochemistry and Cell Biology	134
19.7 Software and Programs	134

CHAPTER 1

Introduction

Research of biological samples on the nanoscale is a growing field in science. To observe and understand the processes which lie behind interactions between biological molecules constitutes the motivation of researchers all over the world. Because the structures are often smaller than the smallest resolvable distance in optical microscopy, it is difficult to visualise them. One method is to use smaller wavelengths like in electron microscopy. Here, the structure is nicely resolved within a few Ångströms. A major disadvantage of electron microscopy though is the sample preparation which alters the sample in a way that all dynamic is disabled and thus any biological information except its structure is lost. Another promising approach is to attach a marker to the particle of interest which can be seen by light microscopy. In fluorescence microscopy those markers can be stimulated to emit a photon by strong light sources such as lasers. The emitted photons can subsequently be collected by sensitive detectors and its signal further analysed. Since the particle itself is only moderately altered by the labelling, the natural behaviour is conserved in many cases. This makes fluorescence microscopy a preferential choice for investigating dynamics in biological samples.

Numerous sophisticated microscopy methods constitute the tools to solve biological mysteries. However, there is not one ideal setup but many different ones, each optimised for a specific problem to obtain as much information as possible out of an experiment. This work focusses on visualising particle trajectories within the cell in three dimensions.

In this thesis, a novel elaborated microscopy method has been developed and tested. Its power lies in the ability to track fluorescent particles in three dimensions with a spatial resolution of some tenths of nanometers and within a reaction time of few milliseconds while simultaneously imaging the biological structure of the surroundings of the observed particle. The technique of the tracking is based on confocal laser scanning microscopy (LSM), however, the laser is moved in an orbit around the particle to determine the xy position of the target particle. Furthermore, the principle of the confocal

pinhole is utilised on two concurrent confocal beampaths to calculate the position of the particle along the optical axis z . In doing so the particle is trapped inside the observed volume, which can be as small as the *Point Spread Function* (PSF), which determines the smallest resolvable distance. As the objective follows the movement, the second part of the setup, an epi-fluorescence microscope, is automatically kept in the focal plane of the tracked particle. Secondary structures can then be visualised to relate the particle to the surrounding structure.

Rapid particle tracking is not the only method which can be applied with this system. Due to its refocussing capabilities, it is possible to apply the system for time-lapse measurements of several hours, where conventional microscopes fail to keep the focus on cells that are moving. Common refocussing techniques use the glass coverslip as the frame of reference. However, if the cellular system moves relatively to the cover slip, the setup loses track of those cells. Especially in large cell clusters like embryonal cells or neuronal networks, it is a way to re-adjust the focus onto the sample itself. The only prerequisite is that the sample has to be labelled with a fluorescent dye that is detectable by the tracking routine.

Three dimensional tracking can also be done using other techniques. The second topic of this work is z -stacking done on a commercial spinning-disc microscope (SDM). Used for sensitive measurements this is a versatile tool to rapidly acquire z stacks with greater temporal and spatial resolution than with widefield microscopy. Through subsequent image processing, three dimensional dynamics of dim samples can be revealed. The SDM was used to reveal the transport mechanisms lying behind mRNA localisation in budding yeast. In collaboration with Susanne Lange from the Jansen group at the Genecenter in Munich, mRNA particles tagged with two different fluorophores were continuously observed during their journey to the bud.

The SDM also proves to be a versatile observing system, where the movement of an entire structure is of interest as it can be seen during cell division. In collaboration with Lily Wang from the group of Nigg at the Max-Planck-Institute for Biochemistry, faint signals of fusion proteins were collected to elucidate the dynamics of proteins involved during mitosis. The accuracy and the sensitivity of the setup is brought to the limits of current three-dimensional imaging techniques to visualise PICH associated DNA threads connecting segregating chromosomes until late anaphase.

CHAPTER 2

Theory and Basics

2.1 Introduction to Fluorescence

Looking at the bewitching glow of fireflies at nightfall or the gleaming surf caused by marine species, one witnesses the biological evidence of a phenomenon known as luminescence. Mentioned by the Chinese in *Shin Ching*, the *Book of Odes*, 1500 to 1000 BC, by Thales of Miletus later cited by Aristotle and also by pre-Hispanic Aztec doctors, as literature from Spanish missionaries suggests, nature has evolved the ability of light emitting molecules in bacteria, fungi, algae, invertebrate animals, fish and insects. However, it was not until 1852 when the phenomena of fluorescence was thoroughly explained by Sir George Gabriel Stokes, who also coined the name of fluorescence [53]. He discovered that fluor spar and uranium glasses absorb light and become themselves a source of light radiation. He also recognised that the spectra of the emission was shifted towards lower energies, i.e. longer wavelengths compared to the excitation spectra. This property is now known as the *Stokes shift* in his honour. In 1913, Niels Bohr introduced a model which could explain the emission lines of the hydrogen atom [7]. He described the atom as a heavy nucleus, where the protons and neutrons are confined and electrons orbiting the centre at defined distances. He concluded that the discrete structure of the electron orbits were the reason for the spectral lines as the electron can only switch between discrete energy states. The absorption and the emission spectra are therefore defined by the energy landscape of the electrons. It was later James Franck who investigated how molecules could dissociate by photon-induction and gave an explanation with electron transition probabilities [16]. Edward Condon extended his theory to general band transitions independent from photon transitions [10]. From their discoveries, the *Franck-Condon principle* was derived, which directly relates the intensity values of the spectrum to the transition probabilities. The energy of the absorption is not necessarily given from a single photon, but as Maria Göppert-Mayer suggested in her dissertation in 1931 [19] also from two or more photons. She developed her theory under the supervision of Max Born out from Dirac's theory of radiation. The processes involved

in absorption and emission were visualised by Aleksander Jabłonski in 1935 when he introduced his model of energy states of a fluorescent chromophore, i.e. fluorophore [25]. The electrons of the molecule become excited to higher electronic states upon absorption and eventually relax, by dissipating the energy through the emission of a photon. This energy scheme of transition processes is named *Jablonski-scheme* from which one can derive the wavelengths according to the energy differences of the transition (Figure 2.1). Then in 1948 Theodore Förster [17] described the non-radiative energy transfer between molecules. Depending on the distance between two molecules, an excited molecule can transfer its excitation energy to a second molecule without transmitting a photon. A high interest in fluorescence was exhibited in the second half of the 20th century. With the invention of the laser by Arthur L. Schawlow and Charles H. Townes [49], the phenomenon of fluorescence was better accessible to scientific studies. So was Göppert-Mayer's prediction of two-photon excitation finally experimentally verified on europium-doped crystals by Wolfgang Kaiser and C.G.B. Garrett in 1961 [27]. Later, fluorescent probes emanated especially into the field of microbiology. A year after the experimental evidence of the two-photon excitation, Osamu Shimomura, Frank H. Johnson and Yo Saiga published the first isolated fluorescent protein of the jelly fish *Aequorea victoria* and described which part of the protein was fluorescing [52]. The name of the protein is the famous *Green Fluorescent Protein* (GFP). It took some decades until 1995 when Roger Tsien together with Roger Heim and Andrew B. Cubitt made mutants to GFP so that more fluorescent proteins with improved fluorescence properties or different spectra [21]. In 2008, Shimomura, Chalfie and Tsien were awarded the nobel prize in chemistry for the discovery and development of the green fluorescent protein, GFP. This boosted the application of fluorescent fusion proteins and now biological research without it is unimaginable.

2.1.1 Fluorescence Properties

Photoluminescent objects emit electromagnetic radiation where the energy of the emitted photons doesn't solely come from the temperature of the luminescent object but from absorbed photons prior to emission. The energy transition probabilities can be explained with the *Franck-Condon principle*. Two kinds of photoluminescence processes are known which are distinguished through their time span between absorption and emission.

The first effect is *phosphorescence*. Here, the time between absorption and emission is in the range of milliseconds or longer. The energy of the absorbed photon is transferred to a triplet state T by a process called intersystem crossing where the transition from the triplet to the ground state is quantum mechanically forbidden due to the spin configuration of the states. The spin of the excited state is flipped relative to the ground state. A small momentum transfer triggers a spin flip and enables the electron to escape from its trapped state via emission of a phosphorescence photon.

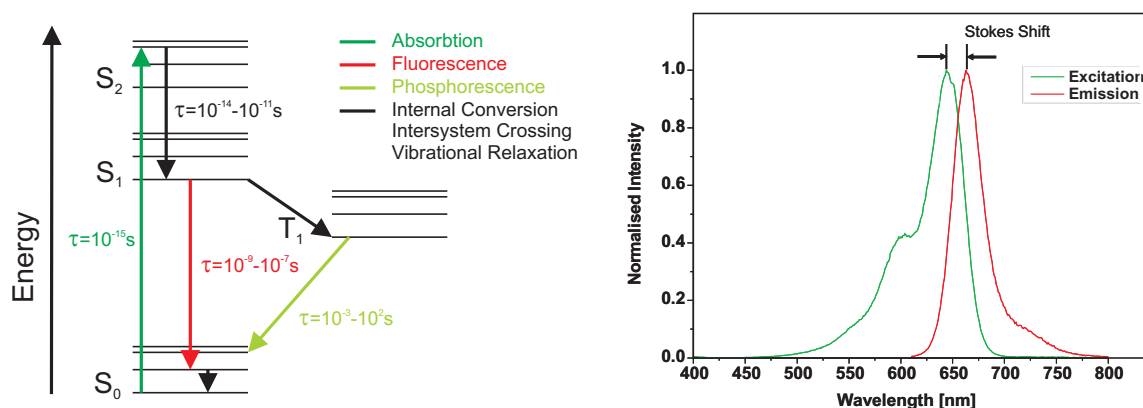


Figure 2.1: Jablonski-Scheme clarifying luminescence, Cy5 excitation and emission spectrum; The distance between both excitation and emission maxima is known as *Stokes Shift*.

In the more common phenomenon, an absorbed photon is exciting the molecule from the ground state S_0 into a higher electronic state, e.g. an excited singlet S_1 . Within picoseconds it relaxes from vibrational states. Because this singlet state has, unlike the triplet state, the same multiplicity as the ground state it can relax to the ground state, usually on the nanosecond timescale. This radiation is called *fluorescence*. Figure 2.1 left panel shows a *Jablonski Scheme* and illustrates processes of fluorescence and phosphorescence. The scheme on the right hand side shows the excitation and emission spectra of Cy5. The spectral shift between the maxima is called *Stokes shift* and results from the reduction of the available energy for the photon transition due to vibrational relaxations.

The Stokes shift is utilised to distinguish photons used for the excitation from those who originate from the emission. Unlike filters, which block certain parts of the spectra, dichroic mirrors can be applied to separate the spectrum at a given wavelength. Especially the utilisation of lasers has been proven to be extremely useful for fluorescence application. Since lasers have a sharp emission spectrum, they can easily be separated via filters and dichroic mirrors. Nowadays the tendency is to use several dyes simultaneously labelling different particles. However, the more dyes are used the higher is the possibility of the *spectral crosstalk*. The crosstalk is usually not beneficial as the emission spectra of different dyes overlap and therefore the detected photons become indistinguishable. Dyes for optical microscopy have typically an emission spectra in the visible range between approximately 450nm to 750nm. Emission spectra are typically 100nm broad, thus only up to three dyes can be used simultaneously without significant overlap. The closer the spectra of different dyes are to another, the more spectral crosstalk they will have.

2.1.2 Dyes

The spectrum of a dye is a property from which the dye is chosen for an experiment. The maximum of the excitation spectrum is chosen according to the excitation laser, while the Stokes shift is used to separate excitation from emission. However, there are more criteria to consider when choosing the best suitable dye. The quantity which describes the amount of the absorbed light in a solution is the *extinction coefficient* which is derived from the *Beer-Lambert Law*. The *quantum yield* is a value which describes the fluorophore's ability to re-emit a photon after absorption. The higher the quantum yield, the less laser power is needed for the experiment and thus less energy will be deposited into the sample which can possibly degrade it. It also has to be considered, how regular the fluorophore emits its total amount of emitted photons. The blinking behaviour of the sample is important for the experiment insofar that blinking events can disturb a continuous observation of the sample, especially when the dynamics of the sample itself occur on a similar timescale. A very important aspect is the lifetime of the sample (not the excited state), or in other words the time the sample is able to fluoresce before bleaching, which is denoted as *photostability*. Common fluorophores degrade after a certain time. The number of photons emitted from a fluorophore until it is bleached can be determined and has to be scrutinised before the experiment. For biological experiments, it is moreover necessary to understand how the dye can be functionalised and linked to the molecule of interest. And of course at the same time, it must not alter the molecule and the surrounding environment, i.e. by toxicity or functional changes. There are in general four sources of fluorescence in biological experiments:

1. Chemical Dyes
2. Fluorescent Proteins
3. Qdots
4. (Intrinsic autofluorescence)

Chemical Dyes are synthetic fluorophores based on organic molecules, where the π -electrons are delocalised and can move relatively freely in the molecule. Prominent examples of these type of fluorophores are DAPI, Rhodamine 6G or the dyes from the Cyanine or Atto family. The structure of DAPI, a DNA marker, Rho 6G, also used as dye-laser medium, and Cy5, whose family is also used for CD-R media, are shown in figure 2.2.

Fluorescent Proteins have their origin in animals that can emit light in a dim environment and are constituted from naturally occurring amino acids. Fluorescent proteins can be found in bacteria, insects, or sea animals. The proteins are also called fusion proteins, since they can be fused to other biological structures in the cell. Several different fluorescent proteins in different spectral ranges have been engineered to suit the

high demands of biologists. Its versatile application range in biology have resulted in the Nobel prize award in 2008 for those, who discovered and modified the proteins. The advantage of these proteins is that once the genetic code of the protein is shuttled into the nucleus via plasmids, the cell itself produces the construct, thus the environment is rather non-artificial. That means, that since the particle is naturally attached to a specific target, no specific linkers, as it is needed for synthetic dyes, have to be designed. From the first sequenced protein GFP, the prominent eGFP protein is derived. Moreover, there are other chromophores such as dsRed, mCherry or YFP, which in general differ in their inner structure of the core. Figure 2.2 shows GFP with a closeup to the inner fluorescent core. The work on fluorescent proteins was rewarded with the Nobel prize in chemistry in 2008.

Qdots are the most recent developed fluorescent molecules. The fluorescence obeys the laws of quantum mechanics and results from an electron confinement in a semiconducting structure (CdSe or CdTe with ZnS). The confinement defines the dimensions of the electron wavefunction and hereby the colour of the emission. The photon emission cannot be explained by π -electrons as for organic molecules but with the band structure of the semiconductor. The advantages of qdots are a sharp emission line of some

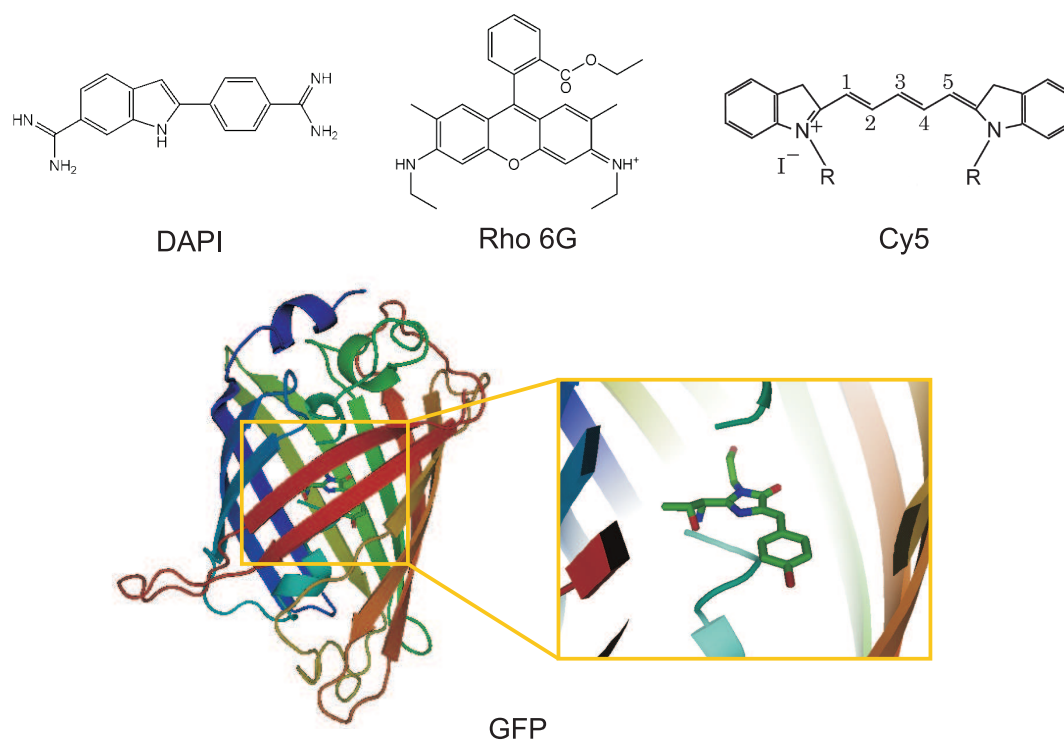


Figure 2.2: Structure of three chemical dyes and GFP with a close-up to the fluorescent core [43]

nanometers and remarkable stability. However, they have to be functionalised since the semiconducting material is highly toxic not water soluble and usually show strong blinking behaviour.

The **autofluorescence** of cells has been known since the beginning of the 20th century. It is a natural property of many components of a cell to fluoresce after excitation particularly in the UV range, but can also be excited with longer wavelengths. The emission spectra goes throughout the visible range and often causes difficulties for ultra-sensitive measurements. Accentuated in stressed cells or in *fetal calf serum* it is therefore mostly an unwanted side-effect of fluorescence experiments in cellular research.

2.2 Introduction to Microscopy

The human eye is an exceptional optical detector and is versatile far beyond the reach of artificial products. The human oocyte with a size of little more than $100\ \mu\text{m}$ about the diameter of the human hair, can still be seen by the naked eye. Going below $100\ \mu\text{m}$, it becomes more and more difficult for an unaided eye to resolve structures and the limit is reached at some tenths of microns. Since the oocyte is one of the larger cells, it was necessary to invent tools to enhance the potential of the eye to observe the small world. The application of magnifying lenses is doubtless an old tool which can be dated back to the civilisations in Egypt and Mesopotamia. The early lenses were made of transparent rocks which bend the light beam. However, the theory of how lenses manipulate the ray track was yet unknown. First empirical theorems were recorded by the Greek Euclid around 300 BC. From him we know about euclidian geometry and provides the basis for geometrical optics. It took another millennium until thorough theories were given by Arab scholars. In the year 984, Ibn Sahl derived the laws of refraction which are later to be known as Snell's law. The first aspheric lens design can be accounted to him as well. The special shape of these lenses minimises the spherical aberrations compared to conventional lenses. Considered as the father of optics is Ibn al-Haytham. His *Kitab al-Manazir*, the book of optics, inspired many future scientists. More and more optical lenses were appearing in the 11th century and were later improved by making them out of glass from the 13th century on. The invention of the microscope is accredited to two dutch lens grinders Hans and Zacharias Janssen dating 1590. A double lens system was used to observe objects too small to be seen with the naked eye. Three decades later in 1625, Giovanni Faber coined the name 'microscope' in analogue to the telescope. Later in the 17th century, Robert Hooke was the first to consider immersion media. Antony van Leeuwenhoek investigated biological samples with the microscope, when finally the cell was accepted to constitute the general substructure of biology. However it was not until

the first half of the 19th century that it was recognised that the fundamental element of any living organism is the cell.

Pioneering work in the field of microscopy was made by Ernst Abbe in 1873. Before Abbe, microscopy design was a matter of trial and error. His accomplishment was to put microscopy on a theoretical foundation. Together with August Köhler, Otto Schott and Carl Zeiss, they produced many innovations in microscopy which had their origin in Jena; New types of lenses based on new glasses, new illumination techniques and a systematic arrangement of the optical path to enhance the image quality. In 1904, August Köhler presented a UV microscope with objectives specially made for the UV region by Moritz von Rohr [23]. As UV light is very energetic, the first autofluorescent samples were discovered. First seen as an annoyance, it was the beginning of fluorescence observation with a microscope. Later, microscopes were build solely for this purpose and in 1911 Bruno Johannes Stübel reported the first experiment on autofluorescence in cells [54]. For the excitation source, a common arc lamp was used. In the following centuries, the basics of the microscope design changed very little. The arrangements of the optical parts varies with the special purpose of the application. In 1960, Theodore Maiman revolutionised science and technology by expanding the existent Maser to the spectrum of visible light: He build the first working laser [38]. Without the invention of the laser, many ground-breaking developments of the last decades are unimaginable. Beside in microscopy it led to the invention of stage-scanning confocal microscope in 1960 by Marvin Minsky. Without the laser it was hardly possible to produce an intensive light to minimise the acquisition to a reasonable time scale. The principle of a confocal microscope is to illuminate a small spot in the sample and to use a detection pinhole to significantly reduce scattered light which would otherwise blur the image. To obtain an image the sample has to be scanned. Another sophisticated method, the two-photon microscope was introduced in 1990 by Winfried Denk, James Strickler and Watson W. Webb and is another effective method for reducing stray-light and to investigate samples deep inside a tissue [13]. Finally, a recent development is *Stimulated Emission Depletion* (STED). Stefan Hell and Jan Wichman developed a method to image fluorescent particles with subdiffraction-limited precision [22], which finally was experimentally proven in 2000 by Stefan Hell together with Thomas A. Klar, Stefan Jakobs, Marcus Dyba and Alexander Egner [33]. The principle is to use phase plates to shape a pulsed laser beam, which is then used to stimulate the fluorophores in close vicinity of the focal spot to relax with a photon of lower wavelength. That photon is filtered out.

Microscopy on biological samples now exhibits numerous applications where fluorescent molecules are used as markers for small structures even below the limit of diffraction. In order to apply fluorescence microscopy, a thorough knowledge of the system to be observed and the microscope is needed. For this reason the next pages will give a brief introduction to the parts of a fluorescence microscope.

2.2.1 Lenses

Achromatic doublets are used for our setup. They consist of two lens elements and have enhanced optical properties. The achromatic doublets correct for chromatic and spherical aberrations. This is beneficial to the quality of the beam in comparison to singlets. Further advantages range from a smaller focus spot to better off-axis performance. The set-up of the lenses is assured by aligning the incoming beam so that it passes the lens in the central region. Also, the beam should hit the lens perpendicular to its surface. Otherwise, the beam quality is reduced as off-axis rays show increased aberrations. To prevent backscattering, the lens can be coated with an anti-reflective coating. To further reduce backscattering the lens shows the side to the incoming beam, which generates the largest reflection angle compared to the incident beam: The flat shaped facing the focussed beam, the round shape facing the collimated beam. Nevertheless, the reflection is visible, which however is advantageous for adjusting the lens especially for angular placement. Also this set-up of the lenses is advisable, to divide the refraction to both sides of the lens, during entering and exiting.

2.2.2 Objectives

The objective lens is the heart of the microscope setup and comes closest to the sample itself. The tremendous requirement on its optical quality is obvious since it is often the most expensive part of the microscope. The choice of the correct objective is important to ensure the best transmission and also to minimise typical lens errors such as *spherical* or *chromatic aberrations* for all wavelengths. The design of the correction is usually made on three reference wavelengths (in modern objectives up to four reference wavelengths) in the visible range. Any deviation, especially at the boundaries of the visible spectra, results in an increased aberration. For single molecule experiments, an increased transmission quality is preferred. Some materials are preferential in terms of transmittance which is also dependent on the working wavelengths. Another feature of current objectives are correction collars, which take into account different coverslide thicknesses as well as for different temperatures. Often neglected, they drastically enhance the image quality if correctly adjusted.

Numerical Aperture

A major criteria of an objective is its *Numerical Aperture* (NA). While the magnification is taken into account when choosing the right field of view, the NA is the essential factor for photon collection efficiency. It is an inconspicuous value which has nevertheless a huge impact on the performance of a microscope. It is the value which describes the objectives ability to collect light from the sample. The higher the numerical aperture, the larger is the opening angle of the collected light and hence gives higher contrast to the investigated structure for a given magnification.

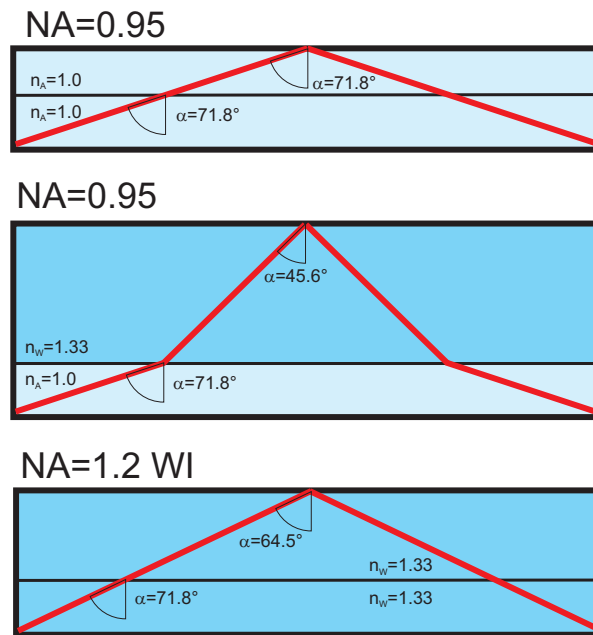


Figure 2.3: The *Numerical Aperture* (NA) describes the opening angle of the light cone which is collected by the objective. Three configurations are shown: An air objective with the lightcone in air-to-air, an air objective with air-to-water and a water objective with water-to-water transition.

$$NA = n_m \cdot \sin(2\theta) \quad (2.1)$$

NA [] : Numerical Aperture
 n_m [] : Refractive Index of the Medium
 α [] : Half of Incidental Angular Aperture

The light cone originating from the objective cannot exceed an opening angle of 180° , which would mean an NA of one for simple microscopes. However, Robert Hooke already realised, that if a sample is in solution it is advantageous to have the same refractive index throughout the detection, which is called refractive index matching. Due to the different speeds of light in different media, the way a light cone travels to reach the objective is determined by the index of refraction of the medium it passes. To increase the angle of the cone one can use an immersion liquid which bends the light cone into the objective guiding more photons into the detector. This is the basic concept of *immersion objectives* and it explains how the value for the NA can in fact exceed 1. Figure 2.3 gives an example of an air objective with an NA of 0.95. For samples in air the cone has an angle of 71.8° . The second image shows what happens, if the same objective is used for an experiment with cells which are typically in solution. Following *Snell's*

Law for reflection, the angle of detection declines to 45.6° . That gives a loss of light by a factor of 2.292x. This refractive index mismatch leads to a significant loss of image quality. To have index matching, a *water immersion* (WI) objective can be used. The third picture gives an example of a typical WI objective with an NA of 1.2. The angle of the light cone becomes 64.5° and gives therefore 1.896 times more light than a high quality air objective. For the case that the refractive index of the immersion is higher than that of the sample the amount of collected light is depth dependent. For objectives with higher NA, the image however becomes subject of significant aberrations especially in deep tissues. The *Point Spread Function* (PSF) changes with higher NA [29].

Resolution and Point Spread Function

If one would like to look upon smaller and smaller structures, the total magnification comes to a limit due to the wavenature of light. Even higher magnification will not result in a gain of information. Every single spot smaller than approximately half of the wavelength of the illumination is diffracted in such a way that its point like behaviour is blurred on the detector to a so-called Airy disc. Because smaller structures also means fainter signal, the resolving power of the setup becomes crucial for the assessment of the microscope. Figure 2.4 shows the Airy disc and an example of either two resolved points or unresolved. However it is possible to measure distances and positions more accurate than Abbe's limit of resolution [41]. Even more it is now possible to overcome this limit in fluorescence microscopy techniques applied in *Stimulated Emission Depletion* (STED), *stochastic optical reconstruction microscopy* (STORM) and *photo-activated localization microscopy* (PALM). The integration times to obtain images for these techniques are in the minimum order of some tenths of seconds. Hence they are not suited for several dynamic processes in cell biology.

2.2.3 Dichroic Mirrors and Filters

Mirrors

An ideal mirror totally reflects the incoming beam based on the laws of reflection. Their characteristics include the spectral range of their application and the flatness of the surface, which can be denoted in fractions of λ 's, as in $\lambda/5$ or $\lambda/10$. On most mirror surfaces, the incident beam experiences a phase shift of π . The substrate is coated with several dielectric film layers similar to the production of filters. A common way to ensure a proper adjustment of the reflection angle is to look at long distances. The further away the observer is, the greater is the influence of the angle on the spatial deviation. A deviation from the ideal beam path can be an angular and a spatial beam deviation. These deviations can be corrected using two subsequent mirrors.

Filters

Today dichroic mirrors or filters in general, are usually made of a quartz glass substrate

on which multiple layers of materials with varying diffractive indices are deposited, e.g. by ion beam sputtering. The coating ensures that only selective wavelengths are transmitted and others are reflected. The principle which lies behind the spectral filtering is the wavelength dependent constructive or destructive interference along the many layers of the substrate. There are two main types of filters. The soft-coated filters consist of many different substrate plates of different coatings which are then laminated with a moisture resistant epoxy. This method opens flexible arrangements of transmission properties. However, the newer hard-coating technique is a more robust type of filter. Those filters are made from only one glass substrate onto which several hundred layers of ion-beam sputtered dielectric materials are deposited. This results in a higher durability and sharper spectral fall and rise. They are resistant to many aggressive chemicals since, in contrary to the soft-coated filters, it consists only of silica and no epoxy layer in between. In addition, they show excellent optical properties, which appear to last for a long time even after high power applications. The anti-reflective coating of this filter type is applied during sputtering and not afterwards. Therefore, there is little concern

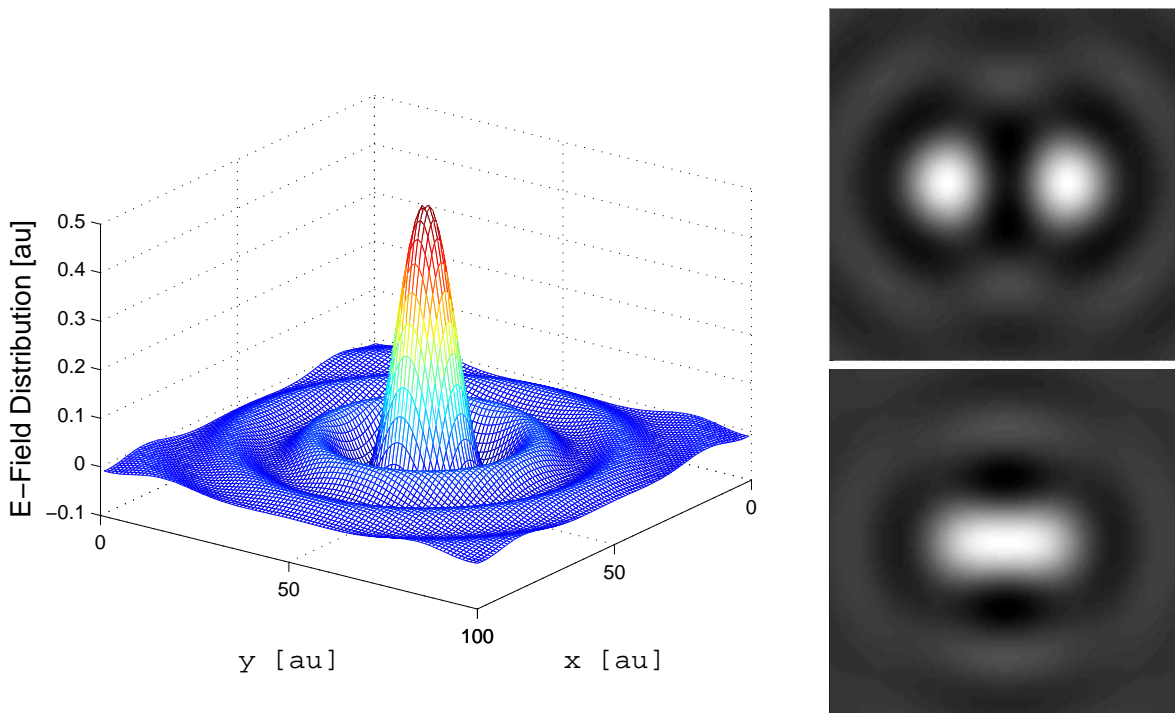


Figure 2.4: The intensity distribution of the radial Airy disc, which is the intensity distribution of a point light structure at the focal plane. For most applications it is regarded that only if the maximum of one Airy disc is at least at the first minimum of the second, two pointlike structures can be discriminated as two and thereby being resolved.

of degradation of the layer starting at the rim of the filters. Good filters have sharp rises or falls at specific wavelengths, high transmission and reflection qualities and have a planar surface. The latter can be improved by choosing a thicker mounting.

Confocal Pinholes

The confocal pinhole is one of the most important elements in a one photon excitation confocal setup. It prevents the off-focus light from entering the detector via spatial filtering and, in turn, spatially restricts the depth of view. This is the reason for the high signal-to-noise (S/N) ratio of confocal images, because it stops straylight from entering the detector giving a nice z resolution in the range of 1 μm . Instead of a confocal pinhole, an optical fibre with a core diameter analogue to the diameter of the pinhole can be used. The size of the confocal pinhole is usually chosen to fit the Airy disc, which is the maximum of the zeroth order of the diffraction pattern until the first minimum. That radius can be approximated to $1.22 \cdot f \cdot \lambda / D$.

2.2.4 Detectors

Detectors are subdivided in two classes of detectors, the point detector and the field detector. The point detector has only a single area which is photo-sensitive in contrary to the field detector. The field detector has an array of point detectors. The choice of the right detector is depend on the application.

An *Avalanche Photo Diode* (APD) is a light sensitive semiconductor which amplifies a single charge created by the absorption of a photon. The APD is essentially a diode working in Geiger mode. A photon entering the detector produces charges in the depletion zone that are accelerated in a strong external electric field. In this zone the field is high enough to transfer enough energy to the electron to produce more electrons via impact ionisation. The following avalanche of charges is finally converted into an electric signal. The APD is extremely sensitive and is useful for very low light applications where single photon detection is needed. During the avalanche generation, the APD cannot detect further photons which is termed as the dead time of the detector, which is on the order of 50ns. The quantum efficiency, a quantity defining the ratio of signal generated per photon, is in the range of 70 to 85%. An intrinsic property of APDs is the so-called afterpulsing. An electron can be trapped in the detector and later released, which produces an additional counting pulse. Additional noise is caused by thermal fluctuations inside the crystal structure of the semiconductor. This noise can be lowered, when the detector is cooled. Good detectors have a low dark current and are chosen from a set of detectors, since the production is not yet fully understood.

A *Charge Coupled Device* (CCD) was first invented by Williard Boyle and George Smith at Bell Labs in 1969 as an electric storage device. It was soon discovered that these

devices have excellent light detecting properties. Another year later, the first CCD chip for light sensing purposes was built. The chip of a CCD is composed of a semiconducting silicon wafer of about $500\ \mu\text{m}$ in thickness. Upon this structure, transparent electrodes are attached on an electrical isolator via lithography. The voltage of these electrodes creates a region of poor charge density, i.e. a potential of the semiconductor close to the isolator. When a photon travels through that region, electrons are released due to the photoelectric effect and transferred from this region to the electrodes. The collected charges are directly related to the number of incident photons and, when the gain is known, the number of photons per electrode or pixel can be calculated. The quantum efficiency for a front illuminated CCD chip is about 45% for red light. An enhancement is made when the wafer is ground to a thickness of 10 to $20\ \mu\text{m}$ and the chip turned to the opposite side. In those cases the quantum efficiency increases to more than 90%. With increasing intensity, the signal can leak into neighbouring pixels which is called blooming. The *Electron Multiplying CCD* (EMCCD) is a CCD with an additional electron amplifier. The amplification is placed between the shift register and the output amplifier. Depending on the gain of the CCD, they can however be used as a photon integrator.

Several noise sources limit the effectivity of detectors. This includes the signal-inherent shot noise, the dark current and the read-out noise. The shot noise results from the poissonian fluctuations of photon emission, which is a general property of every photon source. Since it results from the system itself, the detector can only reach the shot noise limit of the system. The dark current arises from thermal related random generation of free electrons within the sensitive depletion region of the detector and produces additional signal electrons even if no photons are present. This can be measured and simply be subtracted from the signal itself. The dark current has its own noise proportional to the square root of the dark current signal. The dark signal is also multiplied by the gain and has to be considered in the calculation of the signal to noise (S/N) ratio. The more the detector is cooled the better is the performance, since fewer thermal electrons are produced. The read out noise is a property of the electric circuit.

2.2.5 Lasers

The indisputable presence of lasers in science and industry is the proof for the unconditional importance of the technology which has also found its way into microscopy. The unique feature is the emission of coherent light of a specific wavelength at high intensities. Thus, lasers are the ideal light source for fluorescence microscopy. In comparison, arc lamps have broad emission spectra which are restricted by the choice of fluorescence filters. The intensity of an arc lamp can not reach the intensities a laser can provide. Also, laser systems have become more stable and durable than arc lamp systems and are more reliable, which is important for the reproducibility of the results.

2.2.6 Beam Steering Devices

For confocal image acquisition, beam steering devices are needed in order to scan the beam over the sample. The demands on those mechanical components are speed paired with accuracy. For common *Laser Scanning Microscopes* (LSM), galvanometric mirrors are used. The basic principle behind a galvanometric mirror is an electromagnetic motor which applies an angular torque to a cylinder to which the mirror is attached. These galvos operate on just one axis. Special LSMs use the mirror in resonant mode where the mirror is brought into a very high oscillating frequency of tenths of kHz. The common operating mode is typically in the kHz region. The advantage of galvos are the high angular deviation one can achieve simultaneous to the kHz speed. A drawback of galvanometer mirrors is that the pivot point is often not on the mirror surface and there is no feedback loop to test the accuracy of the mirror position. Hereby, piezo-scanners can be applied. The piezo technique is based on a crystal extension sensitive to an applied voltage. The speed is less than for galvo-scanners and special piezo-mirrors can now reach up to 50mrad angular beam deviation. The accuracy is enhanced, since they can have a feedback loop with a capacitive sensor correcting for an accurate positioning. Piezo-scanners can then reach submicroradian accuracy.

2.2.7 Heaters

When working with living cells, a stage heater and an objective heater are integrated into the microscope. They guarantee an experimental environment where cells can grow in a controlled way. The use of CO₂ is also recommended but can be ignored for measurements with CO₂ independent medium which keeps its pH value constant. The temperature can influence the image properties, thus some objectives have correction collars calibrated at room temperature and 37° C, to take into account the different temperatures of the immersion medium.

2.3 Microscopy Techniques

The following section will discuss the methods to illuminate the sample in a way that enhances the quality of the image. Therefore a subdivision between samples is required namely those which change the incident light in their properties and samples, which are selflucent, i.e. fluorescent. Figure 2.5 shows the two possibilities to illuminate the sample. The left image shows a sample observed with transmission light while the right image shows an arrangement, which can be found in epi-fluorescence.

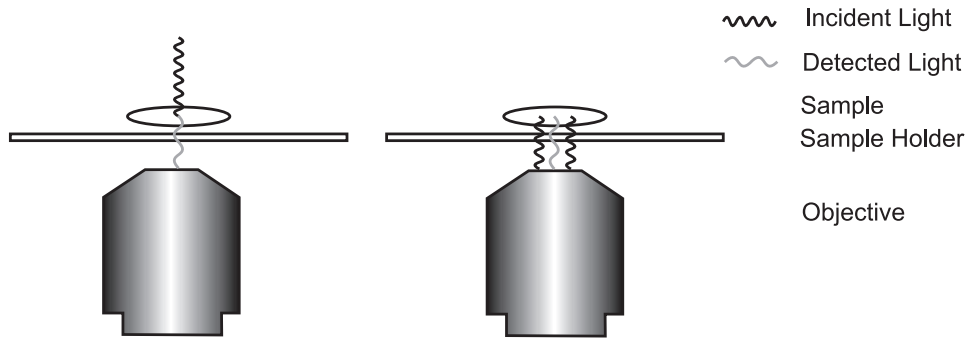


Figure 2.5: The two possibilities an object can alter the incident light and thus gives information about the sample. The transmissive beam is can be changed in phase and amplitude by the sample shown left. The fluorescence emits light which is detected backwards to the objective. This is also known as epi-fluorescence.

2.3.1 Brightfield Microscopy

In brightfield microscopy the sample is illuminated from an incident light beam which passes the sample. The light intensity is spatially modulated by the sample through absorption which can be seen by the observer helping to identify the sample on the obtained image. In common imaging the information of the structure is given by changes in the brightness as the detector is sensitive to amplitudes. However, additional information is contained in the phase of the light which passed the sample. That information can be transformed into an amplitude information as shown by Frits Zernike, honoured with the nobel price for his work on the phase contrast microscope. Another method building upon the is the *Difference Interference Contrast* (DIC).

Difference Interference Contrast

Difference Interference Contrast (DIC) is a technique used to enhance the contrast of a transparent sample. It works similar to phase contrast invented by nobel prize laureate Zernike which translates phase information of the sample into intensity information which is easier to detect and to visualise. Unlike Zernike's phase contrast microscopy, DIC uses interference phenomena to enhance the image contrast. The interfering beams are created through a specially build prism made from a birefringent crystal like quartz or calcite. In 1820, William Hyde Wollaston invented a prism that decomposes the ordinary (o-) and extraordinary (eo-) rays. These two beams take slightly different beampaths through the sample. As the beampath is slightly different, the phase information contained in both beams is different. Hence they can interfere with each other later in the beampath and accentuate the parts of the sample which influenced the beam the most. For correct alignment of the prisms, the Wollaston prism has to be put into the focal plane of both objective and condensor. Special objectives have to be used, which is

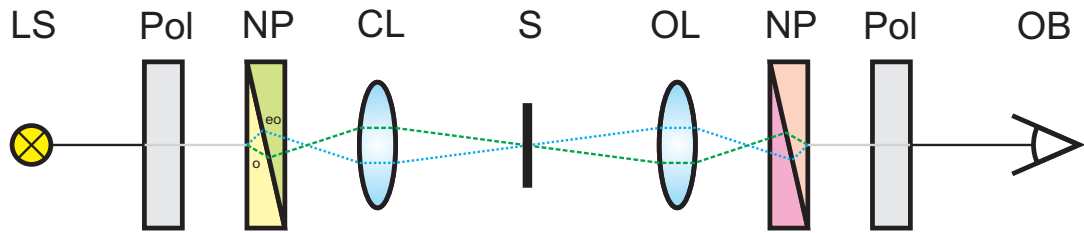


Figure 2.6: The schematic of DIC which shows the two rays ordinary (o) and extraordinary (eo) rays travelling through the sample and thereby generating two differently modified rays which later interfere to result in a plastic image. (LS: Light Source; Pol: Polariser; NP: Nomarski Prism; CL: Condensor Lens; S: Sample; OL: Objective Lens; OB: Observer)

costly and elaborate. An improvement is the Nomarski prism where the o- and eo-rays have their focal point outside of the prism. They are commonly used nowadays. The DIC arrangement is depicted in figure 2.6. The incident light from the light source (LS) passes a polariser (Pol) placed at an angle of 45° . A Nomarski prism (NP) separates o- and eo-rays and the condensor lens (CL) brings the light to the sample. The light passes the objective (OL) after which another Nomarski prism (NP) rejoins the two beams. The information of the image can then be detected after the light has passed another analyser (Pol) at 45° [40]. DIC is an alternative to phase contrast microscopy with the advantage, that it can be used for high NA objectives.

2.3.2 Widefield Illumination Microscopy

Historically, the sample was illuminated by natural light sources such as sunlight or a candle. The light was guided through a mirror to the sample. Although the sun was favoured as a very bright source of light, it changes its position due to the earth's rotation. Clouds could obstruct the direct sunlight but sufficient intensity was still present to illuminate the sample. The clouds diffuse the light, so that it lowered the effort to readjust the mirror to account for the rotation of the earth. When the clouds became for dense, the light was insufficient for measurements and it was also the case at night. A candle, on the other hand, is weather and season independent. Since the candle is not a strong light source its light has to be collected. In critical or *Nelson* illumination, named after its inventor Edward Nelson, the light was collected and imaged in the sample plane. The mirror was hereby carefully adjusted to collect the bright part of the flame. Because of the inhomogeneity of the source, the image of the flame on the sample was slightly defocussed to achieve a slightly smoothed illumination at the expense of lower intensity. With the introduction of electric light, a stronger light source with a more constant intensity was introduced to illuminate samples. Eventually, a field aperture was imaged to the sample instead of the flame to restrict the light to the field

of interest. Still, due to the shape of the filament, light bulbs are very inhomogeneous light sources. A diffusor was sometimes used to smooth the light distribution, but this method has the drawback of lowering the light intensity.

In the year of his dissertation, 1893, August Köhler published a method which overcame the problem of an inhomogeneous light source [31]. In his setup, an additional diaphragm was used, and is thereby also known as "double diaphragm illumination". His arrangement of the lenses follow the theoretical principles of his co-worker Ernst Abbe about image formation. The *Köhler* arrangement was set-up in such a way that the inhomogeneous source still resulted in a homogeneous illumination of the sample. Moreover, with this principle there is maximum light on the sample without additional stray or reflected light. This lowers the deposited energy to the sample, which otherwise heats up the sample. The way of the arrangement enhances the image at the focal plane and reduces the signal contribution of out-of-focus regions. Critical illumination has though the advantage that once aligned, the microscope does not need further adjustment in contrary to the Köhler method, where it has to be readjusted each time, the objective is switched. For modern microscopy with objectives of high NA's Köhler illumination becomes favoured to critical illumination due to a better image quality. The image appears elucidated and clear and has more contrast than with critical illumination.

Köhler Illumination

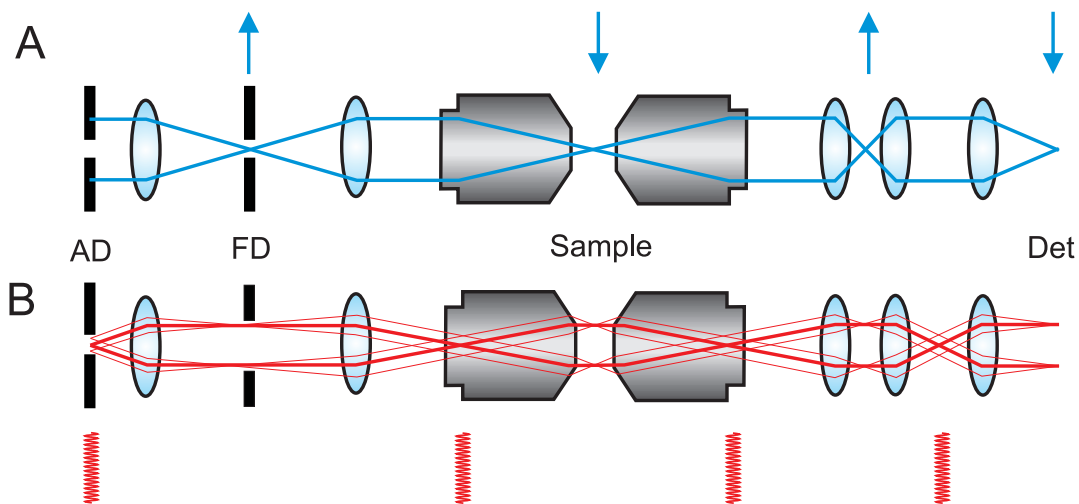


Figure 2.7: The Köhler principle can be described with two equivalent optical rays: The image forming ray with an arrow object appearing at different conjugated planes (A) and the illumination ray with the filament (B). The positions of the aperture diaphragm (AD), the field diaphragm (FD), the sample and the detector (Det) are labelled.

Köhler illumination is based on Abbes image forming theory and has two diaphragms or beam stops in use: the field diaphragm and the aperture diaphragm. In applying the principles of Köhler illumination, the effective image quality, that is higher contrast and an elucidated and clear image, is enhanced because unwanted stray light is minimised. In addition it is exceptionally beneficial for incandescent light sources which have rather inhomogeneous intensity distribution. Two interwoven beam paths can clarify the peculiar arrangement:

1. Image Forming Light Path
2. Illumination Light Path

The *Image Forming Light Path*, as seen in figure 2.7A, shows the image as an arrow forming in different planes of the microscope which are called *conjugated planes*. The first arrow is at the position of the field diaphragm. The following two lenses together constitute the condenser and images the field diaphragm to the sample. This adjusts the illuminated field according to the imaged field onto the camera and helps to reduce straylight from non-observed parts and results in less photobleaching of the sample. The arrow is again formed after the tubelens, a lens unique in design and focal length for the microscope makers. In principle, the image can already be extracted at this point by placing a field detector in this plane. Yet, an additional lens combination is often applied, to relay the image to the detector when an additional post-magnification is made. This also gives the possibility to implement filters as the filter's quality is enhanced in the collimated beam path. The camera is put to where the arrow forms again.

The *Illumination Light Path* is the description of the rays emanating from the light source. In figure 2.7B the formation of the filament images at several conjugated planes is shown. The size of the light source can be adjusted by the aperture diaphragm. The benefits of the aperture is often misunderstood. It is not for the regulation of the image brightness but to adjust the ray bundle angular at the sample plane. This is then responsible for the contrast of the image. As seen in the figure the aperture diaphragm controls the angle under which the light is falling onto the sample plane. If the aperture is infinitely small, only one ray due to diffraction is emanating from that part. As it comes from one source, this beam is then coherent. The aperture diaphragm is therefore a tool to regulate the coherence of the illumination.

To achieve both conditions for image-forming and illumination light path the lenses have to be arranged in that way that each lens has an overlapping focus with the next lens. Under these conditions it follows Abbe's theory where each focal element acts as a fourier transform of the object before. In other words the object in the focus before the lens is fourier transformed through the lens which results in the focus after the lens. As the aperture diaphragm is standing in focus of the conjugated plane of the fourier transform of the sample plane, it defines through its size the number of coherent light spots passing through the system. It has the same meaning of the angular size of the

cone of each light spot, that is the number of diffraction orders which hit the sample. The Köhler illumination is therefore an illumination method which is regulating the order to coherence. It was applied in the widefield part.

2.3.3 Confocal Microscopy

A second type epi-fluorescent illumination is confocal microscopy. The historically newer method is accredited to Marvin Minsky, who patented the technique in 1961. Confocal microscopy is the choice for more accurate measurements with less background interference. The principle used is to spatially exclude the signal from the sample volume that reaches the detector. In order to confine the excitation beam to minimise stray-light the laser is focussed into the sample and only illuminates the focus itself. A detection pinhole is placed in the conjugated plane of the sample which spatially filters the off-focus excitation light before the detected. Figure 2.8 shows how the confocal principle works. A collimated excitation beam falls on a dichroic mirror (DM) which reflects the beam to the objective lens (OL). The objective focusses the light to the sample which excites the fluorophores. The fluorescence emission from the sample is collected by the OL, passes the DM and falls to the first lens L_1 . This lens focusses the light onto the confocal pinhole (PH). Only light from the focus (solid line) passes the PH while off focus light (dashed line) is blocked by the PH. The light which passes the pinhole is then focussed by a second lens L_2 onto the detector (APD). To obtain an image with the point detector, the sample has to be scanned either with the laserbeam steering mirror or the stage holding the sample. This slows down the data collection to some few hertz acquisition rate per frame. This lack of speed is a drawback in confocal microscopy. To overcome this problem, several new approaches have been made. Regular scanners, usually galvanometrically driven mirrors, can go up to some kHz. Alternatively, piezo-mirrors can be used. Since images consist of two dimensions, even with kHz scanning

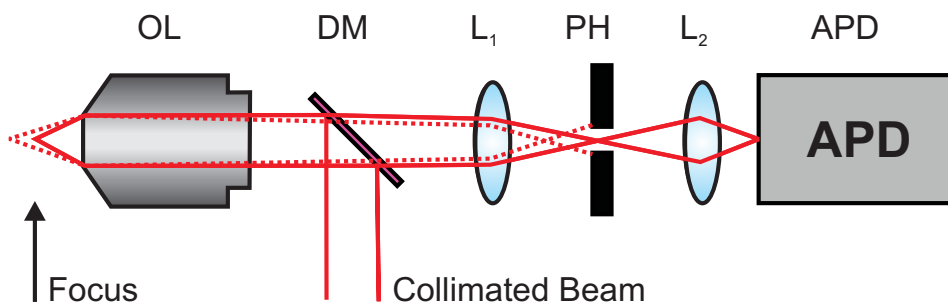


Figure 2.8: A schematic showing the principle of a confocal setup. Only light from the focus can pass the pinhole and become detected by the APD. (OL: Objective Lens, DM: Dichroic Mirror, L: Lens, PH: Pinhole and APD: Avalanche Photodiode.)

speed the total image acquisition speed goes only to some tenths of Hz at best. A recent development first published in 1995 by Tsien and Bacsikai is the *resonant scanner* [44]. A mirror mounted on a crystal is struck so that the whole mirror swings with a high resonant frequency of the crystal. This gives a high scanning speed in one direction. Together with the other mirror controlled by a galvo scanner, this method increases the total acquisition speed a hundredfold.

Another approach is the *Nipkow spinning disc*. The principle was invented by Nipkow and has a wide range of applications. Two fast rotating discs having multiple lenses and pinholes on it. An image is created by screening the many confocal spots over the sample. Unlike conventional confocal microscopy, the image is taken using a field detector. The acquisition speed is therefore limited by the readout speed of the detector. The spinning disc is more or less a hybrid between wide-field microscopy and confocal microscopy with the speed and the image quality greatly enhanced compared to conventional widefield microscopy. A more detailed description of the spinning disc confocal principle can be found in 10.2.1.

2.3.4 Additional Microscopy Techniques

In addition to the microscopy techniques presented above, there are numerous examples of microscopy techniques which can be classified into imaging and non-imaging techniques. Depending on the application, the methods can significantly vary to suit different questions arising. Methods which will be described later in the manuscript in detail are *Total Internal Reflection Microscope* (TIRF), which greatly enhances the signal to noise (S/N) ratio and *Fluorescence Correlation Spectroscopy* (FCS), a sensitive measurement to extract dynamics of solutions.

2.4 Cell Biology and Biochemistry

To understand the fundamental principles behind the processes involved in living organisms, it is essential to investigate the smallest component, that comprises the organism. The word "cell" was coined by Robert Hooke in 1665 when he observed the structure of cork cells under the microscope and comparing them to the rooms for monks in a monastery. However, it was first in 1839 that Matthias Jakob Schleiden and Theodor Schwann stated that the bricks which made the structure of every organism is in fact the cell. In their cell theory the cell carries all the information necessary for proper functioning and heredity transmission to the next generation.

With this knowledge, it is possible to study the structure and process of the cell and furthermore relate them to the larger organism they form. The cell studied in this work is of eucaryotic type. In contrary to the procaryote, cell they have well organised com-

partments with specific tasks. The most prominent one is the cell nucleus, which also coins the term "eucaryotic".

A common eucaryotic cell model used in biology is yeast. Yeast has been known since the ancient world and has a widespread of applications beyond fermentation. In genetics, the species *Saccharomyces cerevisiae* is a well known cell model with many similarities to mammalian and human cells. Many processes and biomolecules involved can be studied in a slightly simpler environment and later related to their human homologues. The advantages of studying yeast instead of other mammalian cells is the much faster metabolism. That makes genetic alterations come into effect much faster.

Among eucaryotic cells are also mammalian cell lines, moreover human cell lines. The typical immortalised cell lines are cancer cell lines. Common healthy cells are apoptotic after the so-called Hayflick limit, which defines the approximate number of cell divisions before apoptosis [20]. Mutants such as HeLa, derived from a tumour of a patient in 1951, overcame the Hayflick limit and are in principle immortal. This is beneficial to the cell biologists because scientists have a stable cell line in different laboratories which give comparable results and are easy to cultivate. Most of the functions are still fully operational and moreover have been extended to suit the demands of the biologists.

Dynamical processes are an attribute of living organisms. Throughout the cell cycle, from one cell division to the next, particles are built, interact and are transported. In addition, the whole cell itself is interacting with its environment. To understand the fundamental processes involved in the very complex nature of the cell, it is desired to establish methods to elucidate selected processes. This can be done through a biochemical approach where, due to the knowledge of the mechanism of selected biochemical assays, the application reveals processes of the cell by deriving the information from the measurement and checking it for erratic influences. Another approach is to visualise the processes. The system is usually altered to highlight the process out from the many competing others.

The work of a cell biologist and biochemist is therefore to alter the cell system via genetic and biochemical methods. The genetic method uses gene vectors, which then introduce a mutation to the cell. A very popular method in the introduction of fluorescent proteins into the gene is cloning. But not only is the cell made to do something it was not able to do prior to infection, but known information of the cell can also be deleted or silenced. To analyse the structure of the cell, biochemistry is often necessary to chemically extract parts of the cell. In gel blots, proteins and other biomolecules can be analysed.

2.5 Data Acquisition

A careful evaluation is necessary for a correct interpretation of the obtained data. Usually, the data contains noise or other inherited errors which can lead to incorrect conclusions.

The acquisition has to be done with the proper resolution, that is an ideal sampling rate. According to Nyquist, the acquisition needs to take place at twice the frequency of the highest frequency compound of the signal in order to obtain the complete information. If the sampling rate is less, information is lost. On the other hand, a higher sampling rate will not lead to a gain of information but will rather lead to a higher amount of data where the handling might become difficult.

An important aspect of the experiments conducted in this work is the correct timing of all participating elements. It turns out that the timing is especially sensitive in these types of experiments where up to 50.000 datapoints are measured so that any slight deviation will sum up to a significant temporal shift, obstructing a correct analysis. Depending on the timescale, the limit can be the data transfer time coming from the length of the cables up to the harddisk access time for writing large amounts of data. A special consideration turns out to be the choice of the operating system. Depending on the system used, real-time measurements may be impossible to conduct.

2.6 Introduction to the following Chapters

The experiments that are presented and discussed will be subdivided into three main parts:

The first part is about the newly developed tracking microscope which enables the tracking of fluorescent particles during the measurement. It combines laser scanning confocal microscopy with the ability to follow single fluorescent particles. The tracking was characterised for fast tracking experiments. The setup was extended to also observe the surroundings of the fluorophore which is beneficial for relating the particle to the structure and to see interactions within. It can further be applied as a refocussing technique which is interesting for long measurements where focus drift is an issue. The major innovative step is the online tracking capability.

For particular experiments with high particle density, orbital tracking cannot be used. For experiments on yeast cells, z-stacking is also an option. Using image stacking with a spinning-disc confocal microscope (SDM), we investigated the mechanism of mRNA localisation. The spinning-disc enables rapid acquisition of images recording the dynamics of mRNA transport. Further image processing then revealed the transport properties of different mRNA species.

Image stacking with the SDM was also applied to investigate protein dynamics in the third part of the thesis. The experiment elucidated the dynamics of *Polokinese1-interacting checkpoint ATPase* (PICH) protein in mitotic HeLa cells from Metaphase to Anaphase and their role in proper segregation.

Part I

The 3D Orbital Tracking Microscope

CHAPTER 3

Introduction to part I: Tracking Microscopy

Traditionally, tracking is conducted using post-processing techniques. Since image analysis is still too ineffective to follow particles of interest in real-time, the most popular way to track fluorescent particles is done by conventional imaging. The images can be analysed later to obtain the position of the particles resulting in a trajectory. Imaging methods lack a feedback mechanism and cannot track particles, that move out of the observed volume. Especially in the axial direction, particles frequently move in and out of the focus. This obstacle can be overcome by image stacking which provides the information of a three dimensional (3D) volume. Here, the data can also be analysed later in 3D. Moreover, the problem of the particle moving out of the observed volume is not completely solved. Also it is a time consuming procedure since the whole volume has to be observed.

In this part we will present a technique which specifically selects the most interesting part of the volume with the particle of interest. This newly developed microscope provides an alternative to postprocessing tracking. Based on a confocal laser scanning microscope, it traps the particle with a custom scanning scheme and follows it during its journey through the space. At the same time, the focus of the system stays with the tracked particle. This re-adjustment of the focus then enables the possibility to attach an additional channel to simultaneously observe the particle surroundings. For this purpose, a widefield system was attached to the microscope. The widefield setup comprised an optional two-colour alternating laser excitation source to observe the surrounding structure of the tracked particle with clear spectral separation and a Köhler arrangement of the lenses to enable high contrast image acquisition. The tracking and the widefield observation system was tested and applied to experiments where three-dimensional position accuracy is required for following particle dynamics or focus re-adjustment was beneficial for sample observation.

CHAPTER 4

Basics: Tracking

4.1 Tracking

It is of great interest to track single molecules inside a cell to understand the driving forces of life. The prominent and typical way to conduct tracking experiments is to post-process acquired images. Hereby, accurate measurements can simply be done as the time spent on the analysis is unlimited. The only requirement on this type of tracking is that the particle moves inside the predefined volume, because otherwise the particle is lost. The more demanding way to track is done using an on-line measurement. The difficulties are to establish methods sophisticated enough that the tracking procedure can decide quickly what to do in order to follow the particle with as few parameters as possible. Such a feedback based tracking method with a moving particle will be described in the following pages.

To determine the position of a particle in a volume, four distance measurements from known anchor points have to be made. From the measured distances it is a straightforward calculation to find the particles position. The accurate position can be obstructed by the movement of the particle which must not be faster than the acquisition time until the position is measured. Most commonly, the acquisition is done by taking several image slices of different focal positions and afterwards put them together. However, the procedure becomes more difficult when it comes to fast dynamics of faint signals. Usual image processing is not fast enough for dynamics inside a cell as decision making algorithms have enormous demands on the system even on static problems. A first tracking approach was published by Howard Berg in 1971 where *Escherichia coli* (E.coli), a bacteria, was kept in focus despite their high motility of up to 50 times their size per second [4]. He used six fibres, each of them looking at the vicinity of the centre of the focus in each direction connected to *Photo Multiplier Tubes* (PMT). The signal of that PMT rises as soon as the bacteria moved closer to the observation volume. The feedback signal keeps a steady state in which the bacteria is kept in focus. The progress of *Laser Scanning Microscopes* (LSMs) enabled scientists to use laser foci instead of fibres. The

advantage is the more specific excitation and observation restricted to a much smaller volume. In 2000 Jörg Enderlein proposed a modified version of how to obtain a particle position in the xy plane via orbital scanning [15]. The suggested method is to circularly move the laser focus around a particle and to calculate the particle position by looking at the intensity modulation. It was experimentally applied by Valeria Levi, Qiaoqiao Ruan, Katarina Kis-Petikova and Enrico Gratton in 2003 on a two-photon microscope combined with a procedure allowing tracking along the optical axis in z [35]. For tracking in z, they moved the objective up and down monitoring positions above and below the particle. The method presented here is based on this tracking procedure with a variation in the z-tracking which allowed to install an additional observation channel based on widefield microscopy.

4.2 Particle Movement: Diffusion and Transport Mechanisms

To evaluate the movement of a particle, it is necessary to distinguish between random and real steps. Some motion modes like active transport can be easily related to specific types, however, a comprehensible analysis is still needed to determine the type of motion for all cases. In recent years diffusion analysis was done using the method of *Mean Square Displacement* (msd). In this analysis, the average distance versus step size or time is plotted. It starts with the average distance travelled for each single step, then after every second step and so forth. This results in a curve in which it is possible to exhibit a typical behaviour according to four different types of motion with the corresponding equation for the msd-plot for particles travelling in two dimensions [48]:

1. Diffusion $\langle r^2 \rangle = 4Dt$
2. Anomalous Diffusion $\langle r^2 \rangle = 4Dt^\alpha$
3. Active Transport or Drift $\langle r^2 \rangle = 4Dt + (vt)^2$ and
4. Corralled Motion $\langle r^2 \rangle \simeq \langle r_c^2 \rangle [1 - A_1 \exp(-4A_2Dt/\langle r_c^2 \rangle)]$

The data obtained must however be treated carefully. As a matter of fact the way the particle moves can vary with time. The danger of an msd-analysis is to average out the motion behaviour during the effort of gaining enough datapoints for a reliable analysis.

Diffusion

Molecules are in thermal motion. In a typical environment, the molecules can not move freely, but are restricted by the existence of other particles which eventually hit and change their direction of motion. The distance a particle can travel on average before hitting a neighbouring particle is defined by the *Mean Free Path*. It depends on the energy of the molecules, the number of molecules inside the volume and the probability

of the molecule to hit another one. However, this area grows in time. Figure 4.1 left shows the linear relationship between the msd and time of the msd-plot, indicating diffusive behaviour of a particle. Purely diffusive behaviour underlies the laws of random motion, which was experimentally shown by Robert Brown, for whom it's also called Brownian motion. The theory was derived independently by Albert Einstein 1905 and Marian Smoluchowski in 1906.

Anomalous Diffusion

From time to time, the diffusing particle can hit an obstacle. It may interact with the obstacle for a short while until continuing random diffusion. The curve in the msd-plot resembles that from the diffusion. Because the particle becomes trapped at some obstacles, the slope decreases.

Transport

A typical transport process moves the particle further away than simple diffusion. The curve in the msd-plot shown in figure 4.1 is therefore not linear but follows a positive bent towards higher distances. If the particle undergoes directional movement, it is a strong indication that some force is applied to the particle. The particle is being transported, with the exception of experimental drift, due to microscope movement. To discriminate between transport and drift, one introduces passive and active transport.

Passive Transport is caused by e.g. a density gradient and is observable for instance during osmosis for the water molecules. Particles starting in a dense environment try on average to move to a volume with lower particle concentration. A second source of

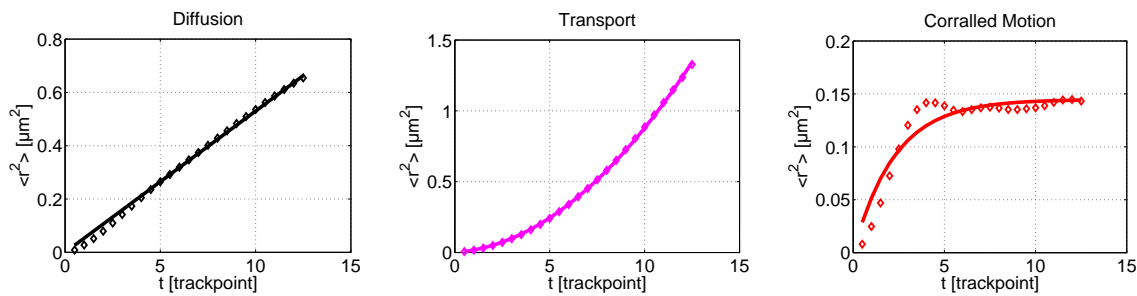


Figure 4.1: Three sets of graphs show the *mean square displacement* (msd) plots for different types of motion in two dimensions. (Left) Anomalous diffusion where on average the covered area of the particle trajectory grows linearly with time, (middle) active transport where a favoured direction of the particle movement bends the line to a curve and (right) corralled diffusion, where an obstacle hinders the particle to move freely in space.

passive transport is a movement of the layer underneath like a drift or a flow, e.g. the stage, the microscope or even the sample itself. As the source of the movement is not always visible, additional analysis of the data has to be made. Usually the coordinated movement of neighbouring particles gives the necessary information to evaluate passive transport.

In contrast to passive transport, **Active Transport** is a particle movement which is caused due to a force actively dragging at the particle. In biological samples, these are usually *Adenosinriphosphat* (ATP) driven processes. ATP is the biological energy source for the so-called motor proteins. These molecules are involved in all types of cellular movement. The prominent motor proteins are carrier vehicles inside the cell. They move along well-defined paths inside the cell and transport a load. Typical motor proteins are kinesin, dynein and myosin. The first two proteins mentioned move along the microtubular network while the latter moves along the actin network. The whole cellular skeleton, to which also the intermediate filaments belong, helps to maintain the structural integrity of the cell.

Corralled Motion

In the case that a particle is restricted to a certain volume, the diffusion analysis of the motion in an msd-plot shows an asymptotic behaviour. In other words, even with long observation time the particle cannot go beyond the area to which it is confined. One therefore speaks of a corralled motion. The size of the corral out of which the particle cannot escape can be derived by the asymptote of the msd-analysis. A typical corralled motion trajectory is shown on the right hand side in figure 4.1.

CHAPTER 5

Methods:

Two Confocal Pinhole Tracking with Simultaneous Widefield Imaging

For this work, a lot of different parts were combined into one specialised instrument. The description of the tracking procedure as well as the description of the microscope with the periphery devices, such as the control and the programs developed for this system, will be presented in this chapter.

5.1 Confocal Scanning

The scanning component is the core part of the online tracking procedure. It is an interplay of the mirrors which move the laser in x and y and the piezo-positioner to move the objective along the axial z-direction. As the focussed beam only excites a very restricted volume in the sample, the particle first has to be close to the laserfocus in order to start the tracking procedure. Thereafter, at least four areas around the particle have to be measured to derive the three-dimensional particle position. In this work, a set of at least 256 datapoints were obtained during an orbit.

5.1.1 XY-Tracking

The scanning principle is based on the effect that the fluorescence intensity of a chromophore is dependent on the power of the excitation and thus dependents on the distance from the laser focus. Using a confocal setup where the laser is focussed into the layer observed, the collected intensity value gives information about the distance of the chromophore away from the centre of the laser focus. For tracking, the laser focus is orbited around the particle. In the ideal case, the particle is situated in the centre of the orbit and thus the intensity throughout an orbit stays constant. However, if the particle is displaced from the centre the fluorescence signal will vary during one scanning orbit.

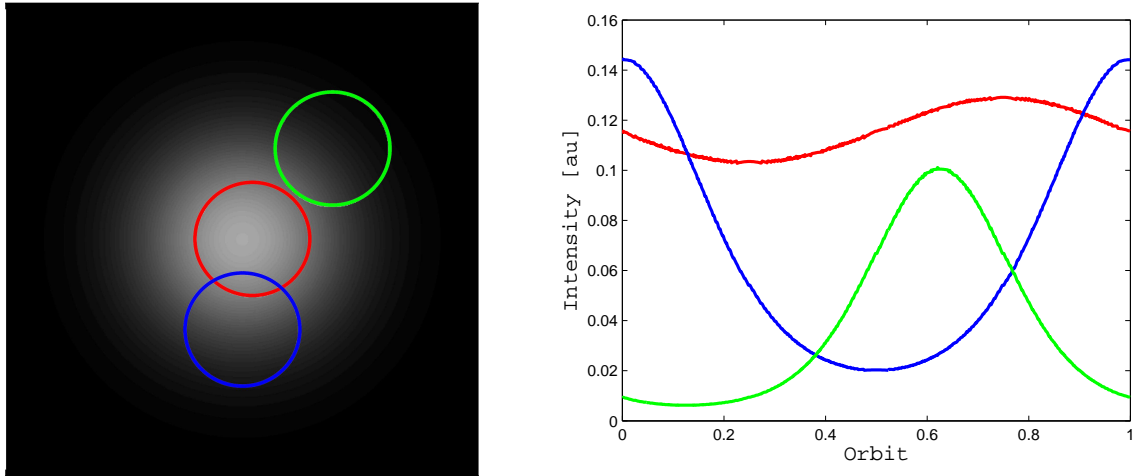


Figure 5.1: The left picture shows a particle in white with coloured scanning trajectories and the corresponding intensity trace are shown on the right.

A feedback loop coupled to the scanning mirrors corrects for the shift of the particle position and the laser is re-centred to the particle for the next scanning cycle. This method is advantageous to other scanning methods, like the ones from Howard Berg [4] or Göbel [18], since circular movements are easily established and also give a comparably easy data analysis treatment. An example of three different orbits of the laser around a fluorophore is shown in figure 5.1. The left picture shows a particle in white with the orbits in red, blue and green. The beam is scanned along these tracks starting from 0 at the top clockwise to 2π . The image on the right shows the corresponding intensity values for the three trajectories for one complete orbit. It clearly shows the dependency of the angular position of the particle and its distance from the orbital centre. To calculate the particle position, the average intensity and the phase must be derived from the trace. A fast analysis which gives good results is achieved with a *Fast Fourier Transformation* (FFT). The Discrete Fourier Transformation is the approximation of a periodic signal to a set of trigonometric functions with different amplitudes and frequencies. In an FFT, the algorithm was improved to rapidly obtain a result. The FFT of a function $I(t)$ is then

$$FFT(I(t)) = I(t) = 0.5 \cdot A_0 + \sum_n A_n \sin(n\omega t) + B_n \cos(n\omega t) \quad (5.1)$$

$$\begin{aligned} DC &= 0.5A_0 \\ AC &= \sqrt{A_1^2 + B_1^2} \end{aligned}$$

From the DC and AC term components, the distance of the molecule from the centre of the orbit and the angle can be derived. AC divided by DC gives the value for the

radial distance and $\tan^{-1}(A_1/B_1)$ gives the angle at which the particle is located. The scanning is most sensitive at the highest slope of the intensity value, which is at the *Full Width at Half Maximum* (FWHM) of the approximated gaussian PSF [32] [34].

5.1.2 Z-Tracking

The tracking procedure in z utilises the concept of the confocal pinhole, which is usually used to measure in the exact focal plane of the sample. For tracking, the fluorescence signal is split into two separate adjustable confocal beampaths, each one of them equipped with a confocal pinhole independently adjustable along the optical axis. According to simple geometrical considerations, shifting of the pinhole allows us to address a different sample plane. By choosing one of the pinholes to detect a plane above the focus and the other one below the focus, the detection becomes sensitive to deviations of the sample in z. This is illustrated in figure 5.2. In our system, the fluorescence signal is collected with a single objective and is then split into the two beampaths after the dichroic mirror which separates excitation from emission. The z position can be determined by the comparison of the detected signal intensity of each of the beampaths:

$$z_{modulation} = 2 \cdot \frac{I_1 - I_2}{I_1 + I_2} \quad (5.2)$$

I_1 Intensity of the first pinhole

I_2 Intensity of the second pinhole

Previously, a two-photon method with an objective moved up and down was established by Levi et al in order to do tracking in z [35]. The major difference of our system is that the objective is not moved in order to obtain the axial position of the particle. This is beneficial since the setup does not have heavily moving parts that can induce oscillations and hence affect the accuracy of the setup. In addition, as the objective is not oscillating it can be used to obtain sharp images in the vicinity of the particle. For this reason, a widefield setup is installed to simultaneously observe the surroundings of the particle.

5.2 Simultaneous Widefield Observation

The widefield setup can be used simultaneously to the tracking method. Using different regions of the visible spectra, two additional colours can be observed at the same time with the tracking. The excitation can also be done using *millisecond Alternating Laser Excitation* (msALEX) [30]. In this technique, different fluorophores are not excited simultaneously but subsequently. With alternating excitation and separated detection, the discrimination of the fluorescence origin can be accurately achieved. Especially in

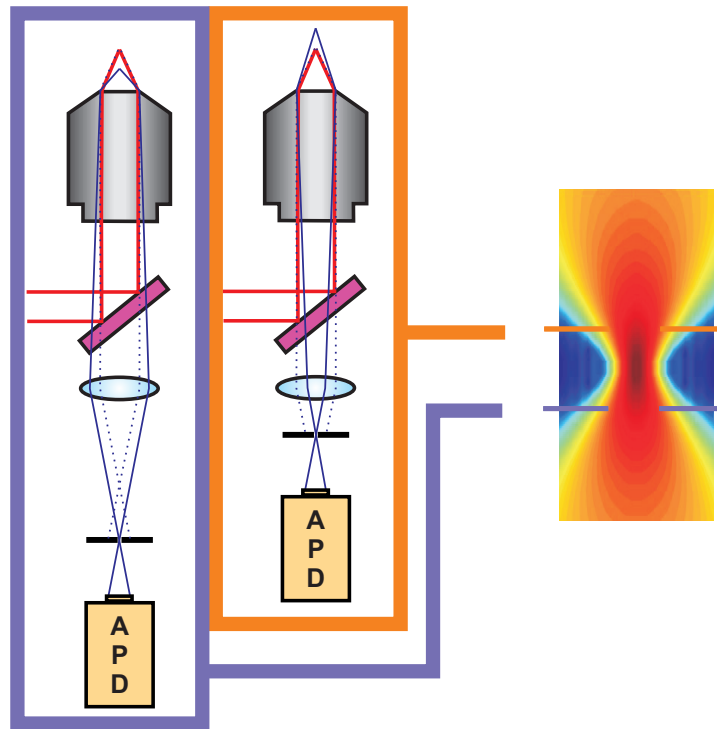


Figure 5.2: The setting of the confocal pinholes for z-scanning. The blue pinhole is shifted away from the sample and detects therefore a layer below the focal spot, respectively the orange pinhole above.

the case of spectral crosstalk and overlapping excitation spectra, it is very important to rule out influences resulting in wrong data interpretation.

The arrangement of the widefield configuration follows the criteria for Köhler illumination to obtain an evenly illuminated beam. The observed area is then transferred to a filter cube which splits the two emission spectra and images them on two separate areas of a single EMCCD chip. The simultaneous acquisition is helpful for the synchronisation of the data. In the end, the tracking occurs at the same time as the surroundings are observed using the widefield setup. Since the widefield setup is an individual part of the microscope, the adjustment to match the confocal part has to be done carefully.

5.3 Optical Design

The design of the setup is based on the optical resolution limits of the structure being observed and can be estimated using Abbe's resolution limit:

$$d = \frac{\lambda}{2n \cdot \sin(\theta)} \quad (5.3)$$

- d [m] : Smallest Resolvable Distance
 λ [m] : Wavelength
 n [] : Refractive Index
 θ [rad] : Half Opening Angle of Light Cone

The maximum possible resolution can be achieved with the laser of the lowest wavelength. It will serve as a calculatory basis for the rest of our system. The lowest wavelength in our system is given by the 488nm diode laser. Starting from that point, the different optical parts of the setup can be subsequently calculated. According to Abbe's law (equation 5.3), the smallest structure that can be resolved depends on the wavelength and the numerical aperture and is calculated by their ratio. With the numerical aperture of the WI objective of NA=1.2, the smallest resolvable distance is 203nm. This structure is imaged on the EMCCD. According to the Nyquist-Shannon theorem, the ideal spatial sampling frequency to cover the 203nm on the chip would be to cover this distance by three light sensitive sensors, i.e. pixels. If two signals are just above the smallest resolvable distance, the resulting signal would appear as in figure 2.4. Each maximum of the signal and the minimum in between has to be detected by independent pixels. Hence each pixel covers one third of 203nm which corresponds to 68nm. If a pixel is smaller, the system is oversampled and if the pixel size is larger undersampled. The size of the chip is 512x512 pixels. Therefore, our field of view on the sample is 68nm times 512 pixels or 34.8 μ m.

Furthermore the correct size of the optical fibre can be calculated from the knowledge of the brightness theorem stating that the area of the diameter of the field times the NA is a constant.

$$A \cdot NA = const. \quad (5.4)$$

- A [m^2] : Area
 NA [] : Numerical Aperture

The fibre core diameter is focused to the area with a diameter of 49.2 μ m times the NA of the objective, NA=1.2. Then, divided by the NA of the fibre, NA=0.22, this yields 269nm for the fibre core diameter.

Furthermore, the magnification factor of the system that yields maximum magnification while maintaining the resolution can be calculated. Since the CCD itself has a pixel size of 16 μ m², the magnification has to be about 235x. With a magnification of the objective given with 60x, the post magnification of the setup has to be approximately 3.9x. The size of the field aperture both in excitation and emission can be derived by geometrical

considerations. From the lenses involved in the excitation beampath, an achromatic doublet with a focal length of 400mm respectively 3.3mm for the objective lens, and emission beampath, 200mm for the tubelens of Nikon and 3.3mm for the objective lens. A special aperture has been constructed to cover the range from 1.26mm, the size of the emission field, and 2.52mm, the size for the excitation field, up to about 10mm. Since the other lasers are of higher wavelength, i.e. 532nm, the same system leads to oversampling for lasers of higher wavelength. The CCD camera was mounted such that the rectangular *region of interest* (ROI) can be read out quickly. It has to be noted that the diameter of the lenses has to be larger or equal to the beam diameter in order to avoid additional apertures influencing the beam quality. Also here, the concept of Köhler illumination becomes useful to understand and to calculate the correct minimum lens diameters.

The design of the confocal beampath results from the arrangement of the wide-field setup together with the dimensions of the microscope itself. For the confocal illumination, the collimated laserbeam enters the objective centred in the back aperture and perpendicular to the aperture plane. However, during scanning, the beam has to be moved to reach other parts of the sample field. To ensure a homogeneous illumination under the assumption of an ideally corrected objective, the beam must not move from the centre of the objective's back aperture but only its direction should be changed. As the distance from the scanning mirror to the back aperture cannot be infinitely short, the mirror would move the beam out of the centre. To address this deviation, the mirror is imaged to the back focal plane of the objective by two lenses. In doing so, the spot at the back focal plane stays constant while its incident angle changes with the mirror movement. The approximate tilt angle of the mirrors can be estimated from the size of the scanned field that is $21.3 \mu\text{m}$ divided by two since it is a symmetric deviation in both directions. The tilting angle α then equals $\arctan(0.0212\text{mm}/2.619\text{mm})/2 = 0.23^\circ = 4\text{mrad}$. The actual angles were determined by the tracking software with 1.70V for x (peak to peak), that equals 4.25mrad and 1.26V for y (peak to peak), which equals 3.15mrad. The centre of the tracking program covers a quadratic field of 256x256 pixels. Also, the tip-tilt movement of the piezomirror can introduce a transformation of the rectangular scanning field.

The setup can be subdivided into two parts:

1. Laserscanning Confocal Beampath for the tracking
2. Widefield Beampath for additional observation

These parts will be presented now in detail.

5.4 Technical description

The microscope is based on an inverted Zeiss Axiovert 200 stage. A Märzhäuser stage is used to move the sample in x and y. The complete setup hosts the widefield and the confocal system which can be used simultaneously. The widefield system is attached to the sideport of the microscope while the confocal illumination beam path utilizes the backport. The three excitation lasers are inside a box to reduce straylight and two optical fibres guide the beam to the correspondent part of the setup. As detector, an EMCCD camera is used for the widefield detection and two APDs for confocal detection. For a more in depth discussion, the following section is subdivided to two parts dealing with the confocal and the widefield beam paths.

5.4.1 Confocal Beampath

For confocal illumination, a 633nm HeNe laser from Melles Griot with a power of 5mW is guided through a mechanical shutter and a density filter wheel into an optical fibre. The fibre is a single mode fibre which propagates a single mode and a gaussian shaped beam exits the fibre. The light is then collimated with a beam diameter of 6mm, to

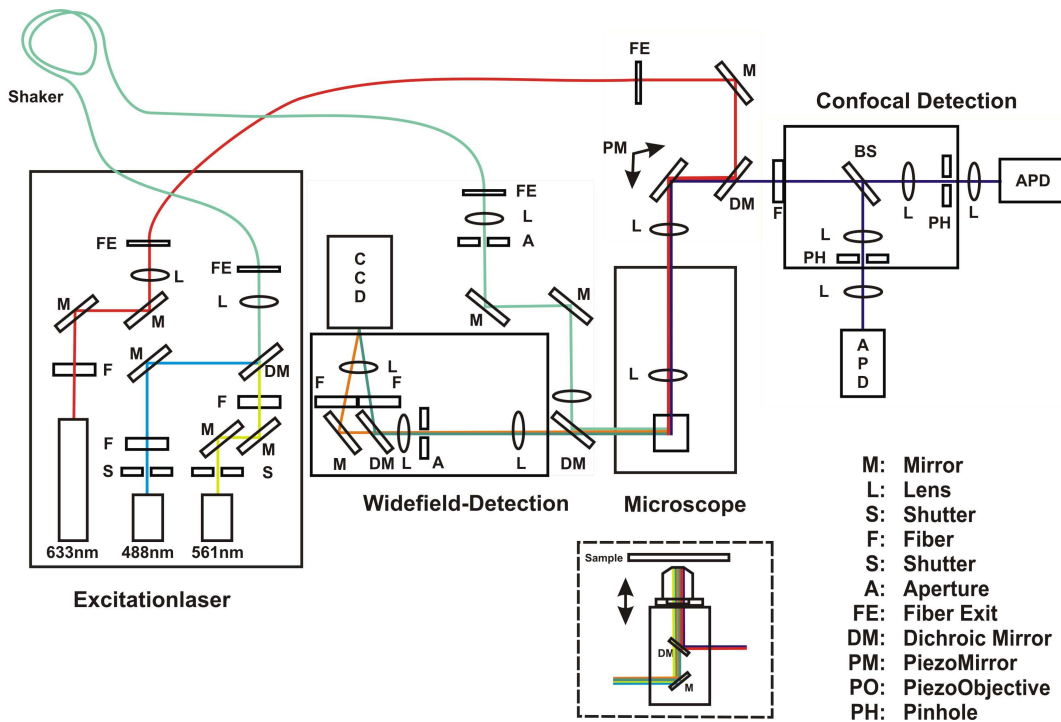


Figure 5.3: The setup of the tracking microscope showing the excitation sources, the microscope base and the two arrangements for widefield and confocal detection.

match the diameter of the back aperture of the objective. The beam is reflected by a mirror and a subsequent dichroic mirror (z532/635) to separate excitation from emission. Afterwards, the beam hits a piezo-driven 2D tip-tilt mirror from PI. This mirror plays a central part in the tracking and is the scanning unit in this setup. It guides the laser to different x and y positions on the sample. In order not to cut the beam by the back aperture of the objective, the mirror-plane is imaged by two lenses, with a focal length of 150mm each, to the back aperture of the objective. Hence, the incident angle of the beam at the back aperture is varied but the beam position stays unchanged. Inside the microscope, a microscope filter cube hosts a dichroic mirror (q630SPXR) which unites the red excitation beam from the confocal setup with the blue and yellow excitation from the widefield system. The objective is a Nikon Plan Apo 60x/1.2 WI, which is apochromatic and corrected for spherical aberrations. The confocal laser beam enters the objective at different angles according to the tilt-angle of the scanning mirror altering the position of the sample that is illuminated. Additionally, a piezo-driven objective nanopositioner is used to move the focus in different planes in the sample.

The fluorescence beam is guided through the same path as the excitation beam entered the microscope. At the scanning mirror the fluorescence signal becomes descanned, which is the unravelling of the angular information of the fluorescent signal. This descanning is possible, because the fluorescence lifetime is orders of magnitudes shorter than the speed of the mechanical movement of the mirror. Hence, the signal appears at the same spot as the excitation beam and can therefore become descanned. After the scanning mirror the dichroic mirror separates the excitation wavelength from the fluorescence. The beam enters a light shielded box where the beam passes a cleanup notch filter (hq695/100) for eliminating scattered laser light following a 50:50 beamsplitter. This beamsplitter enables the simultaneous measurement of two focal planes in the sample. Each beam from the beamsplitter is travelling to a separate confocal detection setup consisting of a lens with a focal length of 60mm and a fibre with a core diameter of 50 μm and an APD.

5.4.2 Widefield Beampath

The illumination for the widefield system utilises two continuous wave (cw) lasers of different wavelengths. The Cobolt Jive diode laser supplies the system with 561nm laser with approximately 25mW laser power. The laser beams are joined with a dichroic mirror (z488rdc) to light emitted by a Coherent Sapphire diode laser at 488nm with 25mW. The laser beam is switched on and off via a mechanical shutter manufactured by Uniblitz and a density filter wheel is used to continuously adjust the laser power for the corresponding wavelength. The combined laser beams are focussed by an achromatic doublet lens with 50mm focal length into a multimode optical fibre with a core diameter of 365 μm . The fibre is loosely attached to a shaker forming two loops of 90° to each other. The shaker is switched on during measurement to minimise interference effects.

Interference appears because of the comparably large size of the diameter of the fibre core in which different laser modes can interfere with each other and produce the so-called laser speckles. By vibrating the fibre, the interference pattern are randomly distributed in time and therefore the intensity variation flattens during collection of an image. After exiting the fibre, the laser beam is collimated via an achromatic doublet with 50mm focal length and passed through a custom designed aperture used as the field aperture. The beam is guided by two mirrors an achromatic doublet with a focal length of 400mm and reflected towards the microscope by the dichroic mirror (z488/561). The focussed beam has its focus at the back focal plane of the objective, already mentioned in the confocal description. The fluorescence is collected by the same objective. As is the case for our inverted microscope, the epi-fluorescence technique collects fluorescence from the same direction as the excitation came from. This has the advantage that the main laser power is not collected by the detection path but only some backscattered light and light from the mobile fluorescent particles exhibiting a spatially homogeneous emission pattern. The numerical aperture defines the amount of light that is collected. The light is collimated by the objective and separated from the excitation laser beam by the dichroic mirror (z488/561) mentioned above. A lens, the tubelens of 200mm focal length, produces an image at its focus. At this position, an aperture restricts the light to the field of interest in order to minimise obstructing scattered light. To optimise the resolution, the image is magnified thereafter via a two-lens system. Because two excitation sources are used, two different fluorophores can be imaged. The two emission spectra of the detected beam become separated between the two achromatic doublets of the magnifying lens system where the beam is collimated. First a dichroic mirror splits one spectrum towards the detector, while the other colour is transmitted and reflected to the camera by a mirror. The two beams are passed through a cleanup filter to suppress any remaining laser light before passing the second lens, which produces two images according to the spectra on the EMCCD iXon 16+ from Andor.

5.5 Design of the Computerised Control

To ensure a flawless operation of the system, the setup was controlled by two computers. As described in the theory in section 2.5, the timing of tracking in combination with the image acquisition in widefield is essential for the temporal synchronisation of both parts. It was observed during the construction of the system that the software which controls the image acquisition is very sensitive to the process priorities of the operating system. An interrupt request such as a movement of the computer mouse or an internet firewall request could disrupt the continuous acquisition of the data. As the tracking and acquisition software had a high demand on the computer resources, the two systems were installed on independent computers.

The first computer was running on a Windows XP professional operating system. Two

PCI cards from ISS were installed. The 3-axis card (Version 1.0) controlled the scanning mirror and the objective nanopositioner for the z dimension. The cables for the piezo-mirror passed an additional homebuild potentiometer with a low-pass filter to filter high-frequency and for calibrating to two axes. The output of this potentiometer was connected with the controller (E.333) of the piezo-mirror from PI controlling the piezo-mirrors (E.300) from PI. The cable for the objective nanopositioner was connected directly to the controller (MIPOS 100PL, piezosystem Jena) which controlled the nanopositioner CAP100 μ . The 3-axis card was synchronised with a cable to the second card in the computer, the FCS card (version 1.0). This card collected the single photons detected from the APDs. The cables were connected to a homebuild power supply for the APDs, with a fuse included to protect from too high intensities or temperatures. The tracking software (SimFCS) was written by Enrico Gratton. This program controlled both ISS cards for fluorescence detection and for controlling the dynamic parts of the scanning. Despite tracking it was able to obtain confocal images and FCS respectively FCCS curves.

The second computer, also running Windows XP professional, controlled the EMCCD for the widefield imaging. This camera (iXon16+) from Andor Technologies was directly connected to the pc-card installed in the computer and was controlled by the IQ 1.7 software. A shutter control system captured the TTL signals of the camera and distributed the signal to the shutters of each channel. This device was build by the electronic workshop and could be used for msALEX experiments.

The second computer was also equipped with two National Instruments (NI) cards (PCI-6036E and PCI-6733) which could be used for digital voltage input and output. These cards could control for instance the piezo stage installed on the microscope either with an included interface or with custom made programs. A camera observation system was included with a simple CCD, alternatively a common photcamera was attached to safely observe the sample.

5.6 Selected Custom Programs

Programs specifically written for this work where either used for simulations to consider theoretical aspects, for the control of the setup and for the analysis of the obtained data. For theoretical considerations a program for the three dimensional intensity distribution of the focal volume was programmed in *Matlab*. With parameters from focal length, diameter of the beam and the back aperture of the objective, it was possible to get an idea of the theoretical intensity distribution at the focal plane in three dimensions. It is based on a the publication of Horvath [24]. To evaluate the intensity according to size and position of the pinholes, a ray-tracing program was created which is, in general, a paraxial approximation. Here it is used to visualise possible deviations due to pinhole

positioning.

In contrary to the simulations, some *Labview* programs were created to steer the voltage control cards from national instruments. This was helpful during the calibration and characterisation of the tracking system.

Matlab was used to evaluate the data obtained for the tracking. A large program was created to first read the set of data. This was the trajectory file of the SimFCS program which was then related to the stacked tiff file the iQ software created. As the real values for the acquisition time differed from the preset values, the tiff file itself could be read to receive the data stamps imprinted in each image of the image stack. The data could then be shifted in time and space and differently visualised to overlap the datapoints. For the analysis, the data could be saved and used to derive msd plots, the corresponding trajectories, instantaneous velocities or also dynamic changes of the msd.

The image processing was mainly done with *ImageJ*, a freeware image program based on Java to evaluate the obtained image stacks. Several freely available plugins such as the Kalman filter, file conversion plugins, stacking processing and View5D, a tracking utility, were applied to analyse the data. Moreover, *Matlab* served as a image processor in cases where *ImageJ* was not suitable due to memory limitations or for the sake of convenience. As the images sometimes had to be changed in stack size and reconstituted, a program could shuffle the stack of images. A program could even be used to imprint labels and timestamps according to the times derived from the timestamps.

CHAPTER 6

Calibration and Characterisation

To achieve proper tracking, the setup was carefully aligned and calibrated. Since the setup was completely built in our laboratory, some issues elucidating the characteristics and the way of tracking will be presented in this chapter. The topics will span from alignment to possible deviations from the theory. Also, later in this chapter a characterisation will be given to show the capabilities of the system.

6.1 Alignment

The proper alignment of the tracking module included the careful adjustment of mirrors, lenses and dichroic mirrors. First, the laser output can be optimised relative to the other widefield lasers. Subsequently, the beam was guided into the fibres to clean the beam shape. Usually, the direct output of lasers, especially diode lasers, has an elliptical profile. This is disadvantageous as it can alter the excitation profile in an unfavourable way. After the optical fibre, the beam has a nice gaussian shape. The beam was then guided into the microscope. On its way, the beam can pass multiple adjustable apertures which are either there to help with alignment or to spatially filter the beam as it is done for instance with the field aperture. A great concern is the proper mounting of dichroic mirrors. Dichroics are coated on thin glass substrates, and they can be easily deformed which influences the beam shape significantly. The less stress that is put on the dichroic, the less the chance of the dichroic deforming. Another way to reduce stress dependent deformation is to use a thicker glass substrate. Finally, the beam enters the objective from the back aperture. On entering, any deviation from an ideally shaped beam will be visible in the sample plane. Of great use was the application of a bulls-eye pattern on a transparency and additional adjustable circular apertures. These items were screwed into the objective holder or mounted inside lenstubes which could then be put into the beampath and provided an additional help to the adjustment.

In addition to a good adjustment of the excitation path, the detection paths must be optimised as well. Since the setup is using epi-fluorescence in both cases, the excitation

and the emission are interwoven. The widefield emission is separated from the excitation shortly after exiting the microscope. It is then transferred to a custom made filtercube which is responsible for the spectral separation of two different fluorophores. These must be correctly imaged on either half of the EMCCD. Also the image must be focussed onto the camera plane. The confocal detection path is very sensitive since the detection path is even more interwoven with the excitation. The beam has to be descanned by the scanning mirrors. Only after descanning, is it possible to separate the excitation and detection beams. A critical part of the confocal beampath is the dichroic mirror separating excitation from emission. A displacement of this component leads inevitably to a complete change, not only from the excitation beam properties but also a misalignment of the detection beam. After separation of the emission light from the excitation beam the signal is passed through a 50:50 polarisation independent beamsplitter which guides two equivalent beams to two different detection paths. Placement of the confocal pinhole needs careful attention. It had to be adjusted correctly in all three dimensions. To find the proper axial position, *Fluorescence Correlation Spectroscopy* (FCS) was used.

6.1.1 Spatial Calibration

Fluorescence Correlation Spectroscopy

For very dilute fluorescent samples, the signal to noise ratio is such weak that it is difficult to extract the signal. In FCS a very dilute fluorescent sample can be analysed [37]. In order to analyse the data, an autocorrelation analysis is performed. The discrimination between noise and signal can be done due to their different statistical behaviour. The intensity of a noisy signal during an experiment is usually random unlike the real signal from the fluorophore. The autocorrelation exploits this difference by comparing different time points with each other. If a signal is present, it will last a while after the first detection. The higher the match, the higher is the correlation of the data. The *autocorrelation function* (ACF) is plotted against time. Then from the shape of the resulting curve, the number of particles and the diffusion time can be derived. For colocalisation experiments, crosscorrelation measurements can also be done.

For the alignment, the ACF can be used to check for the correct position of the pinholes. Hereby the pinhole was moved in lateral position to maximum intensity and an FCS curve taken. The ability to properly fit the data is an indicator for a perfectly aligned confocal pinhole, where the probe volume is defined by the overlap of the pinhole with the excitation volume. Therefore the resulting fit showed how good the pinhole was placed along the optical axis. Only thereafter the lenses focussing the beam to the pinholes were moved on a z-stage and the procedure of lateral adjustment repeated. Finally, when the optimal position in z was determined the equidistant shift of the pinholes was applied resulting in the defocussed detection necessary for the tracking. The pinholes were laterally adjusted to maximum intensity.

An example of ACFs obtained for the two confocal channels with aligned pinholes is

given in figure 6.1. The amplitudes are about the same value for both channels and also the other parameters like diffusion time and structure parameter, which is the quotient of axial to lateral dimension of the detected volume.

Shifting pinholes from the ideal position resulted in a dramatical change of the autocorrelation function. The structure parameter gives an indication of how well the system is aligned and if the detected volumes are similar or not. Figure 6.2 shows two ACFs with significant differences from which it can be deduced that the two detected volumes are not congruent nor do the detection volume overlap well with the excitation. The amplitudes decreased, the structure parameter is changed significantly and the fitting did not work well. The ACF method reveals displaced pinholes but does not work to evaluate their position. With dynamic tracking the position of the pinholes can be revealed. A fluorescent particle was immobilised on a coverglass and placed on a piezo-stage. To determine the position in x and y , the two intensities of both channels were added and analysed using a *Fast Fourier Transformation* (FFT). If one pinhole is addressing a laterally shifted volume, that means both detection volumes are not perfectly aligned on top of each other. Figure 6.3 shows a result of such misaligned pinholes. Any movement in lateral direction x and y leads to a deviation in axial direction and is a direct result from misaligned pinholes. This behaviour occurred frequently when the setup was left overnight. Therefore, the setup was adjusted each morning before starting an experiment. Moreover the figure shows deviations which can be explained with the concept of the *physical angle* (PA).

Physical Angle

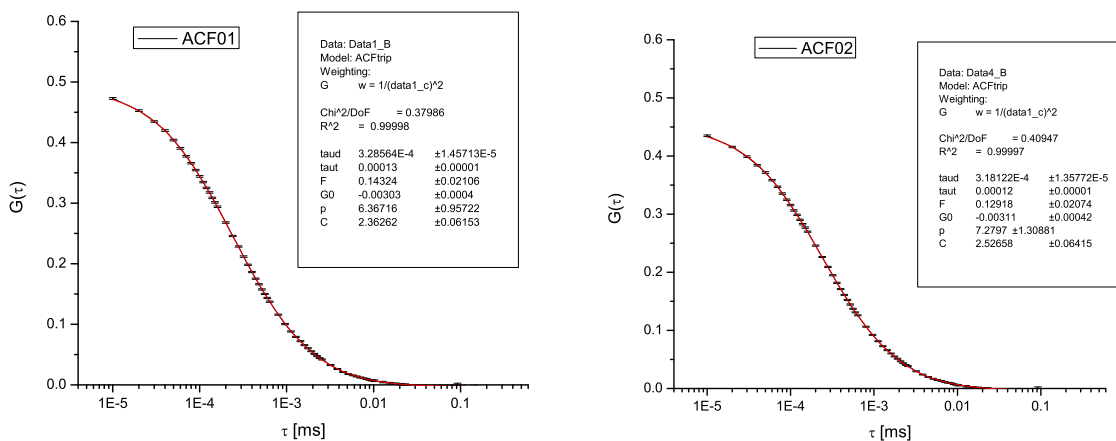


Figure 6.1: Two autocorrelation functions resulting from the two confocal detections. The values for the fitting parameters indicate a correct alignment of the confocal pinholes

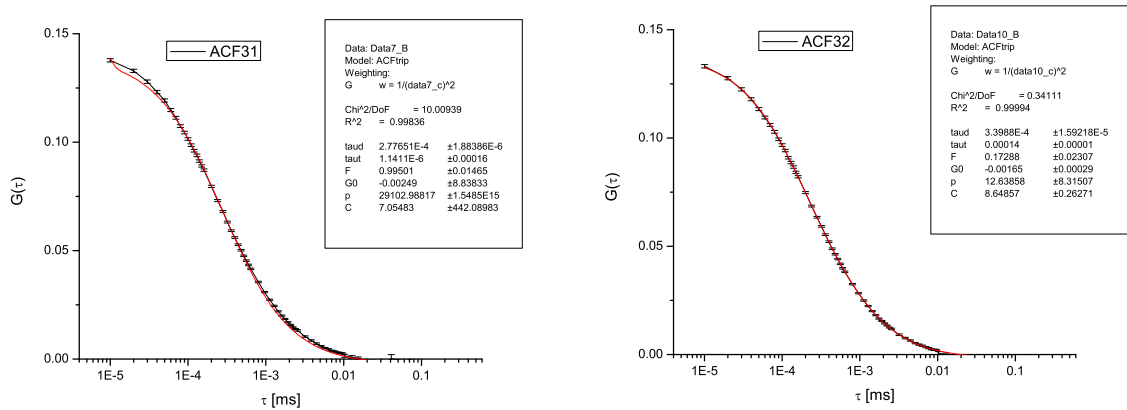


Figure 6.2: The autocorrelation function changes significantly if the axial position of the confocal pinholes is shifted to positions different to that of the excitation volume.

The PA defines the rotational difference of the tracking algorithm to the real world. An arbitrary start point of the SimFCS software defines the zero angle of the system. This does not necessarily coincide with the zero angle of the mirror control. For that reason, the direction of the acquired next position deviates from the actual position and results in a spiral movement of the tracking. Figure 6.3 shows the deviation from right-angles in the lateral projection. Clearly the lines which are supposed to be straight are curved which is a result from an incorrect PA. To account for the deviation it is also possible to measure the deviation by placing a fluorophore particle at a defined angle and look on the intensity trace of the orbits, to find out the angular shift. A closer look on fast moving particles can also help determine the PA by reducing any curvature in straight trajectories. With the correct setting for the PA, the lateral projection in the second image of figure 6.3 shows straight lines. Moreover if the pinholes are also correctly adjusted, the tracking of the three-dimensional LMU-logo shows a good position accuracy in all three dimensions without any deviations. In the rightmost image in figure 6.3, the LMU-logo is properly resolved. Each projection shows a clear movement of the tracking without any loops or kinks.

Mirrors

The piezo-mirror responsible for the lateral scanning of the beam was 10mm in diameter and 2 mm thick. Although the mass is not large, the inertia of the mirror running at frequencies up to 125 Hz is significant. However, it can be accounted for in the tracking routine as a reaction time following these equations for the amplitude A and the phase ϕ :

$$A = A_0 \frac{1}{\sqrt{1+\omega^2\tau^2}} \quad \text{and} \quad \phi = \phi_0 + \arctan(\omega\tau)$$

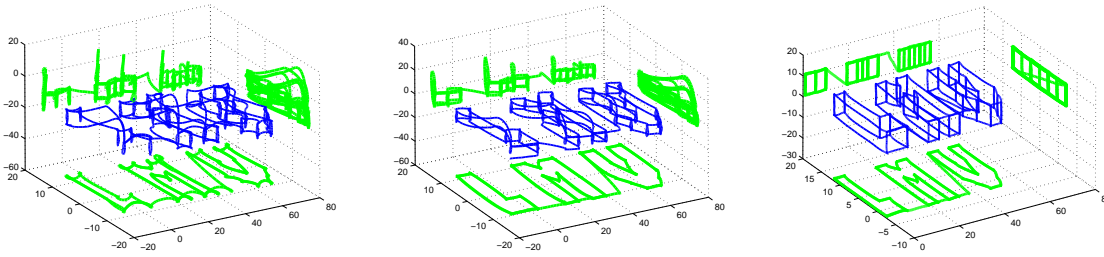


Figure 6.3: The influence of the physical angle and the adjustments of the pinhole. A three-dimensional LMU logo was scanned. The first image shows an example of incorrect pinhole adjustment and physical angle. Correcting the physical angle leads to the image in the centre. The last image is a perfect alignment of the pinholes and the PA

then omega results to:

$$(\omega\tau) = \sqrt{\left(\frac{A_0}{A}\right)^2 - 1}$$

which can then be implemented into the program [9]. The inertia of the objective positioner can be evaluated in a similar manner but was not necessary due to the speed of our instrument. The movement of the objective was an order of magnitude slower than those of the mirrors.

Illuminating Beam Diameter Implication

A theoretical calculation showed a possible effect on the intensity distribution at the focus caused from different beam diameters. A laser or any light bundle cannot be focussed into a single spot due to the laws of waveoptics. The focus follows an intensity distribution which can be calculated by the Lommel functions. The beam aperture plays a significant role in the way the laser is focussed into the volume. Since the back aperture of the objective can be seen as a spatial restriction of the beam, waveoptics tells us that diffraction is inevitable. A calculation of the intensity distribution at the focal plane shows that for a high "beam diameter"-to-"aperture opening"-ratio, the intensity forms non-uniform patterns which finally ends in the distribution Lommel firstly derived in 1885 [36]. The irregular pattern throughout the volume with its maxima and minima could influence the tracking routine. With the drawback of a wider focus diameter a lower ratio was chosen, which smoothed the pattern as it can be seen from left to right of figure 6.4. The intensity variations at the focal plane shown in logarithmic scale are calculations based on formulas derived by Born, Wolf, [8] and expanded by Horvath [24]. They were implemented in MatLab and showed different intensity distributions at the focal plane depending on the incident beam diameter.

Confocal Filtering

The shifting of the pinhole is an essential concept in this setup. In order to better understand the consequences a pinhole shift has along the optical axis, matrix raytracing calculations have been done. The matrix methods in optics, also called ABCD method, is a common way to trace the track of individual light rays passing through different optical elements. This techniques implies the *paraxial approximation*, where the ray is close to the optical axis at small angles that the approximation $\sin\theta$ yield θ . Then every starting vector for the lightray is transformed via a transfer matrix to the end vector in the following manner:

$$\begin{pmatrix} x_{end} \\ \theta_{end} \end{pmatrix} = M \cdot \begin{pmatrix} x_{start} \\ \theta_{start} \end{pmatrix} = \begin{pmatrix} A & B \\ C & D \end{pmatrix} \cdot \begin{pmatrix} x_{start} \\ \theta_{start} \end{pmatrix} \quad (6.1)$$

x [m] : Distance from optical axis
 θ [m³] : Angle
 M [s] : Transfer Matrix or ABCD matrix

The transfer matrix describes the element, which modulates the incoming or starting ray. Different matrices can be used for example to describe a distance in vacuum, a thin lens, or refraction and reflection:

$$M_v = \begin{pmatrix} 1 & d \\ 0 & 1 \end{pmatrix}; M_l = \begin{pmatrix} 1 & 0 \\ -\frac{1}{f} & 1 \end{pmatrix}; M_{refr} = \begin{pmatrix} 1 & 0 \\ 0 & \frac{n_1}{n_2} \end{pmatrix}; M_{refl} = \begin{pmatrix} 1 & 0 \\ 0 & 1 \end{pmatrix}; \quad (6.2)$$

Based on these equations, the rays coming from the region of the focus were traced to the confocal pinhole. Figure 6.5 shows the calculated raytraces for the tracking system of this work. The raytracing routine was created with MatLab. Keeping in mind that there will be deviations from experiment as paraxial approximation is not always valid, the calculated rays give an indication of possible variations. Here, the originating rays

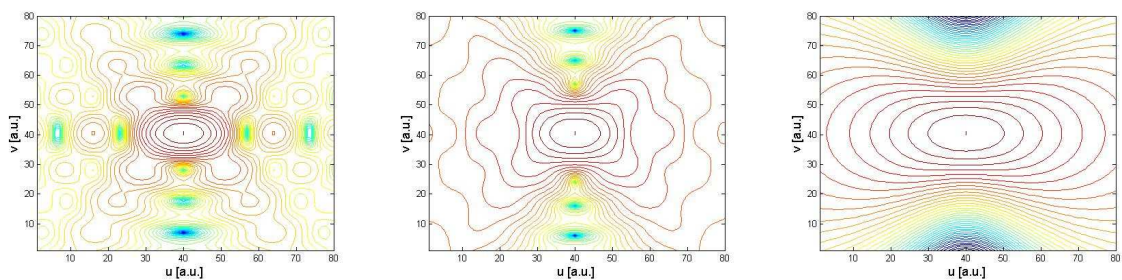


Figure 6.4: Intensity distribution at the focal volume for different beam diameters: Half the back aperture size (35mm), back aperture size (70mm) and without obstacles equals in the distribution derived by Lommel.

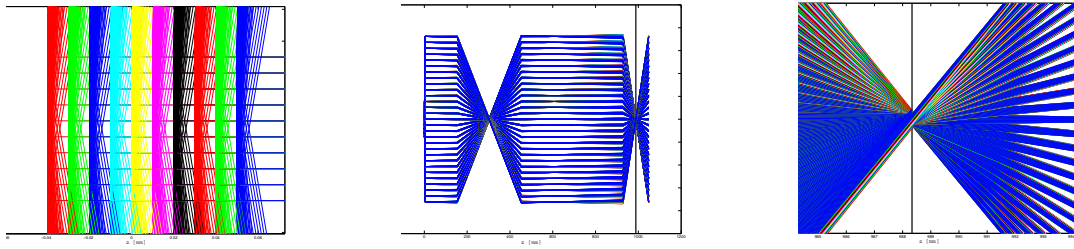


Figure 6.5: Raytracing via Matrix methods. The centre image shows the complete confocal setup construct. (Left) a closer look on the focal area; (Right) on the PH area with the pinhole in black. The pinhole is placed at the conjugated plane of the focus.

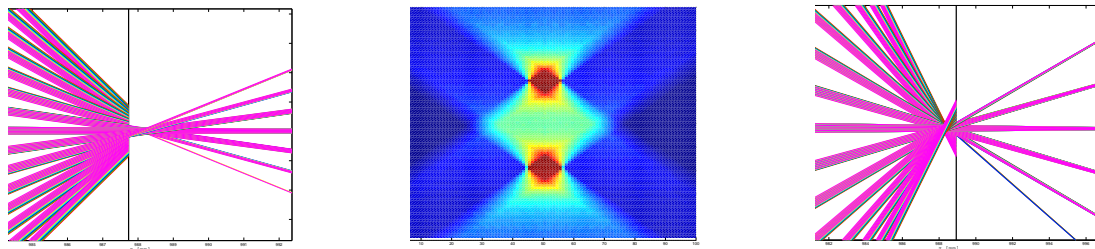


Figure 6.6: The rays falling on decentred PHs and the resulting detection areas calculated with raytracing techniques

from the focus region are plotted on the left. The centre shows the complete geometry of the system in the direction of the detection from left to right. To the right, the principle of a common confocal setup is depicted, namely that only light originating from the focal plane is passing the pinhole at the end of the raytrace. With a geometrical approximation, the left image shows an equal distribution of ray origins with different opening angles. These rays are transferred through the optical system to the confocal pinhole shown on the right hand side. It can be seen that most of the rays pass the pinhole and only a few are blocked by the pinhole. For this tracking method, it is required that two different planes in the sample are observed. To transpose this idea to the given setup, the confocal signal was split into two separate detection channels each equipped with its own confocal pinhole. It can be deduced from figure 6.5 that a shift of the confocal pinhole along the optical axis will restrict different rays emanating from the focal region. The two framing images of figure 6.6 show the properties of two equidistantly shifted pinholes at a separation of $\pm 0.6\text{mm}$. It can be seen that different rays can now pass the pinhole. As a result of the shifting of the pinholes, the detected intensity and the area at the focal plane can be changed. To evaluate the area which is being detected, the number of passing rays was calculated with raytracing. The result is presented in

the centre figure 6.6. Assuming a detection from above the two bright spots give the detected areas in the focal region. The lower red region is the area of a shifted pinhole further away from the setup. It can be seen that the centres of both areas do not overlap with the actual focal spot. A closer look on the distribution also reveals a dependency of the detection efficiency assuming this pure geometrical analysis. The lower spot is larger in area and closer to the ideal confocal position. The reason is the non-Köhler or non 4f alignment of the detection path which leads to a difference of the detection efficiencies. Nevertheless, the shifting of the pinhole gives an access to different planes in the sample.

The passing light was first collected by a lens which imaged the confocal spot to the sensitive spot on an APD. However replacing the lens with an optical fibre with a core diameter of the size of the pinhole greatly minimises the effort in adjusting the confocal detection. Since the fibre is attached to the detector, no tedious readjustment of the detector had to be done as it was the fact in the lens case.

g-Factor

The g-factor was introduced to account for the different detection efficiencies of the two detection channels. The g-factor adjusts the intensity of the first channel to the second channel, which then can support the accurate positioning of the objective according to the particle position. To measure the g-factor, tracking with one channel was enabled and the ratio of the DC values of the two channel resulted in the g-factor. In later experiments it was chosen to be one as the different detection volumes and an asymmetric PSF resulted in further concerns about unexpected effects impeding the tracking.

6.1.2 Synchronisation

The synchronisation of the two parts, confocal and widefield, is a prerequisite for the following experiments. The synchronisation can be subdivided into two parts:

1. Spatial Synchronisation
2. Temporal Synchronisation

1. Spatial Overlap of the Widefield and Confocal Setup

The spatial synchronisation is necessary in order to monitor overlapping regions in both channels, widefield and confocal. After aligning the system, the spatial dimensions of the confocal system had been evaluated. The concern of the confocal system is connected to the scanning mirror which is placed behind the microscope in a 45° angle and rotated 45° relatively to the mirror axis to overlap the x and y direction. The tracking information gained from confocal detection is to be seen in relation to its surroundings, hence an ideal overlap with the widefield is desired. Three criteria fulfil this overlap. The area has to be of the same size, the same axes aligned, and has to be positioned to the same point. For this purpose, the widefield system was taken as a reference to move a multi-fluorescent particle to the borders of the widefield detection through a piezo stage. At the same time, the scanning was activated and followed the particle. The potentiometers regulating the output voltage were correcting for the different amplitudes of x and y. The source of this deviation is resulting from the 45° position of the mirror. In the first approximation, the influence of the axis along the beam direction was about twice as much as the perpendicular dimension, because of the reflection angle doubled along the beam direction. However, from the adjustments a correction factor of about 1.5 times was reached to cover the same length of a given a squared scanning area. To overlay the observed area, the centre of the confocal was overlaid with the widefield centre. This deviation was extremely sensitive and could only be evaluated with an estimated error of one to two pixels. The errors resulted from the position determination of the particle from the widefield image, the tracking accuracy and the sensitivity of the offset control of the piezo. This value was decreased in the post processing of the images together with the obtained trajectory. In total the x and y voltages covered about 17.0% of the maximum deviation in x and 12.6% for y.

What also has to be considered was a transformed plane of the confocal scanning. Figure 6.7 left panel shows a possible deviation of the plane determined from simulations using a povray program of Peter Schwaderer. The diverse dependencies of x and y are responsible for a deviation from an ideal regular rectangular scanning field. However, these images were calculated with much higher angular deviation than applied. In fact, it came out experimentally that moving the laser along this trajectory did not lead to deviations from the ideal rectangular field. There is no curvature of the field and no scaling in both x and y as shown in figure 6.8. Also, a circle is not distorted. The image on the right shows a sample trajectory of a tracked bead which was moved in enlarging

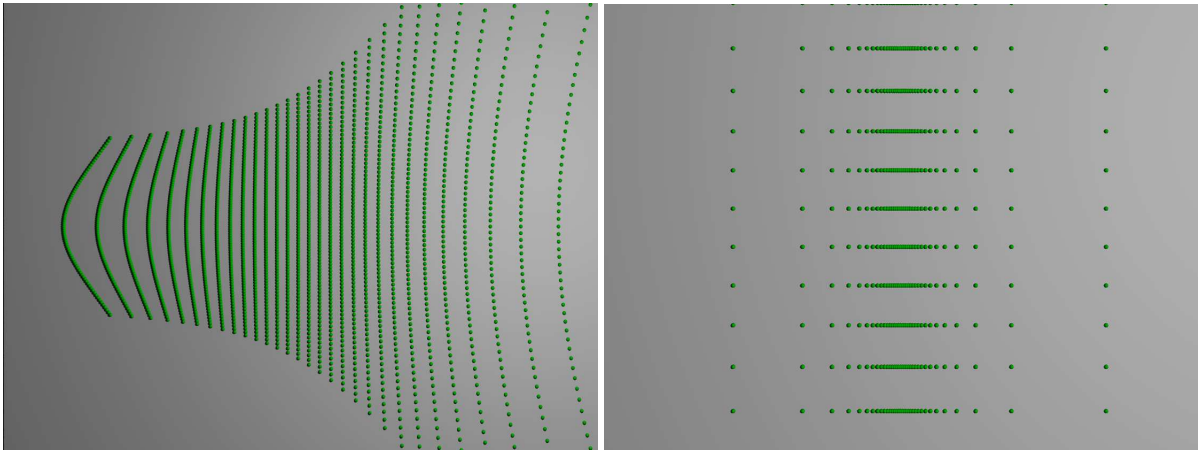


Figure 6.7: Deviations from a uniform rectangular scanning field for large angles with A) one mirror and B) with two mirrors. (Courtesy of Peter Schwaderer)

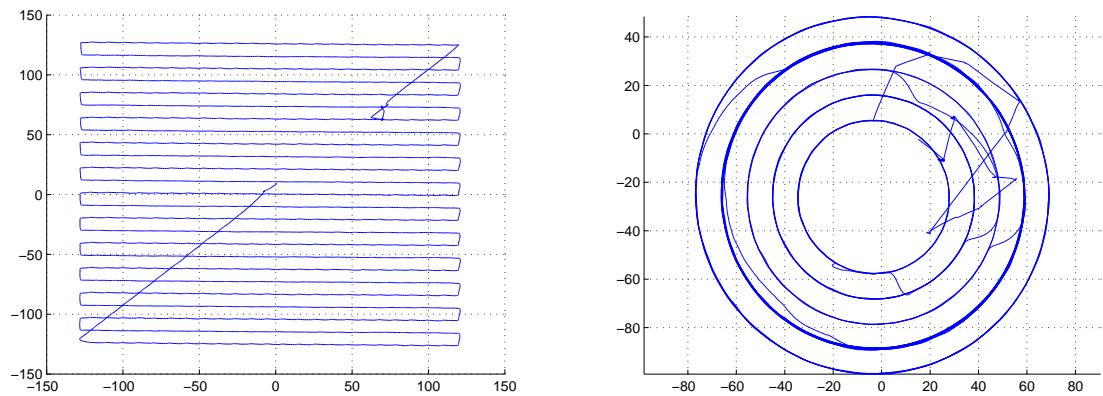


Figure 6.8: A meander scanning the area to determine a deviation from the ideal rectangular non-scaled field. It shows no significant change. The image on the right shows a non-elliptical circular scan of a trajectory.

circles. Any deviation would especially show up at the borders of the field. In both examples it can be seen that the tilt angles were apparently small enough to not see the slight deviation from the square.

The third dimension has to be considered in a different way. In the axial direction, the optical resolution is lower than in the lateral dimension. The spatial overlap for the axial dimension has to be provided so that the z -planes of both methods coincide. To assure the spatial overlap of the widefield and the confocal in z , images were obtained with both methods. Fluorescent beads of $6\ \mu\text{m}$ diameter from Invitrogen were immobilised on a cover slide and measured with the confocal system. The beads are composed of

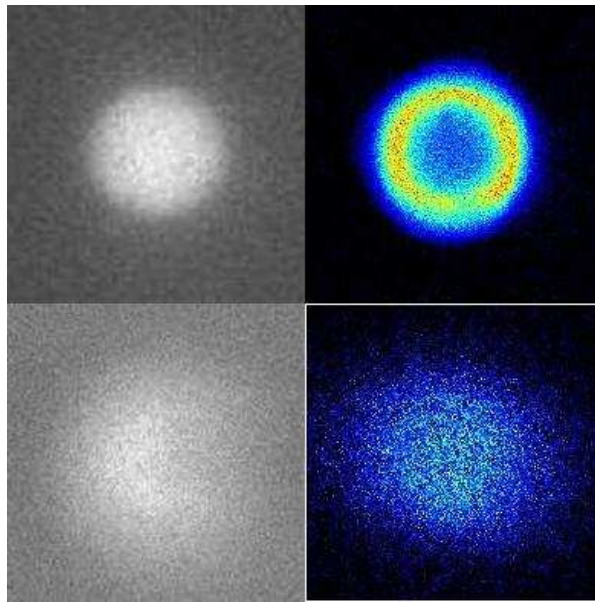


Figure 6.9: The widefield image (left) and the corresponding confocal image (right) showing a nice overlay of both of them. The upper images show a $6\ \mu\text{m}$ bead in focus, the lower show the bead out of focus.

two different dyes, a red dye staining only the surface of the bead and a green dye for a throughout staining of the bead. Figure 6.9 shows the widefield image on the left hand side and the corresponding confocal image on the opposite side. In the upper row the bead is in focus, the lower row shows the bead out of focus. In a correctly adjusted system, the focus of both widefield and confocal coincided. The widefield image was in focus when the bead shows sharp edges and is smallest in size. A deviation from that focal position leads to a blurring where the beads dimensions look larger. The confocal image clearly shows the ring structure of the bead. When the ring structure was its largest extension, the focus of the confocal system was centred on the bead. Since the axial resolution is not as univocal as in lateral direction, the overlaying was also repeated with smaller bead sizes of 170nm which lowers the ambiguity of the true z -position. This method was pursued in the next temporal synchronisation part.

2. Temporal Synchronisation

The software SimFCS controlling the tracking did not include a possibility to synchronise with the widefield. Therefore, the synchronisation was made manually. Since the two systems were installed on two separate computers, the starting was done manually with each hand controlling either program. However a program starting delay and other operating system inherited delays like irregular image acquisition times can easily lead to values in the range of the confocal tracking. Despite the acquisition issues, meth-

ods and acquisition frequency differed between widefield and confocal which had to be synchronised. Therefore, a second correction was introduced by a post-treatment of the measured data.

The signal obtained from the confocal system is based on an intensity trace which is related to the mechanical movement of the mirrors and gives the position of the tracked particle. The time base is in the range of a few tenths of milliseconds and is therefore much shorter than that of the widefield. The widefield data shows a complete image and gives an indication about the particles current position. Since the image acquisition was highly irregular with deviations to the preset acquisition time of more than 50%, an additional time stamp of the time of harddisk access imprinted onto each image was readout. Still, it has to be considered that the imprinted time stamp was raised after the images was written on the harddisk which does not necessarily coincide with the time the image was taken. An external trigger and a lower acquisition frequency can lower the errors which can occur. With the tracking data and the image on the widefield setup it was now possible to overlay the data of both acquisition types by looking for lateral movement of the particle which can be seen in both channels. Obstacles the acquisition, that should be considered are the amount of images in one stack, the bleaching rate and the limits of the tracking program. The maximum number of datapoints is 50.000 that could be obtained with SimFCS. The common settings were 16 or 32 ms for the feedback loop. For widefield acquisition, this was between 200 to 500 ms per image with up to 1000 images.

6.1.3 Calibration Curve for spatio-temporal correction

The calibration curve acts as a look-up table for the tracking system and relates the incoming signal to the particle position relatively to the centre of the orbit. As tracking is not only concerned with accurately measuring the position of the particle but also following the moving particle, careful consideration of the correct curve fitting to the system is necessary. In the case of a moving particle, the measured signal deviates from the fluorescence response of a immobile particle and should be considered for the tracking. Also in most cases, an incorrect correction curve is unable to follow the particle correctly. Different calibration curves have been applied to empirically find the correct setting. Figure 6.10 shows an example of different calibration curves for the z dimension and shows the effect on the tracking accuracy. For this example, a particle was sinusoidally moved along the dimension of the calibration curve. The tracking was analysed by fitting a sinusoidal curve to the derived trajectory. The derived amplitude is decreasing with increasing speed of the particle. It gives a clear evidence of a calibration curve which is unable to follow the particle under the same tracking conditions. The imprint of a correct calibration curve is thus important for a high tracking reliability. Also shown is the standard deviation of the error of the tracking positions to the fitting curve. Only for the blue curve where the amplitude is correctly kept, the standard devi-

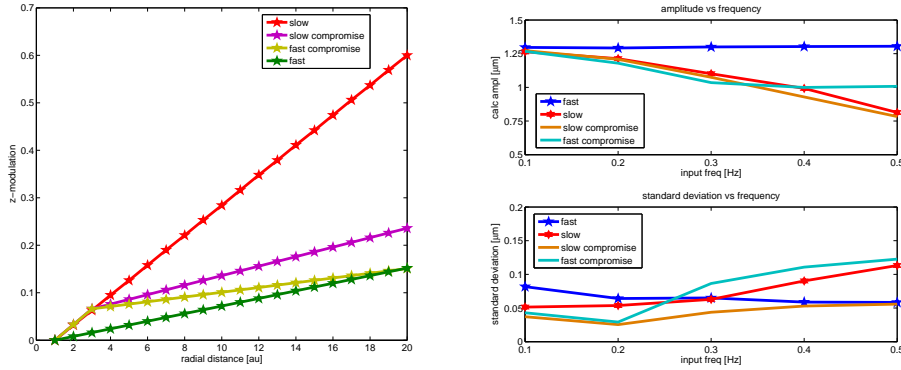


Figure 6.10: Calibration curves (left) and the effect on the dynamical accuracy - Amplitude (upper right) and standard deviation (lower right).

ation gives a trustworthy value. The other values are insofar misleading as the fit does not represent the true trajectory. When the amplitude decreases, the tracking does not work, i.e. it cannot follow the particle through its entire journey. The experiment shows that the accuracy is dependent on the calibration curve and moreover on the dynamical characteristics of the system.

A problem occurs when the particle moves out of either one of the two pinhole planes. The system is then unable to determine the particle position correctly since there will be two positions with the intensity values used to track the z -position of the particle. As a result, the system lags behind the particle. It can be seen in the amplitude values that for faster particles, the system does not reach the maximum amplitude. The temporal lag is still present when the particle already turned backwards.

A larger shift of the pinholes reduces this problem. In the first instance, a shift enlarges the range in which the particle's position can, in principle, be determined correctly and thus is positive for the following of the particles. However, it also leads to a reduction of the collected fluorescence signal. Hence, shifting the pinholes can lead to a decrease in the accuracy of the system. In addition, the system will be more rigid to fluctuations of the intensity resulting from photon noise which improves the accuracy of the system for slow moving particles but becomes worse for fast dynamics. Moreover, the *signal-to-noise ratio* (S/N) will decrease significantly. Therefore, it depends on the particles brightness and photostability whether one chooses, to shift the pinholes further away.

6.2 Setup Characterisation

To benchmark the capabilities of the setup the widefield image acquisition was included for the test measurements, where an immobilised bead was placed on a cover slide.

Multi-fluorescently labelled polystyrene beads with a mean size of 170nm were used and were moved with a piezo-stage along a circle tilted in space. The trajectory of the movement is shown in the first row of figure 6.11. Four images from the movies were extracted and presented below the trajectory. With conventional widefield microscopy, the particle inevitably moves out of focus. It is initially visible only as a faint signal then it approaches the focal position in the third image and continues again out of the focus. With our tracking system, the objective was always repositioned according to the beads current position. As seen in the lowest row, the particle moves in x and y but does not move out of the focus. Of course, the information about the axial position is saved in the data obtained from the tracking system. This data can be retrieved and visualised later.

The dynamic example given here does not only demonstrate the overlapping of the focal planes of the two detection systems, but allows determination of the temporal synchronisation. The system is delayed more than one tracking cycle. The lag of one tracking cycle is an intrinsic property of the feedback method. The system first measures the intensity after which the position is derived and is therefore one cycle behind. An example measurement where the particle was moved on a tilted circle trajectory was used to

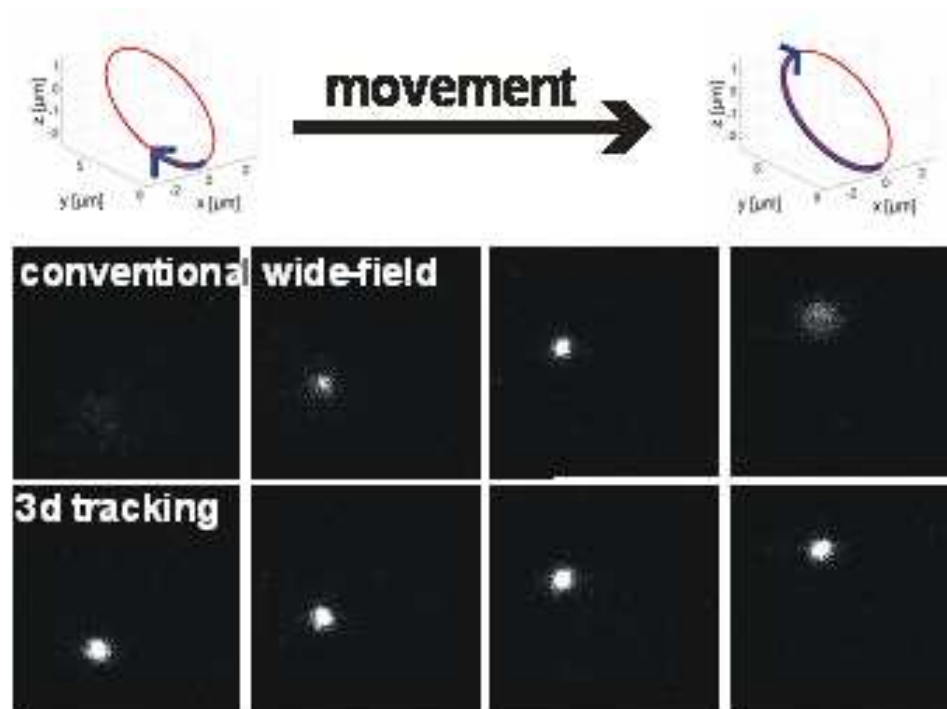


Figure 6.11: Proof of Principle: Conventional widefield images of a bead moved in a trajectory shown above (upper row) taken with the tracking system switched off (middle row) and on (lower row).

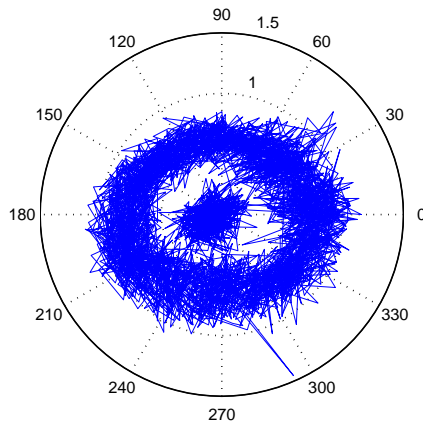


Figure 6.12: This plot shows the radial and angular variation of the experimental data compared to the fitted sinusoidal trajectory. This post-analysis of the circular trajectory reveals a deviation from the centre which results from the lag time of system.

obtain the data shown in figure 6.12. The intensity trace of the two channels were used to manually obtain the particle position as a function of the angular deviation and a relative distance from the centre. The spot at small radial deviation shows the moment when the particle is resting and the tracking does a static measurement and implicates the stability of the system. As soon as the particle moves the derived position moves, out from the centre and the ring-like structure becomes visible. This results from the systems inherent lag which can only be decreased by accelerating the acquisition speed.

6.2.1 Tracking Speed and Accuracy

To test the accuracy of the tracking system as a function of the dynamic properties of the tracked particle, the beads were moved and tracked at various velocities. A 170nm fluorescent particle was immobilised by spin-coating the particles on a clean cover slip. The sample was mounted on a piezo-stage and fixed with an another microscope slide. The sample was then moved in a sinusoidal way in the lateral and axial directions. An amplitude of about $1.3 \mu\text{m}$ and frequencies of up to 0.8 Hz were tested, which gives a maximum velocity of $v_{max} = 6.54 \mu\text{m}/\text{s}$. The obtained trajectory was analysed by fitting a sinus function to the data and comparing both the amplitude of the trajectory and the deviation of the fit to the tracking points. The advantage of this method in comparison to

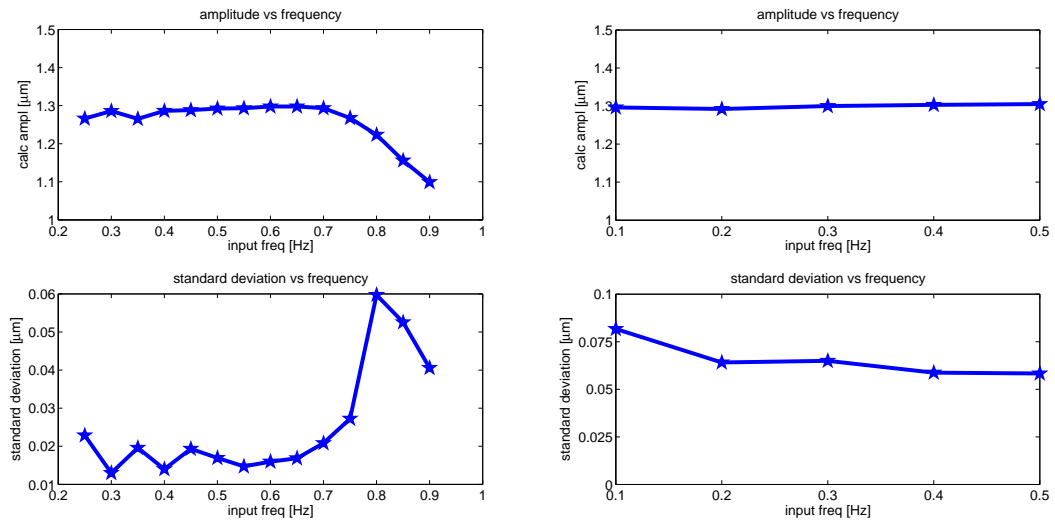


Figure 6.13: Tracking Accuracy xy (left) and z (right) for slow and fast movement

staircase tracking [34] is the incorporation of the velocity which is important to evaluate the system for dynamic processes. As the mode of detection for movement in xy and z are different, the accuracy and resolution were measured separately. Figure 6.13 shows the outcome of this experiment. In the left panel, the radial component was tested. The amplitude stays constant until 0.7Hz when it begins to drop. The error of the fit stays around $\pm 20\text{nm}$ until 0.7Hz above which the error increases. The maximum velocity at 0.7Hz corresponds to $5.7\mu\text{m/s}$. Up to this value, a radial movement of the particle can be accurately followed with a precision of 20nm. The accuracy for z is inferior to that of r and is about 70nm as can be seen on the right panel. Loss of a particle in the radial direction has a binary dependency, meaning that either the particle can be tracked or not, while, for the axial direction, the accuracy decreases, but, because of the nature of the axial tracking, the particle won't be lost so easily. Whenever a particle moves out of the scanned area of the pinholes, the system is still able to follow the direction of the particle assuming that the particle can still be tracked in radial direction. This underlines the power of this tracking method: The axial robustness is especially useful for experiments on a longer timescale. A simple post-processing of images to obtain the particle position for movements as it is shown in figure 6.11 would inevitably lose the focus and thus the capability of tracking.

CHAPTER 7

Applications

In order to apply the tracking microscope to a biological system, two experiments were conducted. First, the system was tested to observe the transport of labelled DNA-polyplexes along the microtubular network of the cell. The DNA-polyplexes can be utilised as gene vectors to shuttle external nucleotide sequences into the cell nucleus where they can be incorporated and transcribed in the cell. Investigations of the transport dynamics of these particles helps increase our understanding of the mechanisms of transfection with gene vectors. It is advantageous to see the transport in combination with the structure component. With the newly developed tracking system, the dynamics of the transport process as well as the interaction with the surroundings could be visualised.

In a second application, the system is used to correct for focus loss that often occurs during long-time measurements. Currently the only way to re-establish a correct focus was determine the distance to the cover slide and keep it constant. In perfect focus systems provided by commercial microscope suppliers, a near-infrared laser is guided onto the cover slide. The reflection is detected from which the system calculates a focal shift. It resets the system by moving the focus to the correct focal position. Using our tracking method the system designed to account for focal shifts which can occur from the sample itself. Stained nuclei were moved by a stage to simulate particle movement in z . The system received a signal feedback to readjust the focus to the sample and thus allows a continuous observation of a sample while it is moving in the axial direction.

7.1 Endosome Tracking

Uptake of gene vectors is an important method for gene therapy. The patient receives a genetic fragment that is incorporated into his own genome. The genetic information is then used to build proteins which would allow her or him to fight an illness. However, suitable gene vectors are difficult to build. Nature has evolved natural gene vectors, i.e. the virus. The virus is a biological structure which lacks the ability to reproduce

itself but is dependent upon a host to replicate further virus particles. Thus, it binds to the plasma membrane and injects its genomic sequence in the cell, which is then often transported with additional proteins to the cell nucleus where the virus genome is incorporated. The virus then utilises the cellular machinery to replicate itself. The virus is therefore the perfect gene vector for shuttling genomic material to the nucleus in order to clone a competent cell. However, the natural shuttle needs careful monitoring since mutations can cause a virus particle becoming potentially harmful. It is also difficult to include any type of sequence into a virus genome.

An artificial approach has been made to overcome this problem. The DNA sequence is packed into polyplexes whose surface can be enhanced with ligands that bind to the cellular envelope and are taken up by the cell. These particles become incorporated into the cell via endocytosis. In endocytosis, the cell absorbs material from the outside into the inside of the cellular envelope and is a mechanism in which the cell can shuttle material through the protecting membrane. After the recognition of the particle docking at the outside membrane, a signalling cascade is started. The incorporated particle becomes surrounded by a small part of the membrane and forms a vesicle. This vesicle contains the particle then fuses with an endosome and is further transported to the inner part of the cell.

7.1.1 Cell Culture and Sample Preparation

HuH7 cells were plated on collagen A-coated 8-well LabTek slides in Dulbecco's modified Eagle's medium:F12 (1:1) with Glutamax I medium supplemented with 10 % fetal calf serum. They were incubated for one or two days (24-48 hours) after splitting at 37 °C in 5% CO₂ humidified atmosphere. Shortly before the measurement, the medium was exchanged with CO₂-independent medium to ensure a proper environment for the cells during measurement in the absence of CO₂. The microscope stage and objective were heated to 37°C.

The DNA polyplexes for the experiments, were build up of plasmid DNA diluted in *HEPES buffered glucose* (HBG) to make up a DNA concentration of 200g/ml. These particles were mixed with *Polyethylenimine* (PEI) and further fused with *Polyethylen glycol* (PEG) to neutralise the positively charged complex. To enhance cellular uptake, the PEI-PEG bundle was modified with *Epidermal Growth Factor* (EGF) [42]. The particles were stored at -80°C. The median particle size of these polyplexes was determined with light scattering to be 248 ± 26 nm and 266 ± 22 nm respectively after thawing. To image these particles with the fluorescence microscope, Cy3 and Cy5 dyes were covalently bound to the plasmid DNA. The labelling was done using the Label IT kits (MIRUS, Madison, WI) according to the manufacturer's instructions [12].

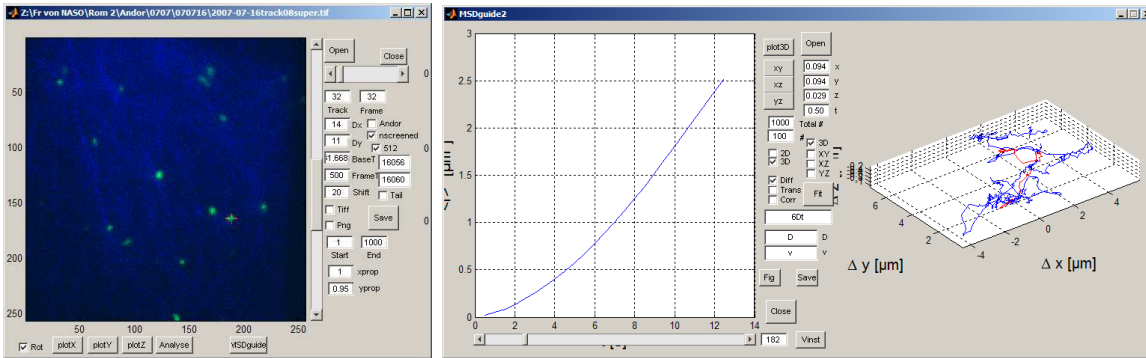


Figure 7.1: Programs: msdGuide and Slider

7.1.2 Experiment

In this experiment, eGFP labelled tubulin of human hepatoma cell line HUH7 were exposed to DNA particles which were manually pipetted onto the cells. The cells were mounted on 8-well labtek slides and fixed on a microscope heater. Thereafter the DNA polyplex solution was mounted on the cell. First, an appropriate cell was chosen with the widefield microscope. These were cells where the cellular skeleton was bright and therefore could be easily seen. The user approached this cell with the tip of the pipette in order to deliver the polyplexes as close as possible to the cell. It was helpful to test the depth to the slide at another place of the chamber and to keep the lasers running during loading. In doing so, the tip of the pipette was illuminated with the lasers if the tip was positioned correctly above the cell. With a quick shot, the DNA-polyplexes were released. After settling down to the cellular membrane, binding of the EGF ligand to the cell was observed as an immobility of the particle. The polyplex became incorporated into the cell itself within a few ten seconds. The double labelled particles were visible in both the widefield (Cy3) and confocal (Cy5) channels. As soon as the particles were visible in the widefield channel, a confocal image was taken. The widefield and confocal systems were started simultaneously. Usually, the signal in the red channel was too weak to track the particle. However, after ten minutes, the particle subsequently fused with others to make larger complexes, which were then traceable with the confocal system. The trajectories were then extracted and analysed together with the wide-field information with custom made programs of MatLab (figure 7.1).

7.1.3 Results

The analysed trajectories could be overlaid with the widefield data and plotted thereafter. Figure 7.2 shows such an overlay with the colour-encoded 3D trajectory for the axial position. It can be seen that the particle moves in the axial direction. The trajectories can further be analysed for their dynamical behaviour. Therefore, msd plots

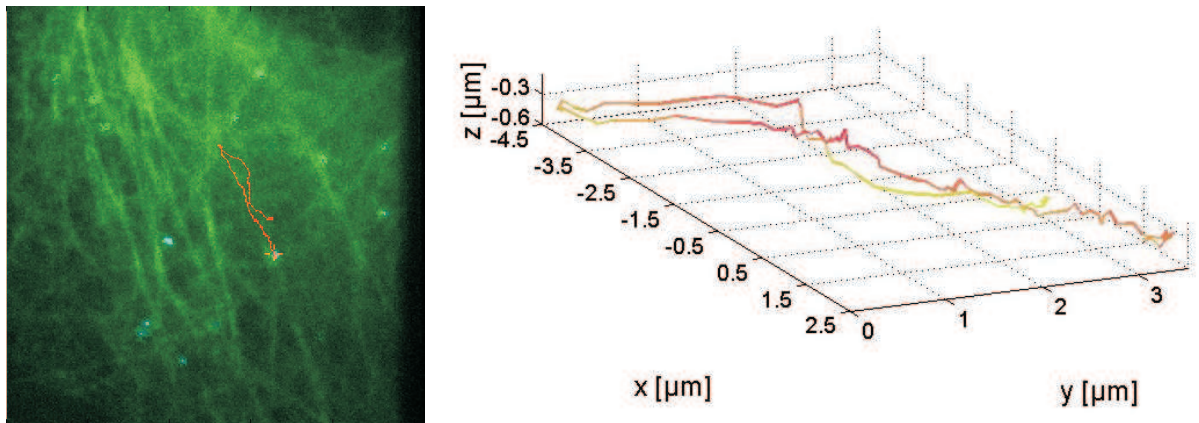


Figure 7.2: Particle Transport along Microtubules. (Left) An overlay of the trajectory with the corresponding widefield image and (right) the trajectory with height encoded coloring.

were calculated to evaluate possible types of motion. The particle underwent all types of motion from random diffusion to active transport and corralled motion. Fast active transport had peak velocities between two and three $\mu\text{m}/\text{s}$. The average velocity was about one $\mu\text{m}/\text{s}$. Since the binning of the msd plots can lead to artefacts, a moving analysis through the complete trajectory was performed. Figure 7.3 shows such an analysis where transport phenomena can be distinguished as yellow to red parts. The development of the msd plot can therefore show changes of the type of motion during a single trajectory. With the support of instantaneous velocities, an interpretation of the movement can be made. However, it was difficult to achieve a clear determination of the boundaries of the dynamics. A clear classification of the trajectory into the motion types depend on the user and should therefore be presented in context with additional data analysis which in total give a conclusive remark on the motion behaviour. Overlay of the widefield with the confocal image allows visualisation of the interaction of the tracked particle in context of the cell. Especially, the double-labelling technique revealed particle switching, where the tracking focus jumps to a second particle, which would otherwise be invisible with simple confocal tracking. Also, the particle was clearly moving along the microtubular network, which was simultaneously changing its own structure. The actual uptake of the particles was not observed, as the labelling of the Cy5 was inefficient and thus, the particle was simply invisible in small amounts in the confocal channel. A possible explanation beside the inefficient labelling is the way the signal is detected in this setup. The detected signal is weaker than for typical confocal systems because the particle is not excited at the laser maximum and the pinholes are displaced. It cannot be circumvent by increasing the laser power because this would increase the effect of photobleaching.

7.2 Focus Readjustment

The technique of tracking can be also expanded to larger structures and also to longer timescales. A common problem which occurs in cell biology is the movement or the motility of the cells themselves. Current techniques are designed to overcome focus drifts resulting from an unstable microscope or stage, but can not account for sample movement. In biology, structures like cells are dynamic. Even if the focus stays on a certain z plane, the cells might move out of the region and focus. The technique presented here is an effective tool which can track cell movement. By following a labelled part of the cell, which is distinguishable from other cells or particles, it is possible to use the method to correct for sample movement. First measurements show the ability of the setup to follow cells even in large z scales up to $100\ \mu\text{m}$.

7.2.1 Experiment

HuH7-tubulin cells were cultivated as described in section 7.1.1. One and a half hours prior to the experiment, the cells were stained with SYTO61 dye. For this procedure, $200\ \mu\text{l}$ of the $400\ \mu\text{l}$ cell culture medium were exchanged with $200\ \mu\text{l}$ of 500nM dye solved in DMSO and the cells put into the incubator again. Fifteen minutes before the experiment, the cells were washed twice and then filled with $400\ \mu\text{l}$ CO_2 independent

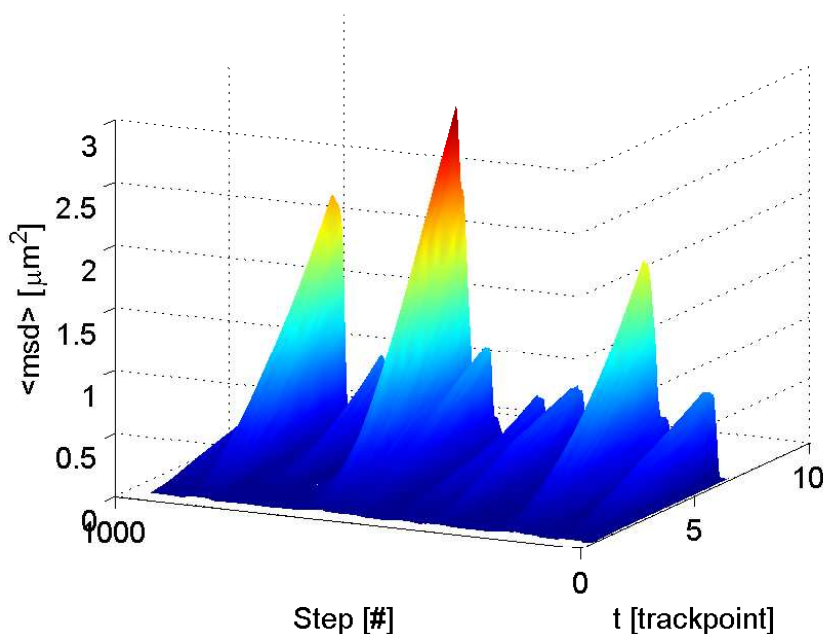


Figure 7.3: 3D msd Plot over a trajectory with a windows of 50 trackpoints

medium. They were then imaged using a piezo-microscope-stage from PI. This stage was capable of moving the sample $100\mu\text{m}$ in x and y and $20\mu\text{m}$ in z . To fit the range of the stage, the scanning range of the program SimFCS was expanded to suit the dimensions of the scanning area. Therefore, the voltage in x and y as well as the voltage in z multiplied. A cell with clearly resolved structure was selected in the widefield channel. The blue channel showed the GFP labelled microtubular skeleton of the cells. Thereafter, a confocal image was obtained to check for the simultaneous SYTO labelling of the cell. The movement of the stage was activated after starting the acquisition in widefield and tracking. The stacks and the trajectories were subsequently analysed using the same custom made programs as previously described.

7.2.2 Results

A cell sample was manually moved with the microscope stage while it was being tracked by the program. Figure 7.4 shows the trajectory colour encoded for time ranging from red to green. The image obtained with the confocal setup is overlain. The three-dimensional trajectory is plotted in the right graph to show the tremendous range of the tracking. The movement can be followed up to $100\mu\text{m}$ in all directions without losing the focus and is currently only limited by the given range of the piezo-nanopositioner.

To ensure that the system is properly focussing on the correct image plane, another experiment was conducted where widefield images were simultaneously taken during axial movement of the cell. In figure 7.5, widefield images with the corresponding trajectory are shown. To test the ability of the refocussing system, the sample was moved approximately $18\mu\text{m}$ along the axial direction. The widefield images show a mitotic cell which was being moved along z . The corresponding diagram shows the actual movement, mea-

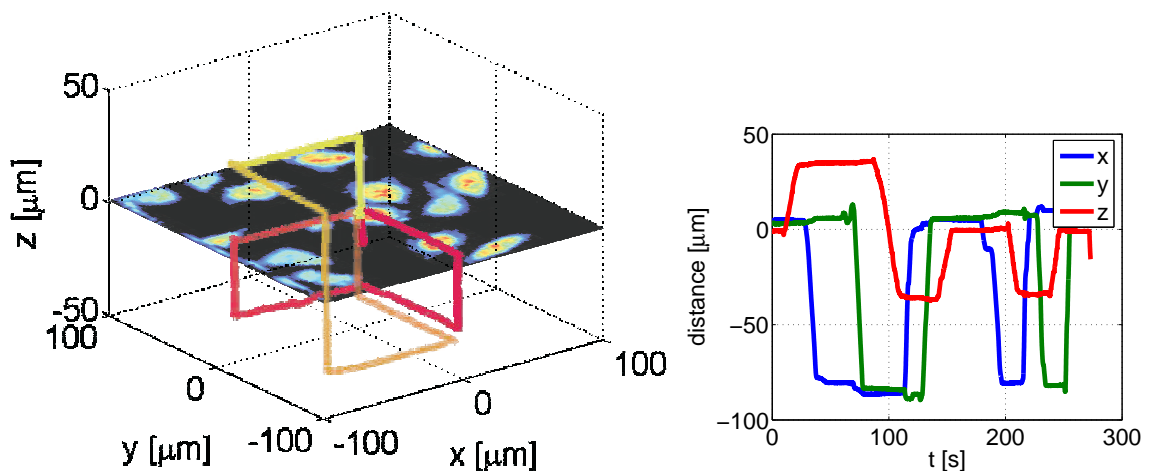


Figure 7.4: The trajectory of a cell moved with the microscope stage along x , y and z with the image obtained with the confocal prior the movement.

sured with the tracking system but the axial movement is not visible in the widefield images. A slight lateral movement is visible, due to a deviation of the stage coordinate system with the scanner coordinate system. Due to the limitations in the range of the piezo-stage, the sample could only be moved about $18\ \mu\text{m}$ and already shows a limit in the lower part of the trajectory, visible as a flat part instead of a hump of the sine. The limit is caused by an un-symmetric installation of the microscope stage.

A larger range can be covered by the tracking system, as the objective piezo responsible for z can travel up to $100\ \mu\text{m}$. Currently, the time scale can be expanded to 1.5h, only limited by the software SimFCS. Future programs can overcome this problem. The only obstacle would then be the photobleaching of the dye. Here it was demonstrated that the accuracy and the reaction speed was excellent to keep a fluorescently labelled biological sample in the focal plane.

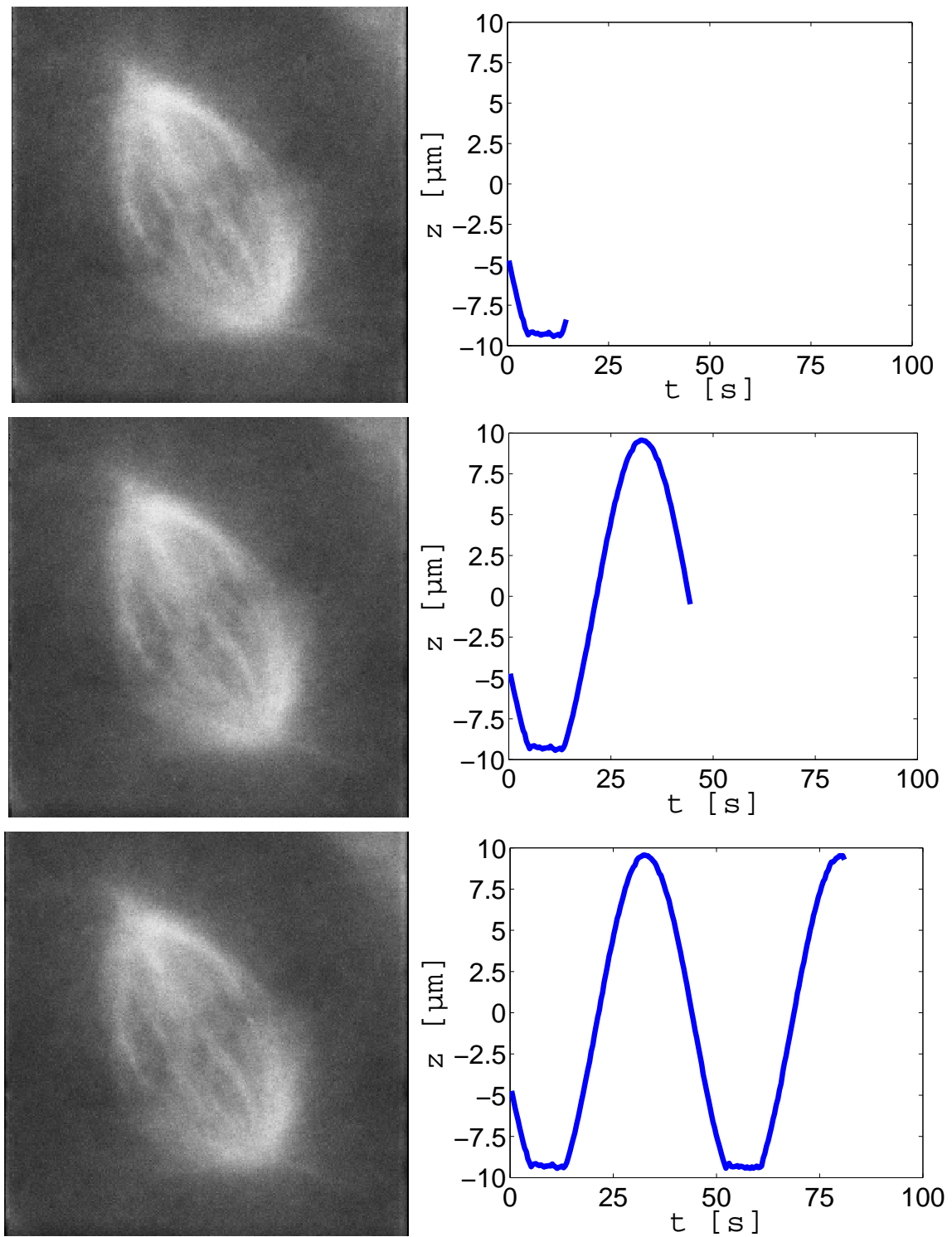


Figure 7.5: Widefield images of a mitotic cell moved artificially with a piezo-stage in the z direction. This movement does not perturb the images. The diagram shows the corresponding axial movement.

CHAPTER 8

Outlook

8.1 Software Improvements

The SimFCS program was written by Enrico Gratton. Although he provided the source code, several program libraries were missing that home-made modifications of the program were impossible. Thus, Prof. Gratton included the modification requests. The next step would be to build a stand-alone software that is capable of controlling the different devices accurately and allows us to direct program improvements to the tracking algorithms itself.

A major limitation of the program was the restriction of the tracking to a maximum time of 1.5h. This made the program not suitable for any long measurements as it would be the case for the refocussing purpose. The experimental conditions during long-term tracking are different in terms of the amount of fluorescence signal and the problem of photobleaching. Therefore, a different tracking scheme has to be developed with for instance includes pauses to lower the exposure of the sample to the laser light. In this case, the timescale is much longer so that the fast FFT analysis of the intensity trace could be exchanged for a real fitting of the fluorescence signal, which can give a higher accuracy.

A Fourier analysis can still be beneficial to analyse dynamical changes of the structure. The second harmonic gives clues to the shape of the signal in the centre. Any deformation from a circle will be visible in the second harmonic. This idea was developed by Prof. Gratton, but is not accessible during online measurements.

As deformation of the image is not only due to the shape of the structure but also result from movement of a particle during one scanning period, the evaluation of the second harmonic can also be used to anticipate the future position of the particle. For typical particle movements, an evaluation of the former positions could be utilised to enhance the prediction power of the system and to smooth the trajectories. Currently, the system is always reacting to particle movement. A sophisticated anticipation routine would help to increase the tracking accuracy for quickly moving particles.

An improved S/N ratio by integrating the photon signal could reveal more detailed information of the structure than Abbe's limit of resolution states, as it has been established in techniques such as STORM or PALM [46] [6].

Currently, the tracking is limited to the borders of the tracking window. Depending on the voltage set for the lateral deviation of the beam this tracking window is fixed in the beginning of each experiment. Similar to the image stacking problem where the particle's movement is anticipated to act only in the preset volume, the confocal tracking can not follow particles moving outside this tracking window. Therefore, it would be extremely beneficial to enlarge the effective area of the tracking by programming the system so that, for instance, the xy stage is coupled to the tracking. The range would then be extended to an area, that is limited only by the physical limitations of the microscope, that is the stage and the focus wheel. Three modes of tracking are imaginable:

1. laser only used for orbiting and stage corrects for the movement
2. laser tracking, but stage reacts, when tracking limits are reached
3. laser used completely for orbital tracking

The power of the system lies nevertheless in the fast tracking of fluorescent particles which should always be considered.

The post-analysis of the data plays a big role. A program which includes the experimental parameters and evaluates the data was basically established. To improve the user friendliness, it would be useful to establish an overall program which combines all fragments of the already developed data analysis. From data import (extracting and converting) and synchronisation to detailed analysis with post-fitting for data verification and trajectory evaluation.

8.2 Hardware Improvements

A difficult task was the synchronisation of the widefield and confocal setup. Controlled by different programs, it was not possible to integrate one program into the other correctly. Both systems were moreover depending on the operating system which allocates the memory and the CPU time. Running on Windows XP, the programs could not run smoothly at the same time. To improve the synchronisation task, a different operating system such as a unix based system needs to be used or a complete stand-alone system. For both solutions, the tracking routine has to be rewritten. An example of a stand-alone beside unix is the real-time system from NI called CompactRIO together with programmable cards called *Field Programmable Gate Arrays* (FPGA)s. This can then be used to externally trigger the shutters, the camera and the confocal detection and put them all together to a global acting program with one global time for each element. The synchronisation is essential for the correct interpretation of the data and was until

now solved with elaborate post processing.

To reduce spectral crosstalk it can be beneficial to use *millisecond alternating laser excitation* (msALEX), where different laser excitations are switched on and off alternatively **??**. The resulting fluorescent signal can be traced back to the excitation source. For overlapping emission spectra, the contribution of the fluorophore to the higher wavelength spectra can then be evaluated. Currently the tracking laser can not be synchronised with the widefield excitation, so that the dyes from the widefield excitation could leak into the confocal tracking channel. To include the switching into the tracking is therefore one issue, where the offtime of the tracking laser also has to be included in the analysis. The switching can however occur more rapidly with pulsed lasers, an *Acousto-Optical Modulator* (AOM) or an *Acousto-Optical Tunable Filter* (AOTF).

The putative drawback of a fluorophore visible in another channel can be also taken as an advantage. Particles excited with 561nm can be partly visible in the confocal tracking channel. Although the tracking accuracy could be worsened, since the widefield excitation does not provide a nice distribution, it is possible to apply confocal tracking with widefield excitation. The tracking can hereby occur simultaneously while the signal can be observed in the widefield. Thus, the tracking and the simultaneous observation can be provided with just one fluorophore. The prerequisites are a strong staining and a well defined choice of filter sets.

If not using a conventional widefield system, a spinning disc confocal microscope can be utilised to give almost confocal z-resolution at high scanning speeds in the range of a conventional widefield. The advantage of the slices in the spinning disc together with the accurate tracking would result in a perfectly focussed spinning disc image. Also since the S/N ratio is greatly enhanced, the sensitivity of the system increases and thus can observe fainter signals. A closer look to the spinning-disc principle is given in chapter 10.2.1.

The confocal detection also gives room for improvements. An additional widefield path is loosely attached to the confocal, by switching one lens and a mirror it is possible to switch from confocal to widefield excitation and guide the signal response to a *intensified CCD* (ICCD). This gives the possibility to have an quick overview image which is more difficult to get from a confocal scan.

As mentioned in the section 6.1.1 in the "Confocal Filtering" paragraph the confocal detection is not a 4f system, essentially a Köhler arrangement of the lenses. The consequence is an asymmetric detection volume. To set the detection to a 4f system, the design has to change as the space is limited. However, that change would implicate a symmetric distribution of the detection.

A problem which frequently leads to focus drifts is the evaporation of the immersion liquid. The slight force due to the surface tension of the water droplet leads to a focal shift which is especially problematic for longer measurement. A possibility is to use a liquid which has a higher viscosity and thus evaporating less but with the same index of refraction. However for tracking purposes this can additionally induce a force to the

sample, when the objective has to follow quickly and squeezes the droplet. Therefore in these experiments millipore water was used. The solution would be a water source which constantly adds water to the droplet so that the amount of immersion water stays the same.

The use of different fluorophores showing a more photostable behaviour and being brighter is always beneficial to the system. The use of quantum dots can be considered, however the qdots are excited also by the widefield excitation lasers. Hence the system response must be carefully observed and tested. Also, qdots are subject of blinking which is unfavourable for the tracking. So, either a photostable environment must be created or a large qdot aggregate which smoothes the intensity trace.

Part II

mRNA Transport in *Saccharomyces cerevisiae*

CHAPTER 9

Introduction to part II: mRNA Transport

In collaboration with Susanne Lange from the group of Ralf-Peter Jansen at the Gene Center in Munich, we studied the movement of individual mRNA particles in the budding yeast *Saccharomyces cerevisiae* with a spinning disc confocal microscope (SDM). We collected z-stacks over time to obtain 3D trajectories from the movement of the mRNA.

The organisation of cellular components inside eucaryotic cells shows a well-defined process of particle sorting during the development of the cell. To ensure a proper functioning of the cell, proteins are needed at specific sites within the cell and throughout the cell cycle. Hereby the proper transport and targeting has to be ensured by the cell. It was suggested that protein sorting is a post-translational process, where parts of the genetic code corresponding to the peptide sequence also encodes the destination of the protein to which it is to be carried by motor proteins of the cellular system. However, in recent studies, another mechanism for the asymmetric distribution of proteins was found which is due to intracellular mRNA transport [26]. In this process, mRNA particles form ribonucleoprotein (RNP) complexes which are transported along the cytoskeleton to specific targets and thereby become localised. Later, the RNP complex disassembles and the released mRNA is translated into proteins. Although it was shown that different mRNA species use the same transport machinery, it was yet unclear how the RNP complexes are formed, whether the mRNA are sorted into the same or different complexes. The aim of the experiments presented here was to investigate the dynamics of RNP localisation during mRNA localisation in yeast by live-cell imaging .

CHAPTER 10

Theory: mRNA Transport

Protein localisation plays an important role for budding yeast during cell growth. The active transport of mRNAs mediates localised translation of proteins from the template RNA at specific sites at which the synthesis is required. The transport of these mRNAs is performed through the cytoskeleton and their corresponding motor proteins, such as kinesin and dynein for the microtubular network and myosin for the actin filaments, which then carry their load to the specific sites encoded in their sequence.

10.1 Cell Biology

Saccharomyces cerevisiae belongs to the family of fungus or mycota. The frugal organism are facultative anaerobes and can therefore be found in various places in nature. For a long time, mankind has used its fermenting capability in various applications in the food industry such as in bakery, brewery but also in vinery companies. Moreover, it is also a popular eucaryotic cell model system in cell biology due to its similarity to the human cell in combination with the easier cultivation and shorter cell cycle. The yeast system can be cultivated in an erlenmeyer flask with culture medium at room temperature. The response time of genetic assays is greatly accelerated since yeast has a doubling time of 90 minutes compared to about 24 hours for many human cell lines. Therefore, it is not a surprise that many homologues of human proteins, were first discovered in yeast. The cells are of spherical shape with a diameter of about 6 μm . The cell cycle differs from that of the mammalian cell cycle and consists of three phases: Budding, Mating and Sporulation. In this work, only the first phase is considered.

During budding, the cell develops a protrusion out of which the new cell is developing. This protrusion is named the bud. The mother cell fosters its progeny by transporting numerous biomolecules to the bud which are essential for its development. The bud grows in size until finally a new nucleus is formed and transferred followed by the separation of the bud forming a new copy of the mother cell. Among those transported biomolecules are mRNAs whose localisation is needed for gene expression.

10.1.1 Gene Expression

Gene expression is the process in which the information of DNA encoded genes is transferred into a functional structure such as a protein or an RNA.

The first step in normal gene expression is the transcription of the gene on a DNA into an RNA by the *RNA-polymerase* (RNA-pol). The transcription is composed of three steps: Initiation, Elongation and Termination. During initiation, transcription factors are recruited to the site of the transcription. This further promotes the recruitment of RNA-pol which initiates the copy process. RNA-pol binds to the specific site, unwinds the DNA and creates a transcription bubble to access the nucleotides. As the polymerase travels along the template strand, it creates a complimentary RNA strand. The structure is similar to that of the DNA. A significant difference though is the exchange of the thymine base with an uracil base. The transcription terminates with the dissociation of the RNA-pol/DNA/RNA complex. Next, the newly created RNA acts as an information carrier. It can travel out of the nucleic membrane into the cytosol and eventually become translated by ribosomes into an amino acid chain out of which the proteins are composed. The amino acids are synthesised by reading the information on the mRNA. Each triple set of nucleotides, called codons, encodes an amino acid. The sequence of amino acids between two special codons, the start and the stop codon, makes the polypeptide chain which after folding gives the final protein.

10.1.2 mRNA Targeting

To maintain the protein polarity inside the cell, proteins have to be localised at specific sites. One common process is the transport of the proteins to these specific sites. However, as mentioned in the beginning of this chapter, a second process involved in protein targeting is the localisation of the corresponding mRNA. The mRNA is transported to the specific site, is released and is translated locally by ribosomes into a protein. Especially during budding, proteins essential for the bud growth are sent to the daughter cell [39].

10.1.3 DNA Transformation

DNA transformation describes a process in yeast and bacteria, where DNA fragments are inserted into a living organism's own genetic code. As a result, the inserted information becomes replicated by that organism and out comes a natural *in vivo* engineered biomolecule. The role model is bacterium which exchanges their genetic material to broaden its genetic variation. In mammalian cells the analogue to DNA transformation is transfection. The transfection is utilised by a prominent particle. The virus can not replicate itself but it is able to reproduce itself by hijacking the cellular replication machinery. The involuntary host produces offspring which produce the new virus particles. Man made transfection can be dated back as far as 1977 when Silvia Bacchetti

and Frank Graham transfected human cells by *Herpes Simplex Virus* (HSV) [2]. This technique is nowadays known as cloning. Since then genetic engineering is a common task in bio-laboratories. Nowadays, the genetic code is inserted into a plasmid, a circular DNA fragment originating from bacteria, via restriction endonucleases. These restriction enzymes are crucial for transmutations as it acts as a scissor to cut double-stranded DNA. Its discovery was honoured with the Nobel prize for the scientists working on that enzyme, Daniel Nathans, Werner Arber and Hamilton Smith. After cutting, ligases put the content of the plasmid DNA fragments and the host DNA strand together, which then becomes reproduced by the cellular machinery. To sort out those cells containing the new information, an additional marker is inserted into the genome. Via either resistance assays or essential nutrient supply, only cells which were transfected with the additional marker can survive. For the non-transfected cells, the cultivating environment is fatal. The plasmid itself is loaded into a carrier, a salmon or herring sperm for instance, and loaded onto the cell suspension. To help the intrusion of the carrier into the cell, the conditions are changed either chemically or electrically, such that the cellular membrane can be permeabilised. Carriers can then enter and eventually transfect the cell. The DNA becomes recombinant and the cell uses the new information to reproduce the protein encoded in the inserted genome.

10.2 Microscopy

Fluorescent labelling of sub- μm large objects is used to reveal dynamics of the processes inside the cellular membrane. The fluorophores are excited by lasers and the emitted fluorescent signal is collected by the objective and transferred to a detector. To have a fast image acquisition, widefield imaging is used where the whole sample is illuminated at once. The acquisition time of one image plane is usually only restricted to the time needed for an image on the field detector to be transferred to the memory. In this system, an Andor iXon+ EMCCD camera with a chip size of 512x512 pixels was used. The minimum full-frame readout time for this camera is given as 32ms. Widefield imaging has the disadvantage that not only the focal plane is illuminated but planes above and below as well. In addition to unwanted bleaching, this leads to a larger background signal from out of focus stray-light. The observed z-slice is confined to an area of some few μm . As yeast cells are about six μm in diameter, the whole cell volume is projected in z and results in a low contrast. One solution to overcome this overlay of different z-slices is to deconvolve the image. The image is the convolution of each point in the sample with the image response function of the optical system, here the microscope. A point like structure is 'broadened' due to diffraction and the result is the *Point Spread Function* (PSF). The 2D width of the PSF can be calculated from:

$$PSF = 0.61 \frac{\lambda}{NA} \quad (10.1)$$

λ [nm] : Wavelength
 NA [] : Numerical Aperture

The PSF is an essential concept in imaging. It explains how point-like structures are transformed by an optical system. An ideal point will not be imaged as a delta function on the detector but, due to diffraction and the inability to collect every photon emitted, the point will follow an intensity distribution. This distribution depends on the optical elements along the optical path, i.e. each optical element between sample and detector. With the knowledge of the system's PSF, it is possible to calculate the original image without alteration due to the limitations of the setup. This procedure is called deconvolution.

$$\text{Image}(x,y) = \text{Object}(x,y) \star \text{PSF}(x,y) + \text{Noise}.$$

By knowing the PSF the calculation the object function can be made. This is a basic concept in imaging. As a prerequisite for deconvolution, the system's own PSF has to be measured. The PSF can be determined by using a point-like source, that is a particle significantly smaller than a least half of the excitation wavelength. The convolution of the PSF with a point gives the PSF itself and thus the PSF is determined. When performing deconvolution, care has to be taken in order to prevent image artefacts resulting from the calculation.

10.2.1 Spinning Disc Confocal Principle

To circumvent the calculation efforts of deconvolution, a laser scanning confocal microscope (LSM) can be used. The confocal microscope limits the off-focus light during the measurement by the confocal pinhole. However, the LSM has to be scanned through the sample and is therefore comparably slow in acquiring images. To overcome the problem of non-focal scattered light while maintaining the speed of the widefield imaging a commercial *spinning disc confocal microscope* (SDM) can be utilised. This state-of-the-art technique combines the advantages of widefield and confocal microscopy by being as fast as widefield with the z-resolution of confocal microscopes. The core part of an SDM is made of two spinning discs also called *Nipkow discs* shown in figure 10.1. The Nipkow disc is designed such that during one rotation of the disc, the holes screen over the complete field of view. Rotating at 30 Hz they consist of a large array of about 20.000 of microlenses and pinholes respectively arranged in a spiral pattern. Each microlens-pinhole combination is a single confocal spot on its own. Because of the arrangement of the pinholes and the high rotation speed of the discs, a whole image can be taken rapidly

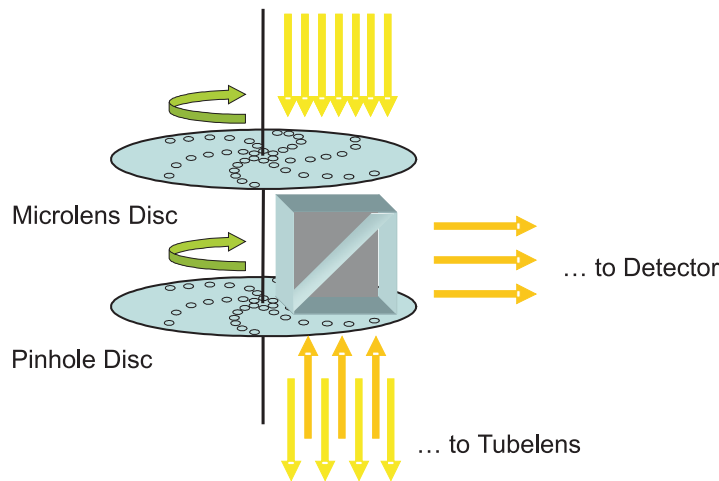


Figure 10.1: Spinning Disc Confocal Principle; The incident light coming from the top passes the microlens disc, which focusses the many rays to the pinhole disc. In between is the filter cube separating excitation from emission light. From the backdetected fluorescent light only the light coming from a selected plane from the focus can pass the pinhole array. This light is reflected inside the filtercube towards the detector. The pinhole disc is placed at the image plane of the system.

when the many confocal spots are scanned over the sample. For one rotation, the disc exposes the detector 12 times and therefore the spinning disc can acquire images with an enormously high speed of 360 frames per second and is only limited by the read-out time of the field-array detector.

A comparison between an image stack taken with a conventional widefield microscope and a similar image stack taken with the SDM is shown in figure 10.2. Apparently, the images obtained with the spinning disc are free from off-focus stray light. Hereby the image shows more contrast and depicts the information of a very thin slice in z . Also, as noise resulting from stray-light is reduced, the overall S/N is improved.

10.3 Image Stacking

The images taken with a widefield system are usually from one selected image plane. To reveal particle dynamics in 3D, the sample has to be scanned in the third dimension, as well. The objective or sample has to be moved to address different planes in the sample. Several images are produced which are stacked to a pile of images altogether representing the observed 3D volume. As the image planes are accessed one after the other, the time for acquiring one of the image planes has to be faster than the movement of the particle itself in order to not lose the particle. The ideal setting is a compromise

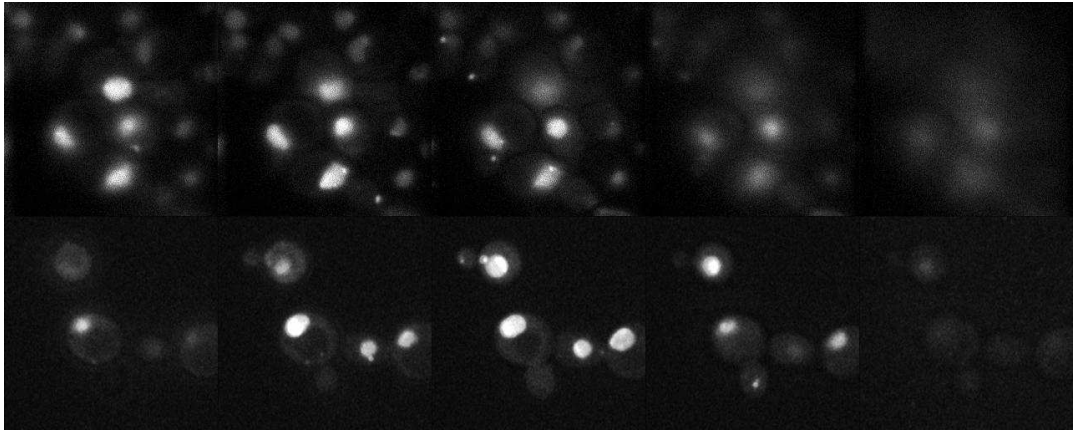


Figure 10.2: A comparison of stacked images of *Sacharomyces cerevisiae*. Each plane is $1\mu\text{m}$ apart from the next. The upper row shows images taken with a wide-field setup on a TE 200; the lower row images taken with a SDM setup. No blurring caused by out of focus light is observed in the latter.

between sufficient coverage of the observed volume and an image acquisition fast enough to reveal the dynamics of the sample. The number and the separation of the slices is therefore determined by the dynamical behaviour of the sample together with the acquisition speed of the system. The stack representing the investigated volume is saved for later image processing. Prior to image processing, careful adjustments for both spatial and temporal deviations have to be performed. Assuming a good colour correction for the focus of the objective, the correction for the planar overlay was resulting from the different beampaths the two spectrally separated beams were travelling. The correction was accounted for the translational and rotational shift and included a scaling factor, if applicable. The slices can then be put together to form a dual-colour image. Furthermore, the speed of the moving parts in the microscope is not infinite. The mass of the objective or the stage slows down the moving process and an artificial pause is set in the acquisition program in order to ensure a correct axial positioning while taking image slices. The movement of the z-plane is hereby set to a sawtooth mode. In doing so, each slice in the image stack will be equally separated in time. The large step at each end of a complete stack raises the necessity of a higher pause. Each image is a confocal image of the sample from a small z-slice in the sample. It is possible to enhance the image quality with any additional knowledge known from the system. Special care and attention is necessary in order to not alter the image content. As a rule of thumb, any enhancement of the image should be applied to every part on the image without any restriction. Afterwards it is possible to calculate a 3D image by putting the slices together. Figure 10.3 shows a stack of 5 slices, which were put together in such way to build a 3D image of yeast cells. This image was obtained using a program developed and written by Adam Muschielok.

10.4 Microscope Setup

The experiments were conducted on a commercial spinning disc confocal microscope (SDM) from Andor technology. Due to its excellent speed and the resulting z-stacking capability it is an excellent tool to investigate the question of how the particles are formed and transported. The system is controlled by an externally mounted rack and builds together with the microscope, the scanning head and the detector so-called Revolution system accommodates three excitation lasers for three different wavelengths. These are

1. a 50mW Coherent Sapphire diode laser at 488nm
2. a 50mW Cobolt Jive diode pumped solid state laser at 561nm and
3. a 50mW Coherent Cube diode laser at 635nm.

The lasers are combined and selectively chosen by an *Acousto Optical Tunable Filter* (AOTF) from AA Opto-Electronic before being coupled into a multi-mode fibre. The exit of the fibre is fed into the Spinning Disc Unit (CSU10) from Yokogawa mounted on the sideport of a Nikon TE2000E microscope base. The beam is guided through various optics before illuminating the fast rotating Nipkow discs, the first disc with about 20.000 spirally arranged microlenses and the second disc with the corresponding pinhole array. After passing through the spinning disc unit, the beam enters the microscope and

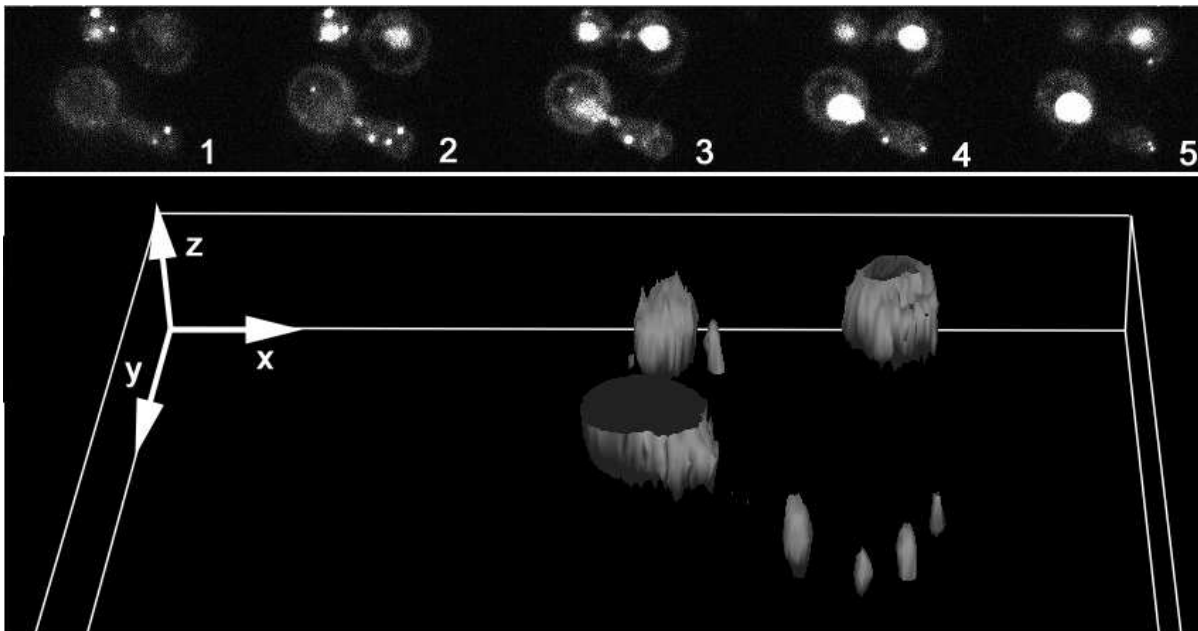


Figure 10.3: An image stack obtained with a SDM of labelled mRNA in yeast and the calculated three-dimensional reconstruction. (Courtesy of Adam Muschielok)

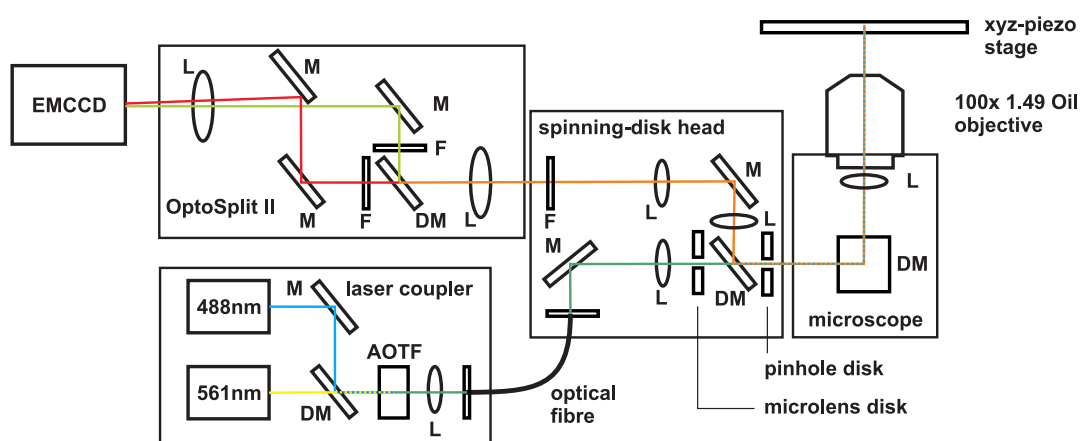


Figure 10.4: A schematic of the SDM. Laser light coming from the coupler enters the spinning disc head and is further transferred to the microscope. The back-detected fluorescence passes the spinning disc head and is guided to the OptoSplit. The spectrally separated signal is then imaged on the EMCCD.

can finally illuminate the sample. The sample is placed on a piezo-stage (NanoScanZ) from Prior Scientific enabling z-stack experiments. That stage is controlled electronically and is synchronised with the image acquisition via the Andor iQ software. In addition to the z-stage, the microscope is further equipped with a motorised xy stage, also from Prior Scientific. The microscope base has the possibility to illuminate with *Difference Interference Contrast* (DIC). A 100x Nikon (NA=1.49) oil immersion TIRF objective with a correction collar is used for both heated and room temperature measurements. The fluorescence emission is transferred back to the spinning disc unit, where it is spectrally separated from the excitation lasers by a quadrupel dichroic mirror (Di01-T405/488/568/647, Semrock) after the first Nipkow disc. A cleanup filter (NF01-405/488/561/635), also from Semrock, further blocks possible stray-light from the laser lines behind the spinning disc unit. Thereafter, the OptoSplit II filter cube unit from Cairn Research Ltd. separates the emission spectra on two different parts on the iXon+ EMCCD camera from Andor Technology. A setup scheme is shown in figure 10.4.

10.5 Data Acquisition

The Andor IQ 1.7 software was used to acquire the data and to control the peripheral devices. First, the program has to be configured to include all necessary parts which have to be controlled by the software during acquisition. These are the CSU10 spinning disc head, the EMCCD camera, the AOTF for the selection of the lasers and the piezo-stages to move the sample to the desired position. Then, the properties for the

experiments, such as laser lines, camera settings and image stack sequences, have to be set. After placing a sample into the focus, the experiment was started. An image consisting of 512x512 pixels with 16 bit gray value depth is 531.778 bytes in size. Taking 100 timepoints in five stacks for two excitation wavelengths, the size of the file sums up to 531 MB. This file has to be written to the harddisk without slowing down the acquisition itself. To ensure a reliable time sequence without interruption the harddisk is chosen and configured to act as a raid5 disk. This ensured a rapid image writing time and allowed framerates as fast as 25Hz limited by the read-out time of the CCD.

CHAPTER 11

Experiment:

mRNA Tracking in *Saccharomyces Cerevisiae*

In budding yeast, more than 20 different mRNA types are known to be localised to the daughter cell via the microfilament scaffolding of the cell [51]. In order to understand the machinery of mRNA localisation, it is necessary to not only conduct *in vitro* measurements but moreover to utilise methods which dynamically show the build-up and transport process *in vivo*. *In vivo* experiments may reveal undiscovered processes invisible to static snapshots of a highly dynamic system. With the development of high sensitive microscopes, it is now possible to observe processes of systems that have been only minimally altered.

11.1 mRNA

ASH1 is one of the many mRNAs, which are localised in the bud. There it is translated locally into the protein *ASH1p*, which is known to act as an inhibitor of the homothallic switching endonuclease which is responsible for mating type switching. For the transport of the mRNA, the cis-acting RNA sequences of *ASH1* are recognised by the *SHE2* protein [55]. *SHE2p* itself forms a dimer and binds to the mRNA inside the nucleus, presumably in the nucleolus. This complex can further bind to the myosin motorprotein *MYO4p* through the adaptor protein *SHE3p*. The myosin then carries *ASH1* to the daughter cell where the protein complex falls off the mRNA so that it can be translated by a ribosome. *MYO4p* is also known to carry *IST2* to the bud tip via the same *SHE*-protein complex. *IST2* functions as a membrane protein and is thought to be involved in osmotolerance, the cell's ability to withstand osmotic pressure. Also in this group of *SHE*-complex mediated transport of mRNA is *WSC2*, a sensor-transducer involved in the maintenance of the cell wall integrity and heat shock recovery. These three examples of *SHE*-protein complex mediated transport are used in this study to investigate the mechanisms behind mRNA localisation. In observing the properties of each mRNA, the question of how the

localisation process is conducted can be revealed.

For comparison, we have investigated the dynamics of *HOM2*. This mRNA does not localise to the bud but stays within the mother cell. *HOM2* is a precursor to methionine (Met) and threonine (Thr), two of the essential α -amino acids. *HOM2* acts as a negative control, since it does naturally not localise to the bud. An experiment conducted with *HOM2* can reveal possible artefacts connected with the labelling assay of the mRNA.

11.2 Tagging

Most commonly, the transport of mRNA can be studied with fluorescence labelling of the moving particle. For *in vivo* observation, the use of artificial dyes is complicated since the dye has to cross the cellular membrane. This constitutes a classical problem in cell biology, how to shuttle a fluorescent marker into the cell. Microinjection is a strenuous procedure for the cells, especially for yeast cells which are much smaller in size than mammalian cells. Cellular uptake, for example via endocytosis, does not give high labelling efficiency since the uptake usually can not be done specifically and, at the same time, the cell has effective methods to prevent the intrusion of foreign material. Cloning assays are therefore the most convenient way to specifically label particles inside the cell *in vivo*. Proteins which are fluorescent by themselves were extracted and are now accessible to biochemistry assays. They can be genetically fused to a genetic sequence which can be translated by the cell itself. The emerging construct then contains the protein together with the fused fluorophore. The obstacle for this kind of experiment is that the particle to be observed is not a protein but an mRNA, hence the fusion protein sequence is not transcribed yet and thus is not fluorescent. Therefore, another strategy to label the mRNA had to be developed. The mRNA has to be tagged in such way that a fluorescent fusion protein recognises the tag and binds to that part, thus labelling the mRNA. This has already been achieved with the MS2 system, a protein from the bacteriophage ϕ A. With MS2 tagged mRNA, Bertrand et al studied the transport of mRNA [5]. The MS2 is cloned to the mRNA and forms DNA hairpin loops which can be recognised by a second construct expressing the MS2 coat protein (MS2cp). The MS2cp is fused to a correctly folded fluorescent protein and thus the mRNA is labelled with that protein. Susanne Lange from the Ralf Jansen lab established a second construct which can label a second mRNA simultaneously. Another bacteriophage system, the λ -phage, exhibits similar binding possibilities. For this purpose, the mRNA was fused with boxB loops which are recognised by the λ -N-peptide (λ -pep). The fluorescent protein was attached to the λ -pep and thus a second labelling construct could be utilised to simultaneously label two different mRNA's. In this work, EGFP and RedStar RFP were used as fluorescent proteins. This system can therefore answer the question whether different mRNA are packed into common or different RNP carriers.

11.3 Cloning

The yeast cells have to be transmutated in order to label the mRNA. Resistance-(R) plasmids, which contain a resistance gene, are cloned with the sequence of the transmutation. The carrier, a herring or salmon sperm, includes the plasmids which can then infiltrate the cell. To favour the uptake of the carrier, the cellular membrane is permeabilised with lithium acetate at 45°C for half an hour. The leucin deficient medium constitutes a fatal environment for non-transmutated cells. The plasmid is composed of the gene for the deficient medium (leu) with an *Origin of Replication* (ORI). Here, the replication rate can be encoded, through "2 μ " for as many as 30-50 replications, CEN (centromer), for 1-3 replications or integrative, where the genomic sequence is incised into the DNA, which lead to a much lesser rate. Furthermore, the plasmid includes the promoter, with the binding site loops for readout, the *Open Reading Frame* (ORF) with the gene of the recombinant DNA, which the cell is supposed to replicate, and the terminator. The final result shows only transmutated cells with the new recombinant DNA, which could survive the fatal environment of the leucin deficient medium.

11.4 Image Analysis

For further image analysis, the available image data on the harddisk was saved as stacked tiff files and transferred to the analysis computer. The images were prepared using the freeware program *ImageJ*, version 1.38x [45], under *Java* 1.6.0.02. Four different spectral channels could be extracted from the image sequence:

1. GFP channel after excitation with 488nm
2. RFP channel after excitation with 561nm
3. RFP channel after excitation with 488nm
4. GFP channel after excitation with 561nm

However, for most cases, only the first two channels were used for the analysis. These were extracted according to the following procedure. First, the colour separation was made by de-interleaving the complete stack. As two excitation wavelengths were applied, the even frames belonged to one excitation wavelength and the odd frames to the other. Since the images of the two spectra are imaged on two spatially separated image areas on the CCD, the de-interleaved part was cut and thereby split resulting in two independent image stacks for each fluorescence signal. The essential information was taken from case '1', which will be denoted as the 'green' channel, and case '2', from now on denoted as the 'red' channel. However case '3' contained information about the spectral crosstalk and was sometimes taken into consideration as an additional information source. Case '4'

shouldn't contain any signal at all. The images themselves do not need further filtering or enhancements other than adjusting the contrast and the brightness. The signal from the fluorescent particles was clearly distinguishable from the background signal. The intensities of the two image stacks were adjusted and converted from a 16 bit to an eight bit grayscale image. This conversion was required for the colour merge of both channels. Usually, the green channel was shifted to overlap with the red. The *TransformJ* Tjshift plugin allowed a pixelwise shift of the image in x and y. The borders were filled with the appropriate value. The result was an RGB image stack where individual images could be extracted. For some measurements this RGB image stack was further converted to an *image5D* stack, a convenient file form for looking through different z-slices, colours and timepoints.

The tracking was either done manually or with the additional help of the *View5D* plugin for ImageJ written by Rainer Heintzmann. With this tool the user can select a particle of interest after which the plugin automatically looks in the next timeframes for the corresponding particle. It hereby applies a 2D gaussian fit at the vicinity of the particle's prior position to determine the next. The method becomes inaccurate when other bright signals interfere with the observed particle. In our case, a bright nucleus packed with fluorophores in the vicinity of the small RNP would disrupt the tracking manual tracking was required. For visualisation purposes, the result was converted with Matlab into coordinates from which the slices with the particle in focus could be extracted out from the stacked tiff file could be extracted. The resulting movie was a timetrace of the tracked particle always in focus. As the timepoints between two subsequent frames were not equidistant in time, the actual time had to be determined. The report file generated by the Andor software was so inaccurate that an additional program was written in Matlab to read out the timepoint from each tiff file to address this problem. They were otherwise only visible with the imageviewer of the IQ software. The tiff file format includes tags which Andor used to include the timestamps. The tag is encoded in the stack where a custom made program parsed through the file to find and decode the timestamp. They were situated at the beginning of each frame of the stack. The obtained timestamps were then included into the stack by overlaying time information with the image with a another custom-made program.

To calibrate the images, a reference image of a pattern of known dimensions was taken with the same setup. The pattern of the 1951 USAF Resolution Test Chart consists of three vertical and three horizontal bars with an identifier for the group and item imprinted next to it. The size of the bars can be calculated according the following formula: the length: $\frac{2.5mm}{2^{Group+(Item-1)/6}}$ and the width: $1mm \cdot (2^{-(Group+1+((Item-1)/6))})$. The scale was determined to be 7.580pixels per μm .

With the time and scale extracted from the images the stack could be processed into an avi movie.

CHAPTER 12

Results

12.1 mRNA Tagging with MS2 and boxB

In recent papers, tagging of *ASH1* and *IST2* with MS2 complex was shown by Edouard Bertrand, Pascal Chartrand, Matthias Schaefer [5], and Peter A. Takizawa and Ronald D. Vale [55]. Building MS2 hairpin structures were incorporated into the sequence of the mRNA. The MS2 coat protein (CP) which recognise the hairpins on the mRNA structure was fused with a fluorescent protein and thus labelling the mRNA itself with either a GFP, RFP or any other fusion protein. This technique allowed the observation of tagged particles *in vivo* in contrast to *Fluorescence In-Situ Hybridisation* (FISH), where cells have to be fixed and thus are no longer living anymore. With this tagging method, the transport of mRNA's can be observed. For the experiments presented in this part, the technique was incorporated to fluorescently label single mRNA's.

Cell lines with 6 MS2 loops in the 3' *Untranslated Region* (UTR) and a number of combinations of mRNA and fluorescent proteins alike were cloned and established in the Jansen lab. Table 12.1 gives an overview of the cloned constructs. As can be seen in the table, it was possible to clone the *IST2*-MS2 and the *ASH1*-MS2 constructs on terminator 3' UTR. The cloning of the new construct, *HOM2*-MS2, was also successfully performed in the Jansen Lab. However, as the goal was to measure whether different mRNAs are co-transported, a second tag is needed. A second tagging assay was established in the Jansen lab. The λ -boxB tag has its origin in the bacteriophage λ . The boxB-loops form hairpins, like MS2, which are recognised by the λ -peptide (pep). The boxB loops could be inserted into the mRNA sequence whereas a fluorescent protein was fused to the λ -pep. This gives the second labelled construct which can be utilised simultaneously with the MS2 construct for dual-particle measurements. Further analysis of the data showed that the boxB construct with 12 to 18 loops had to be placed at the 5' UTR, 36 basepairs upstream of the of the mRNA *Open Reading Frame* (ORF), the region where the RNA is encoded in a gene starting with the AUG codon. The reason for the upstream labelling position is that the λ -pep usually recognising the boxB loops,

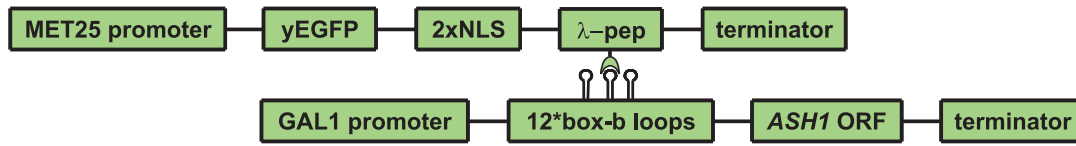
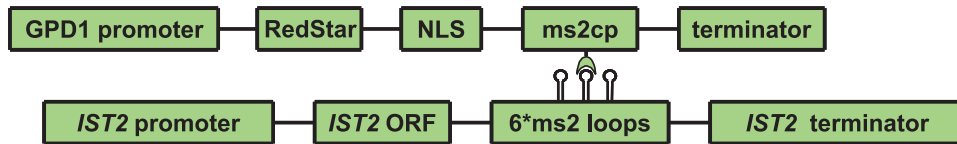
Table 12.1: mRNA constructs with MS2

No	mRNA	Prom	Binding Protein	Prom
3124	-	-	-	-
3134	<i>IST2</i> 6xMS2	<i>IST2</i>	RedStar-RFP-NLS-MS2cp	GPD1
3207	-	-	GFP-NLS-MS2cp	GPD1
3208	<i>IST2</i> 6xMS2	<i>IST2</i>	-	-
3209	-	-	-	-
3267	<i>IST2MUT</i> 6xMS2	<i>IST2</i>	RedStar-RFP-NLS-MS2cp	GPD1
3296	<i>IST2MUT</i> 6xMS2	<i>IST2</i>	GFP-MS2cp	MET25
3350	<i>IST2</i> 6xMS2	<i>IST2</i>	GFP-MS2cp	MET25
3351	<i>ASH1</i> 6xMS2	GAL1	GFP-MS2cp	MET25
3390	6xMS2 <i>HOM2</i>	GALS	GFP-NLS-MS2cp	GPD1
3393	-	-	-	-

failed binding to these sites if the loops were put on the 3' UTR, possibly because of steric hindrance. Further studies revealed that higher numbers of boxB loops resulted in an increase in unspecific binding to motor proteins. The constructs used were therefore made with either 6 or 12 loops. Table 12.2 gives an overview of the cloned constructs with the λ -pep tag. Figure 12.1 and figure 12.2 show an exemplary sequence of either *ASH1* mRNA with the λ -pep tag or *IST2* mRNA with the MS2 tag. The tags are bound to the hairpin structure which was cloned into plasmid for the mRNA sequence.

Table 12.2: mRNA constructs with λ -pep

No	mRNA	Prom	Binding Protein	Prom
3124	12xboxB <i>ASH1</i>	GALS	GFP-NLS- λ	MET25
3134	12xboxB <i>ASH1</i>	GALS	GFP-NLS- λ	MET25
3207	12xboxB <i>ASH1</i>	GALS	-	-
3208	-	GALS	GFP-NLS- λ	MET25
3209	-	GALS	GFP-NLS- λ	MET25
3267	12xboxB <i>ASH1</i>	GALS	GFP-NLS- λ	MET25
3296	12xboxB <i>ASH1</i>	GALS	RedStar-RFP-NLS- λ	MET25
3350	6xboxB <i>WSC2</i>	GALS	RedStar-RFP-NLS- λ	MET25
3351	6xboxB <i>WSC2</i>	GALS	RedStar-RFP-NLS- λ	MET25
3390	12xboxB <i>ASH1</i>	GALS	RedStar-RFP-NLS- λ	MET25
3393	12xboxB <i>ASH1</i>	IST2	GFP-NLS- λ	MET25

Figure 12.1: *ASH1* Sequence with Tag ConstructFigure 12.2: *IST2* Sequence with Tag Construct

A *Nuclear Localisation Signal* (NLS) was included to confine non-bound GFP particles to the cell nucleus, which greatly enhanced the contrast of particles travelling in the cytosol. The remaining GFP particles were visible as a bright signal in the cell nucleus (Figure 12.3).

The methionine25 promoter reacts on methionine demands. When a low concentration of methionine is present, the methionine promoter is activated and the following sequence translated. In contrast, the galactose1 promoter is activated when galactose is abundant in the medium. After induction with different promoters either Met25, Gal1 or the endogenous *IST2* promoter, we observed the formation of particles within 30 minutes after induction. Furthermore, it was observed that a number of particles formed at early stages which later fused to larger complexes. From the structure of *SHE2* and the loops many *SHEps* were binding to the loops. As *SHE* is a dimer, an aggregation is likely to happen.

To prove the binding specificity of MS2cp to the MS2-loops and the λ -pep to the boxB loops numerous cross experiments were conducted which showed no creation of RNP particles for boxB with MS2cp and MS2 with λ -pep. Hence the binding is specific only for the corresponding binding partners MS2cp with the MS2-loops and λ -pep with the boxB loops. Thus this tagging system is valid for using for the two colour measurements.

12.2 Localisation

The experiments showed the expected localisation of *ASH1*, *IST2* and *WSC2* to the bud. Other particles which were located in the cytosol in the mother cell were either immobile, representing a fraction of either damaged mRNA or individual GFP or RFP particles respectively, or were transported to the bud at a later transport. The tagging system also worked for the *HOM2* particle, which did not localise, as expected for the negative control and was indeed found exclusively in the mother cell.

Additional tests were made to ensure a proper tagging system. *IST2* mRNA, where the known localising sequence was deleted and replaced by a UUU point mutation, was occasionally observed to become localised. As the outcome was also seen in FISH measurements it appears that *IST2* has more localisation signals than those known and deleted. A similar observation was made with *ASH1*, where the localisation sequence was deleted. Also here, *ASH1* was seen to localise to the bud tip. However, in this case, it is presumably because the *SHEp* complex seems to bind to the boxB loops. Another possibility for this observation is that *ASH1* and *IST2* has more localisation signals than previously known. Although the deletion of the localisation did not agree perfectly with the suggested model, the unexpected localisation can be explained with unknown localisation sequences. However, since the rate decreased and also the major proof of naturally unlocalising mRNA showed the expected occurrence restricted to the mothers's cytosol, the localisation of mRNA could be shown.

Table 12.3: Results

No	Outcome
3124	-
3134	3D tracking
3207	no interaction
3208	no interaction
3209	no particles
3267	unspecific DsRed particles, no conclusion
3296	MS2 CP w/o NLS
3350	control for colocalisation of two localising mRNAs
3351	same as 3350, but with new pair, <i>ASH1</i> here as MS2 fusion
3390	control, localising vs. unlocalising

12.3 Colocalisation

Previously colocalisation experiments of mRNA were conducted on fixed cells based on FISH [14]. These studies lack the possibility to clearly distinguish between random and real colocalisation. Due to the property of the localising mRNA to be anchored, preferentially at the bud tip, colocalisation can appear by chance. The occurrence of overlapping signals is only dependent on the particle density. Only extensive studies gaining a statistical insight of the processes can eventually reveal a real colocalisation. There is still the controversial question of FISH actively influencing the system leading to falsified results. However, these experiments show the first results of live cell imaging in three dimensions. In this study, those mRNA particles forming RNPs could be observed over a defined time period to move in unison for differently labelled mRNAs. This time-lapse

observation support the surmise of colocalising particles. The movement of particles of both types could be followed individually with the SDM. The experiment showed that different localising mRNAs are using the same carrier rather than taking different ones. The RNPs were then co-transported to the bud, verifying that the localisation utilises a general transport mechanism. There was no occurrence of two independently moving RNPs.

To verify that the signal is not due to aggregation induced by overexpression but a real physiological result, the *ASH1* and *IST2* were translated using their endogenous promoter. Also *ASH1* was tested with a short induction pulse to see whether overexpression would affect the result. Particles formed already 15 minutes after induction, indicating that the signal is a real physiological result. A gal promoter, which is too strong, would lead to or provoke coalescence of particles. With the endogenous promoter, particles were observed showing the expected colocalisation. Although this clearly confirms our previous measurements, the endogenous signal was too dim to last long enough to extract particle trajectories.

12.4 mRNA Transport

Not only was the colocalisation of different mRNA studied but also the complete movement of the RNP from the mother to the bud was observed using time-lapse measurements with the SDM. The analysis of the particle position was either done manually or with the help of the View5D plugin from ImageJ. With the View5D plugin the focus was set on one of the particle of interest and the program calculated the next particle position in the stack of images by finding the closest intensity maximum obtained with a gaussian fit in all three dimensions. It was possible to manually interrupt the finding process to force the focus to a specific point which was especially needed in the case of multiple particles close to each other. The finally obtained trackdata was read by a custom-made Matlab program to further analyse and visualise the complete trajectory. Thus the colocalising mRNA transport tagged with MS2 and boxB constructs could be shown on living cells with the SDM setup. It was possible to determine the average speeds and moving behaviour of the particles themselves. The difference between active transport of the particle and occasions where the particle seemed to try to anchor to the bud tip could be distinguished. In figure 12.3 the top image represents the brightfield image with the fluorescence image overlay together with the 2D trajectory. The trajectory shows the path, the double labelled mRNA particle has travelled from the mother to the bud tip. In the lower part of the image, the three dimensional representation of the same trajectory show the examples of active transport (middle row) and corralled motion (bottom row) highlighted in blue together with the corresponding msd-plot. The present data is a big improvement of the tracking in 2D by Bertrand [5]. The advantage is the ability to visualise dynamics in more than just two but three dimensions.

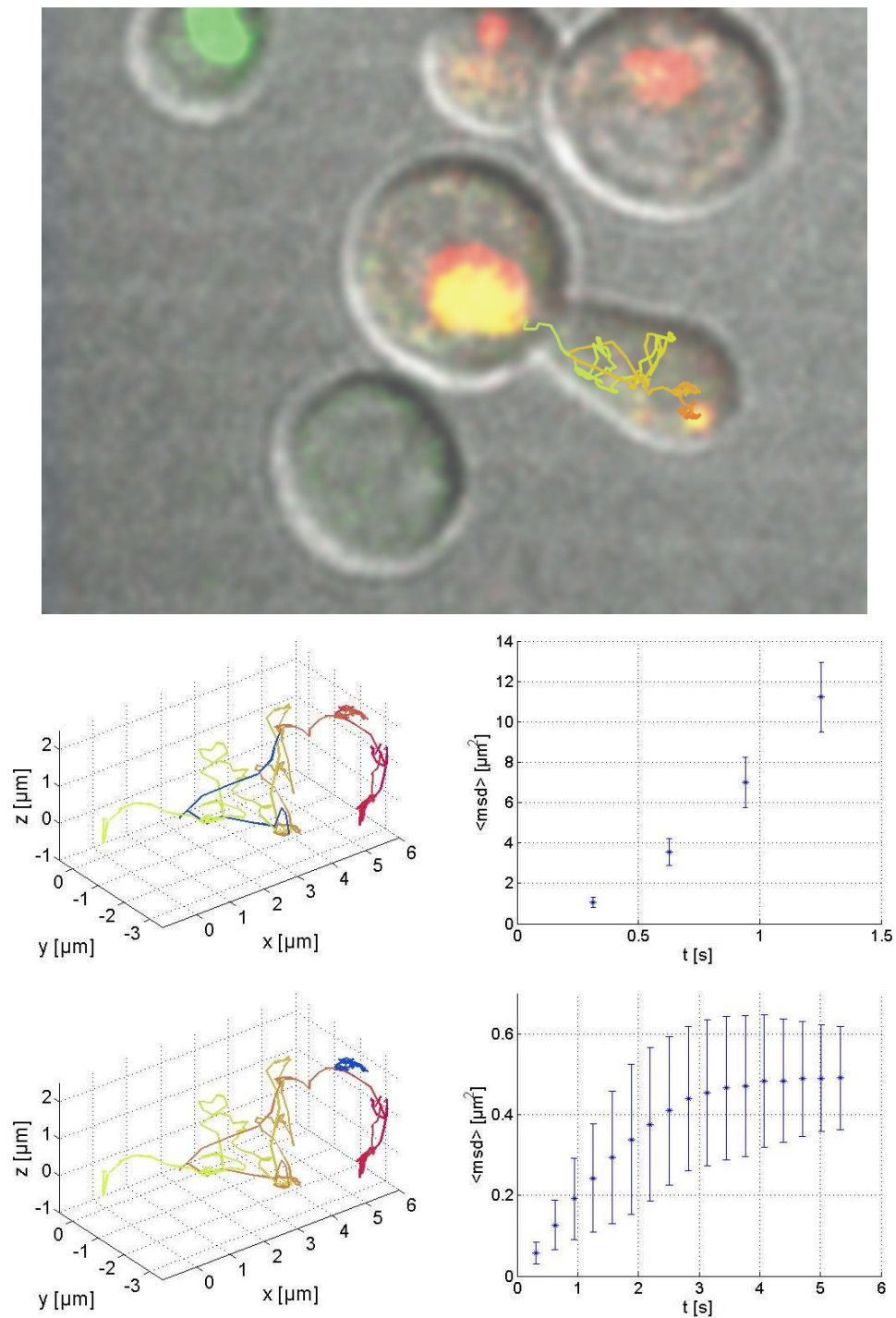


Figure 12.3: Trajectory showing the trace of labelled RNP on the way from the mother to the bud (top). Three dimensional trajectory of the same trajectory (lower). Colours indicate time advancement from green to red. Inserted blue colour regions indicate active transport (centre left) and corralled motion (bottom left) with their corresponding msd-plot (right).

12.5 The Influence of Unmatured RedStar RFP

In addition to the spectral crosstalk of GFP into the red channel and direct excitation of RFP which are solved by msALEX with 488nm light another problem can evolve from unmaturing fusion proteins. In this experiment RedStar RFP, a mutant of RFP and improved version DsRed, was used for the colocalisation experiments. However, on several occasions it was observed that signals of RFP leaked into the green channel. After testing the filters again it was obvious that the choice of the filter was not the reason for the spectral crosstalk.

Andrea Sacchetti et al showed that unmaturing RFP forms a dimer which emits light in the same spectral region as GFP [47]. It was found that the leakage into the green channel was caused by RFP in its unmaturing form. As is apparently the case, unmaturing RFP signals interfere with common GFP signals. This is a possible cause for falsified results during colocalisations experiments. Through the usually different bleaching rates, it was possible to determine the composition of the green signals in most measurements. An example of distinguishing GFP and RFP through the bleaching rate is shown in figure 12.4. The figure shows a set of images taken at two different timepoints. The upper row taken at an earlier stage shows the green channel after excitation with 488nm. A particle is clearly visible in the bud. However a tremendous amount of RFP signal is clearly visible in the red channel. Not only is this a signal resulting from spectral crosstalk but from also RFP excited with 488nm. The true signal of RFP is shown in the right most image where the red channel after excitation with 561nm is shown. The green channel with 561nm excitation is black as expected. The problem arises when RFP signal is so strong that it is impossible to tell the origin of the green signal and whether it is a result of GFP or unmaturing RFP. Only in the row below which is the same system after some observation time gives a clear idea of the origins. It can be seen that GFP has almost the same intensity as before whereas the RFP signal is significantly bleached. As the green signal did not faint it cannot be due to unmaturing RFP.

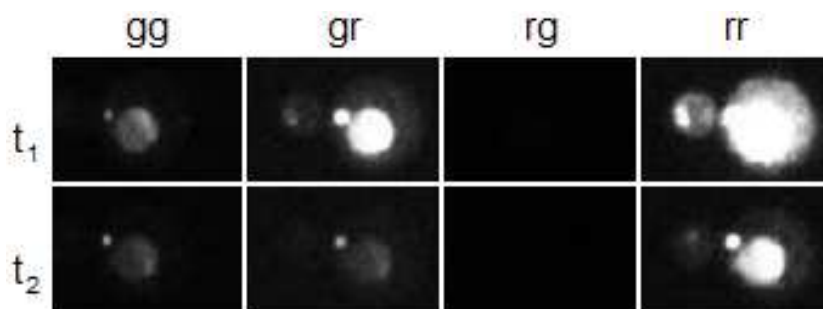


Figure 12.4: Crosstalk; rows: represent two different timepoints; columns: left letter detection, right letter excitation.

CHAPTER 13

Summary and Outlook

In this part, we have shown that different mRNA particles use the same transport machinery to become localised to the yeast bud. As expected from previous studies, the RNP complexes utilise a common transport machinery which carries the load via myosins to the bud tip of the yeast. Two different tagging systems have been established for these experiments, which allowed the simultaneous observation of two mRNA species. With several test measurements, we determined that there is no influence of the tagging procedure nor the expression rate on the localising behaviour. Localising mRNAs were moving to the bud while non-localising mRNA species remained in the mother cell. The SDM allowed rapid acquisition of z-stacks which were then analysed with both commercial and custom software. The co-transport of different mRNA species may represent a common procedure in which corresponding particles are travelling in the same RNP complexes.

The observation of RNPs travelling side-by-side suggests that the coordinate life-cycle of mRNA localisation might also come along with the co-transport of the translational machinery. Two recent studies have shown that localising RNPs can associate with the tip of the tubular *endoplasmic reticulum* (ER) structure which are covered with ribosomes [1][50]. In the near future, a labelling of the ER structure will allow us to answer this question. A further interesting aspect is the anchoring of the RNP particle to the bud tip. In the movies obtained, the RNP particle moves to the furthest tip of the bud and shows cumulating phases of pausing. This suggests an anchoring attempt of the RNP to the tip. The later timepoints of RNP transport have to be investigated to see whether this anchoring attempt is true or otherwise disturbed by the structural reconfiguration of endogenous mRNA caused by the tagging system.

Part III

PICH Dynamics during Meta- and Anaphase

CHAPTER 14

Introduction to part III: PICH

During mitosis the cell divides into two identical daughter cells, each one of them provided with the identical set of genetic information. The division is a highly organised process where a perfectly balanced set of actions and checkpoints assure a proper division. The actual segregation of sister chromatids is a subtle set of mechanisms ensuring the correct progress of events leading to a successful division. A failure of proper separation can lead to cancer. The newly discovered protein *Plk1-Interacting Checkpoint Helicase* (PICH) is suspected to play an important role during these processes [3]. To support biochemical evidences, experiments were conducted on the spinning-disc confocal microscope (SDM) on live-cells. In collaboration with Lily Wang, a researcher from the group of Erich Nigg at the Max-Planck institute for Biochemistry, the role of PICH during meta- and anaphase has been studied *in vivo*.

CHAPTER 15

Theory: Chromosome Segregation

15.1 Mitosis

During proliferation each eucaryotic cell experiences a set of phases which describe the current state of the cell. This set is called the cell-cycle and consists of four distinct phases: G1, S, G2 and M phase. Three of the phases, G1, S and G2 are often summarised to the so-called interphase, as the cell's appearance does not change considerably. The interphase is surrounded by the M phase which is named after mitosis. This is when the cell division occurs after which the two resulting cells enter the cell-cycle beginning with the G1 phase. In the postmitotic G1 phase cytosolic constituents are being replicated and the cell prepares for the following DNA synthesis. In S phase the DNA is replicated or synthesised. At the end of S phase two sets of chromatids are within the nucleus. In G2 the cell prepares for cell division. G1 as well as G2 are called the gap phases as the cell appears unchanged for the untrained eye. In both G phases several checkpoints ensure the proper progression of the cell cycle. Any failure leads to a cell cycle arrest and in worst cases to an inevitable apoptosis, the programmed cell death. The mitosis or M phase is a comparably short period where the cell divides into two identical daughter cells. An equal number of chromosomes is distributed to the daughter cells. Since a tremendous number of processes happen, each one of them playing an vital role for the fate of the next cell, the coordination of the single steps during this sequences have to work perfectly. Any major mishap usually leads to apoptosis. Though the cell has developed numerous rescue mechanisms to ensure proper cell mitosis, and failures occur only occasionally. rescue mechanisms have been developed any major mishap usually leads to apoptosis. Furthermore, the mitosis itself can be subdivided into seven steps which can be distinguished by the form and arrangement of the DNA. During prophase the chromatin state of the DNA from the interphase begins to condensate into the chromosomes. It consists of two sister chromatids which are bound at the centromere. In the next step the prometaphase the nuclear envelope disassembles. Two poles, the centrosomes, build up at opposing sites of the cell from which the microtubular spindle

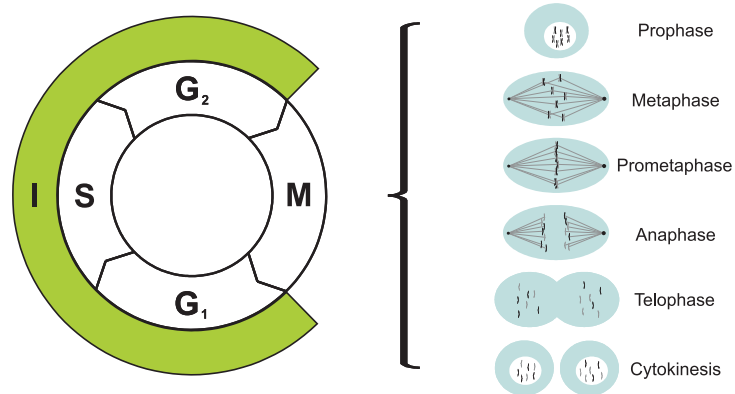


Figure 15.1: The cell cycle with a detailed description of the different processes within mitosis.

apparatus forms. One end of the spindle attaches to the centrosomes, also called the spindle pole, the other to the kinetochore which build up at the centromeres of the chromatids. In metaphase the chromosomes align in the centre of the cell resulting from the forces the spindle apparatus forms. After proper alignment the spindles pull each set of chromatids to each end of the cell during anaphase. Then during telophase when all chromosomes have successfully reached their final position close to either end of the cell a new nuclear envelope builds up and the chromosomes unfold back to chromatin structure. Finally the cleavage furrow builds up and separates the two cells during cytokinesis. The cell cycle is summarised in figure 15.1.

15.2 Cohesin and DNA Catenation

This study focusses on cells from metaphase to anaphase. During metaphase, the chromosomes align at the centre of the cell before the spindle system pulls the chromosomes to each sides of the cell. The process of proper chromosome segregation is maintained by two mechanisms which are known to hold the chromosomes together prior segregation:

1. Cohesin Protein Complex Formation and
2. DNA catenation

The *cohesin* is suggested to form a ring which is wrapped around the two sister chromatids to prevent premature separation. Cohesin is then disassembled by Wapl and Plk1 and AuroraB during Metaphase. Only cohesin complexes at the centromere remain protected by the action of shugoshin (SGO) together with the phosphatase 2A (PP2A), until during anaphase the spindle assembly checkpoint (SAC) is silenced. The SAC ensures the bipolar attachment of the microtubules to the spindle and the proper

tension between all sister chromatids. Separase becomes activated and cleaves the centromere cohesin subunit hRad21/Sec1 so that the sister chromatids can separate. An antagonist, securin, is preventing the separase to work on cohesin. Only during anaphase the securin is hydrolysed and finally separase can act on cohesin.

During replication the DNA is entangled with the sister chromatid which leads to the effect of *DNA catenation*. This embracing has to be unwound. The unwinding process or decatenation is initiated by *Topoisomerase-II α* (TOPOII) which helps the DNA to change its topology by inducing double-strand breaks, restructuring and fusing the breaks again [56]. The decatenation process starts already in G2 phase until Mitosis. The chromosomes disentangle beginning from the arms and continues to the centromeric region of the chromosome. This then results in the typical X shaped DNA structure. It was suggested that decatenation ends with the sister chromatid separation. However the processes involved in the decatenation process is not well understood and the results indicate that decatenation lasts as long as to late anaphase. TOPOII required for decatenation was needed even after the onset of anaphase to completely decatenate the sister chromatids. It is found that *Polokinase1-interacting checkpoint ATPase* (PICH) binds to catenated centromere DNA in anaphase and could therefore play an important role in the decatenation process in combination with TOPOII.

15.3 PICH

PICH acts as an interaction partner and substrate of *polo-like kinase 1* (Plk1). Plk1 itself is an important regulator in mitosis and is needed for centrosome maturing, the formation of the spindle apparatus, the chromosome segregation and the cell division itself. Plk1 is also recruited to sites at which PICH becomes phosphorylated and controls its localisation. PICH then accumulates at kinetochores and inner centromeres in prometaphase. Since it binds to catenated centromere DNA during anaphase the question arose how the TOPOII-mediated DNA decatenation is influenced by the act of PICH. The binding to threadlike DNA structure connecting sister chromatid centromeres could so far be shown *in vitro*. The dynamics of the thread resolution was yet unknown and will be first revealed in this study.

CHAPTER 16

Experiment: PICH Dynamics in Metaphase

16.1 Setup

The experimental setup is based on the spinning-disc microscope (SDM) which was described in section 10.4. Also here the sensitivity of the system proves to be a suitable tool to reveal the dynamics of PICH *in vivo*. The dyes used in these experiments are EGFP, YFP and mCherry. Since the EGFP signal is strong and mCherry did not show a significant signal in the green channel, the set of filters in the filtercube separating the fluorescence emission of the two dyes were changed to suit the new experimental properties. Instead of a narrow filter used in part II for the mRNA tracking, the green channel is equipped with a broader filter (hq525/50, Chroma). This enabled the observation of YFP with the same filter which was used instead of EGFP in some experiments. The structures observed had however a clearly distinguishable appearance so that possible spectral crosstalk could be recognised immediately. Furthermore to provide an ideal environment for the cell suspension over several hours, the sample was heated to 37°C with a stage heater (TC-500, 20-20 Technology) together with an objective heater (Tempcontrol mini, Pecon).

16.2 Cell Biology

As discussed in section 15.1 mitosis is a very short interval during cell cycle. Therefore not many cells can be seen in mitosis in a normal cell suspension. With biochemical assays though it is possible to arrest cells in a certain stage during cell cycle and release them in a controlled manner prior the experiment. In doing so a huge number of cells can be stimulated to enter into mitosis simultaneously. For the observation of anaphase cells this procedure turns out to be extremely helpful since there is a greater number of observable anaphase cells.

16.2.1 Cell Preparation

GFP-histone H2B and YFP-CENPA competent stable cell lines were cultured in two-well chamber slides (NUNC) in 1ml/well normal medium (DMEM, 10% FCS, 1% penicillin and streptomycin). The cells were simultaneously transfected with mCherry-PICH and PICH-1 siRNA solution which is $3\mu\text{l}$ of Oligofectamine (Invitrogen) and $3\mu\text{l}$ of $20\mu\text{M}$ PICH-1 oligo in $100\mu\text{l}$ OPTM-1 medium (Invitrogen) for each well. Simultaneously the PICH transfection was made with $6\mu\text{l}$ Fugene 6 (Roche) and $2\mu\text{g}$ of DNA in $100\mu\text{l}$ OPTM-1 medium. 10h after transfection the cells were synchronised by exposing the cells to 100mM thymidine which arrests them in S-phase. After 18h they were released into mitosis and then arrested again by $100\mu\text{M}$ Noscipine, a microtubule interfering agent, for another 14 hours. Only after then the cells were released 30 minutes before the cells were investigated for the experiments under the microscope. Because PICH excess turned out to be toxic the imaging was performed on cells expressing low levels of mCherry-PICH.

16.3 Image Acquisiton

The images were acquired with the SDM. The acquisition time for each image was set to 50ms. Up to 23 planes with each slice separated $0.5\mu\text{m}$ from the next were observed in z. The high amount of planes was necessary because of the spatial distribution of anaphase chromosomes. Every now and then the cell was tilted that the structures observed, the interconnecting threads, were only visible complete by joining several image planes. Depending on the experiment an additional delay was given so that the total frametime was between 2s and 30s. The timepoints were chosen that the size of the data could be analysed without splitting the data file. About 200 timepoints were taken so that the total image stack size summed up to about 8000 images per experiment. If necessary the images were split immediately on the acquisition computer according to their excitation channel, either in green or in red before finally transferred to the analysing computer. The convenient image size was limited by the software ImageJ (<http://rsb.info.nih.gov/ij/>), which only allowed file size of below 1.5GB. If the files were larger they would have to be cut either by the Andor IQ 1.6 software or by custom made programs in Matlab 7.0 (Mathworks).

16.4 Analysis

From the stacked tiff files the colours were separated and the slices de-interleaved using ImageJ. The threads were elongated approximately along the image plane but as it did not perfectly match to one image slice several slices were combined resulting in an image which showed the complete threads. For this purpose a z-projection of five consecutive

image planes was made. The files were regrouped using Matlab 7.0. Thereafter five z-slices of $2.5\mu\text{m}$ thickness in total were projected using an average projection. A maximum projection came out to be less powerful to show the threads as it further enhanced the background signal unlike the relevant thread signal which became even less visible. Two different filters were then applied in order to enhance the quality of the images of the PICH dynamics. In a custom made program the raw data, the data processed with a gaussian blur filter and the data processed with a Kalman stack filter, all processed with ImageJ, were presented in parallel. The thread dynamics were extracted by means of a frame by frame analysis, that means that every single picture was analysed for PICH thread end-point positions. The consultation of three differently processed image stacks resulted from the fact that neither process was showing the best results for each image stack. Depending on the cell dynamics, PICH signals could appear clearer with Kalman filtering or gaussian filtering or the raw file itself. In general for longer timescales and dynamic cells the application of the gaussian filter was preferred. However for slower dynamics, i.e. less cellular rotation or wiggling and shorter timescales, the Kalman filter gave the most satisfying results.

16.4.1 Gaussian Blur Filter

The gaussian blur filter is applied on noisy images which show fluctuating pixels throughout the area interfering with the real image information. It smoothes or de-speckles the image by convolving the original image with a predefined kernel matrix of gaussian shape. The radius of the gaussian decay can be defined to where the value decreased to $\exp(-0.5) \sim 61\%$, that is the standard deviation of the gaussian distribution. The size of the kernel usually is kept to a size of about three standard deviations from the mean, where the values are effectively zero. That is a practical solution since the gaussian distribution never reaches zero and would lead to an infinite size of the matrix. It has to be considered, that like in many convolution operations, the pixels outside the image boundaries get the value of the nearest edge pixel, thus resulting in a higher weight of corner pixels and even higher for edge pixels. The higher the kernel size is, the more serious this boundary weighting comes to an effect. The outcome of the gaussian blur filter is an enhancement of structures about the size of the filter radius, while other structures become suppressed.

16.4.2 Kalman Stack Filter

The Kalman Stack filter is a temporal smoothing filter. It acts as a recursive prediction and correction algorithm [28]. The filter performs the following steps: Initialisation, correction, prediction, update and repeat from the correction step again. As it predicts future images from the information from the past the order of the stack was reversed to prevent artefacts in the dynamics of the thread separation. Now the timepoint of

a dissolving thread starts at the dissolving frame and does not become smoothed into earlier timepoints. When applied to an image the Kalman filter enhances the signal which lasts longer in time thus eliminating temporal fluctuations such as noise.

CHAPTER 17

Results

The involvement of PICH during the resolution of catenated centromeric DNA in anaphase has been visualised in live-cell imaging on the SDM. Although the binding to threadlike DNA structures connecting sister chromatid centromeres during metaphase until late anaphase was shown *in vitro* [3], the dynamics of the thread resolution was first revealed in this study.

17.1 Chromosome Separation

Labelled cells were observed under the SDM from prometaphase until cytokinesis. The typical cell in mitosis starting from prometaphase is shown in figure 17.1. The image sequence shows HeLa cells with EGFP labelled histones in green resulting in a labelling of the actual chromosome. Also in this picture PICH is labelled with mCherry and shown in red. Each image represents a projection of five subsequent slices of the image stack to ensure that a complete plane along the separation can be observed. The first six images are taken every five minutes. To resolve the faster dynamics of the separation the following ten images were two minutes apart from each other until the last images show again the five minutes gap between subsequent images.

The chromosomes are nicely aligned in prometaphase at the central region of the cell. It stays a while until the chromosomes are drawn to opposite sides of the cell by the spindle apparatus in anaphase. The red signal of PICH can be seen at the ends of the chromosomes in the direction of the centrosomes. This already indicates that PICH is associated with centromeres. Some visible red signals are left from the non-complete tagging of PICH itself. The segregation itself lasts about ten minutes, which is in agreement to existing observations. When the chromosomes are correctly segregated the cell starts to form a cleft in telophase where the future cell membranes build up. Meanwhile the chromosomes dissolve into chromatin fibres until faintly seen in red the new cell membrane forms the two new cells in cytokinesis.

The emphasis was put on the chromosome separation. Labelled histones, PICH associ-

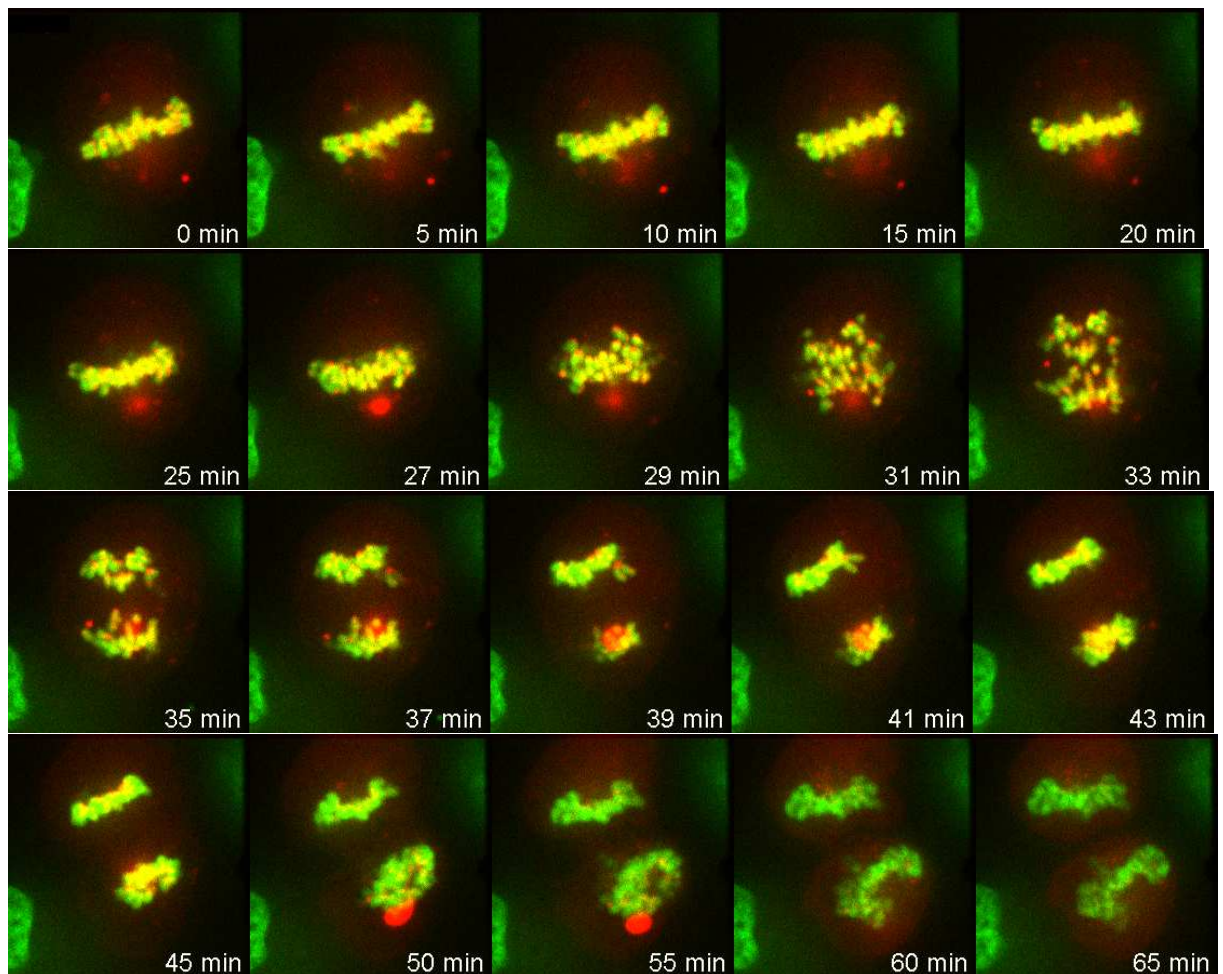


Figure 17.1: Chromosome segregation in HeLa cells in mitosis from prometaphase to cytokinesis observed for 65 minutes.

ated nucleotides and centromeres themselves were aligning in prometaphase. The actual startpoint of the separation, in other words the anaphase, was difficult to determine. The cell could stay in prometaphase for as long as an hour without entering anaphase. The continuous observation of those cells is unfavourable since the dye is subject to bleaching. In contrary, the beginning of anaphase could be missed one waited for the separation. To favour separation, cells were treated as described in the methods part to have an abundant number of mitotic cells to raise the chance of observing dividing cells. Then cells were selected for aligned chromosomes. Metaphase cells, which had lagging chromosomes, would have taken too much time until chromosome segregation. Since a strong signal often inhibited proliferation, cells with only an increased brightness compared to the rest were sought for.

An image sequence obtained with higher time resolution shows mCherry-PICH in red

together with GFP-H2B in green, marking histones in figure 17.2. Each image is an average projection of five subsequent slices and the complete stack was time reversed and filtered with the Kalman stack filter to enhance the PICH signal. PICH hereby seems to localise with centromeres and evolves faint threads aligning between the separating chromosomes. Those PICH associated threads have been anticipated by previous measurements but were firstly discovered here *in vivo*. Here a closer look on individual threads can be made which strengthens the speculated ripping thread. In this figure the thread appears to be under tension, since the rip forces the thread to snap back until a certain distance after which it appears to resolve slowly towards the centromeres. Therefore PICH may be suspected to bind to catenated centromeric DNA to monitor tension under chromosome separation.

17.2 PICH colocalises with centromere DNA

To determine to which part of the chromosomes PICH binds, live-cell imaging can verify the discoveries from biochemical assays. It was shown in biochemical studies that PICH binds to centromeric DNA [3]. In this study this result could be verified with live-cell imaging. Figure 17.3 shows mCherry-PICH labelled mitotic cells in anaphase in red together with YFP-CENPA centromeric protein marked in green. Clearly the centromere localisations are visible in yellow which is a clear agreement to the previous findings of PICH colocalising with centromeres. Furthermore the PICH signal can be seen in between two sister centromeres as faint threads already discussed in the prior part. The three images also show the different processing techniques which were also applied for the other measurements. The first image shows a projection of five image planes of the raw data with green and red channel overlain. The second is a projection, where the complete track was first reversed and then filtered with the Kalman stack filter, which is a smoothing filter in time. The third image was filtered with a gaussian resulting in a spatial smoothing of the image. Clearly all images show dots of the colocalising signal

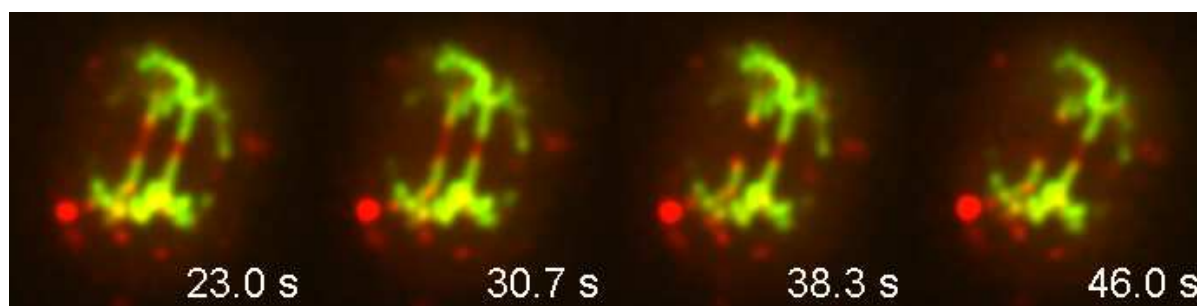


Figure 17.2: The ripping of an individual PICH thread can be observed. The thread appears to be under tension since the cut thread snaps back.

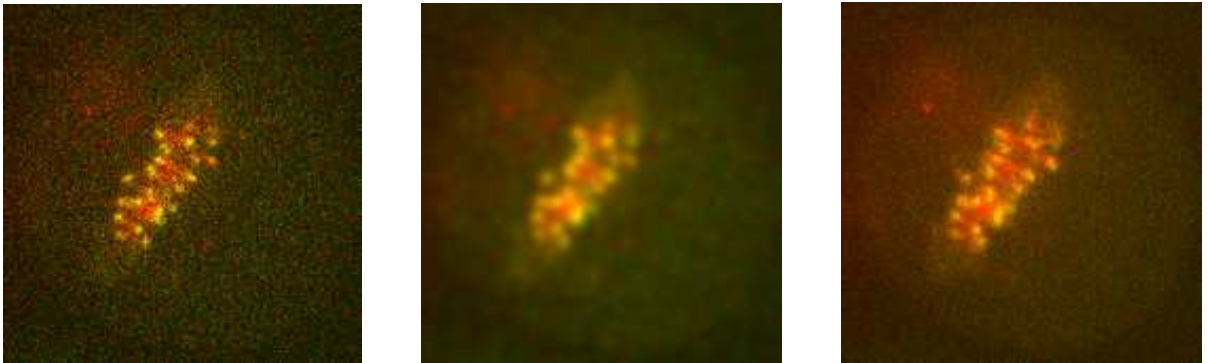


Figure 17.3: PICH-Centromer Colocalisation with raw data, Kalman processed and gauss filtered

and the threads themselves. The image quality is though dependent on the dynamic behaviour of the dividing cell. Especially for steady movements without oscillations of the signal the Kalman filtering shows better results. In undulating signals the Kalman filtering can show artefacts which appear as a faint tail in the image. The reversing of the stack order prevents a misinterpretation of the starting time of the ripping as the Kalman filter works only in forward direction of the stack. The efficiency of the gaussian filter depends on the structure size. For spot-like structures in the size of the gaussian filter the filtering shows very good results. However for unstructured signals such as the threads of labelled histones the gaussian filter turns out to be inferior to the Kalman filtering.

17.3 The dynamics of PICH associated threads

To show the dynamics of the ripping threads in anaphase, the images were analysed using a Matlab program. In this program, the image sequence was shown step by step with the possibility to switch between raw image, Kalman and gauss filtered. Then, the dissolving PICH threads and their anchoring point on the centromeres were marked manually to evaluate the dynamics of the ripping and recoiling threads. Figure 17.4 shows the results.

17.4 PICH in Walker A mutant deficient cells

Figure 17.5 shows an example of the separation of a Walker A mutant (K128A) cell, which has an ATPase deficient PICH mutant. Clearly it can be seen that the separation is prolonged and that some PICH labelled threads cannot resolve properly over the observed time period of almost 40 minutes. For this measurement the lag time between

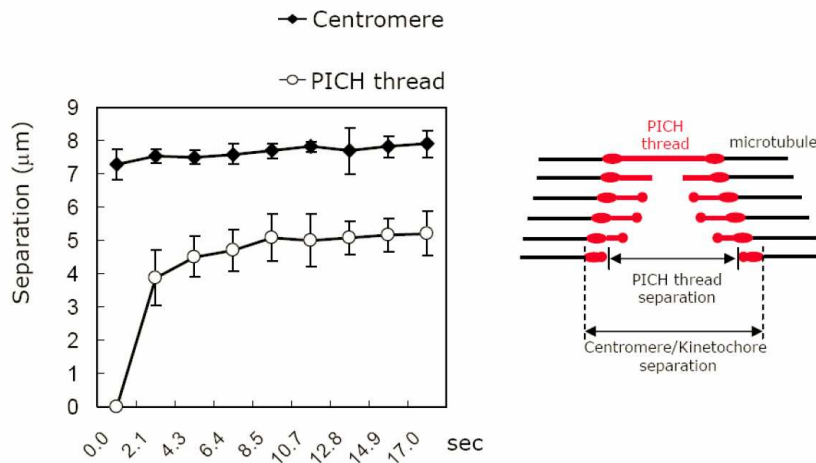


Figure 17.4: The dynamics of the threads (left panel) and a schematic of the suggested process (right panel).

two subsequent images had to be prolonged such that the faint signals did not bleach before the end of the acquisition. From the prolongation it can be inferred that ATPase activity of PICH is required for efficient decatenation of the DNA.

17.5 Supplementary biochemical results

With additional biochemical assays it could be shown, that cohesin removal is a prerequisite for TOPOII-mediated decatenation. The complete resolution of the sister chromatids can be seen as follows: first the ringlike cohesin structures connecting sister chromatids are removed from chromosomes with the help of Wapl, Plk1 and Aurora B in the prophase pathway. Only centromere associated cohesins are left and protected by shugoshin1 (Sgo1) and protein phosphatase 2A (PP2A). These centromeric cohesin complexes were dissociating after the spindle assembly checkpoint (SAC) is silenced. Securin is degraded and hereby separase becomes activated which then cleaves the remaining cohesins which triggers anaphase. Simultaneously with TOPOII and PICH catenation as a direct consequence of DNA replication is resolved. Also here decatenation is first carried out at the arms of the chromosomes so that the typical x-shaped morphology can be seen in metaphase. However only in anaphase the centromere associated catenated DNA is resolved [3]. Since PICH persists on ultrathin DNA threads until anaphase PICH seems to promote TOPOII activity. Furthermore with biochemical assays it could be shown that a prerequisite of decatenation is the removal of cohesin.

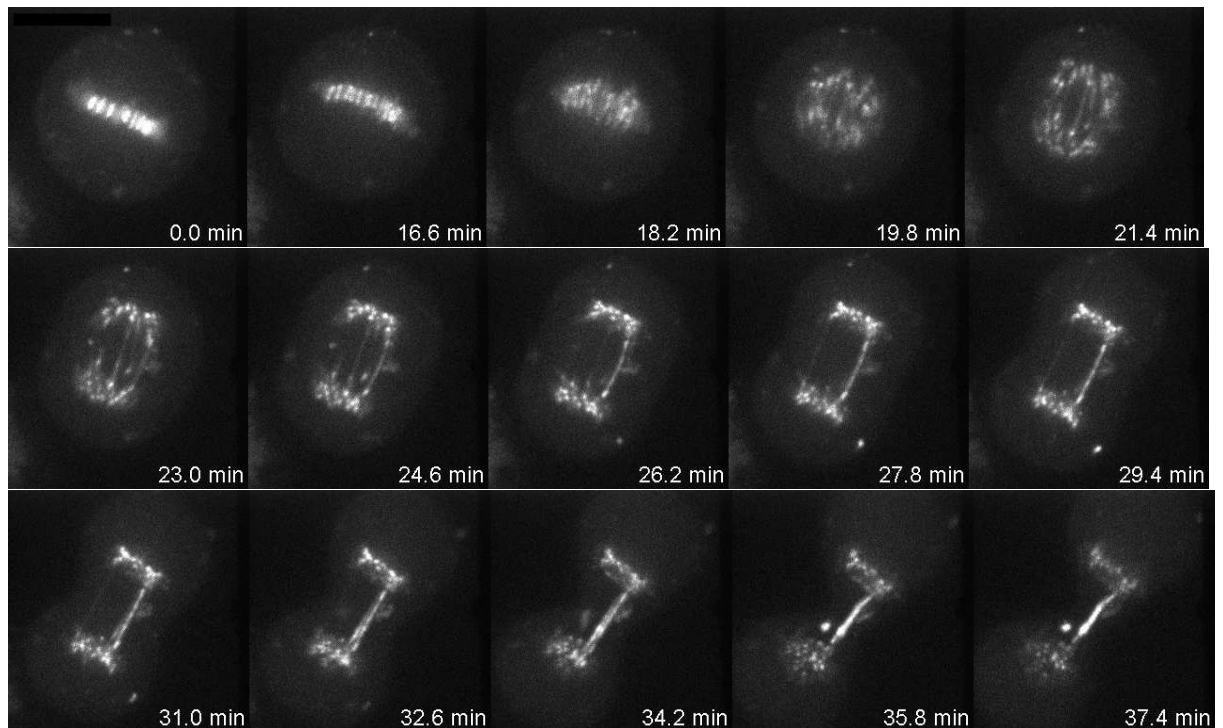


Figure 17.5: Walker A mutant cell, having ATPase deficient non-endogenous PICH mutant prolongs chromosome separation significantly.

CHAPTER 18

Outlook

In this section of my thesis the involvement of PICH during chromosome segregation could be shown with live-cell imaging. With additional biochemical assays conducted in the Nigg lab, we showed that PICH plays a crucial role in the proper segregation of sister chromatids. Only with the sensitivity of the SDM at high speeds, could the faint signals of PICH associated DNA threads be visualised *in vivo* so that the dynamics of the PICH threads could be elucidated.

The next step involves the marking of TOPOII with PICH to see whether TOPOII is the partner in thread ripping, similar to the role of TOPOII in onset of anaphase. Currently the maximum time resolution we could achieve was about two seconds due to the high stack number that was necessary to resolve a complete thread. However, with a faster acquisition time, the time line of the ripping could be investigated more thoroughly. Moreover, DNA damage sensitive markers might show whether there is a controlled ripping or if the DNA strand is simply broken. From biochemical assays, it is expected that the DNA stays unharmed. Another point of interest is how the DNA resolves into its initial structure. It is possible that the DNA strand does not condense back to the chromosome but rather joins the chromatid structure shortly after anaphase. These experiments depend strongly on the dynamics of PICH. Dissociation of PICH prior to chromatid formation results in the reduction of fluorescence markers, making the experiment very difficult to conduct.

CHAPTER 19

Summary and Conclusion

The elucidation of dynamical processes on the cellular level was the main goal of this work. For this purpose, sensitive and technically demanding new methods have been developed. A tracking microscope was developed which tracks fluorescent particles in real-time. The system is able to track single particles with a precision down to 20nm and a time resolution of 16ms. From that data, dynamic processes can be analysed in terms of motional behaviour and velocities. Furthermore, a widefield setup was attached to the microscope which simultaneously observes the surroundings of the tracked particle. This enables the possibility to relate the obtained trajectory to the embedded structure. The system can also be used to maintain the focus on a specific labelled particle as large as the cell nucleus itself. The tracking system was tested and applied on microtubular movement and artificial refocussing of HuH7 cells.

The two further experiments were conducted using a spinning disc confocal microscope. The first experiment revealed the transport mechanism of localising mRNA in budding yeast. With the SDM, we obtained colocalised trajectories showing that different localising mRNA-species utilise the same transport machinery are also transported within the same vehicle.

In the second experiment, the ripping of DNA threads associating with PICH, a helicase involved in proper chromosome segregation was visualised. Here, the first live-cell image of the dynamics of PICH associated DNA threads showed that PICH is maintained on these threads and the threads themselves are maintained until late anaphase. Only then do the threads rip and become resolved to the centromeres.

Bibliography

- [1] S. ARONOV, R. GELIN-LICHT, G. ZIPOR, L. HAIM, E. SAFRAN, and J. E. GERST. mRNAs encoding polarity and exocytosis factors are cotransported with the cortical endoplasmic reticulum to the incipient bud in *Saccharomyces cerevisiae*. *Molecular and Cellular Biology*, 27(9): 3441–3455 (2007).
- [2] S. BACCHETTI and F. L. GRAHAM. Transfer of the gene for thymidine kinase to thymidine kinase-deficient human cells by purified herpes simplex viral DNA. *Proc. Natl. Acad. Sci.*, 74(4): 1590–1594 (1977).
- [3] C. BAUMANN, R. KÖRNER, K. HOFMANN and E. A. NIGG. Pich, a centromere-associated snf2 family ATPase, is regulated by plk1 and required for the spindle checkpoint. *Cell*, 128(1): 101–114 (2007).
- [4] H. C. BERG. How to track bacteria. *Review of Scientific Instruments*, 42(6): 868–871 (1971).
- [5] E. BERTRAND, P. CHARTRAND, M. SCHAEFER, S. M. SHENOY, R. H. SINGER and R. M. LONG. Localization of ash1 mRNA particles in living yeast. *Molecular Cell*, 2: 437–445 (1998).
- [6] E. BETZIG, G. H. PATTERSON, R. SOUGRAT, O. W. LINDWASSER, S. OLENYCH, J. S. BONIFACINO, M. W. DAVIDSON, J. LIPPINCOTT-SCHWARTZ and H. F. HESS. Imaging intracellular fluorescent proteins at nanometer resolution. *Science*, 313(5793): 1642–1645 (2006).
- [7] N. BOHR. On the constitution of atoms and molecules. *Philosophical Magazine*, 26: 1–25 (1913).
- [8] M. BORN and E. WOLF. Principles of Optics. *Cambridge University Press*, 7th Ausgabe (1999).
- [9] O. BURKACKY. CARS-Mikroskopie und Aufbau sowie Charakterisierung einer Apparatur zur dreidimensionalen Verfolgung von Einzelobjekten in Echtzeit. Ph.D. thesis, Ludwig-Maximilians-Universität München (2007).

- [10] E. CONDON. A theory of intensity distribution in band systems. *Physical Review*, 28: 1182–1201 (1926).
- [11] S. D. CONNER and S. L. SCHMID. Regulated portals of entry into the cell. *Nature*, 422: 37–44 (2003).
- [12] K. DE BRUIN, N. RUTHARDT, K. VON GERSDORFF, R. BAUSINGER, E. WAGNER, M. OGRIS and C. BRÄUCHLE. Cellular dynamics of egf receptor-targeted synthetic viruses. *Molecular Therapy*, 15(7): 1297–1305 (2007).
- [13] W. DENK, J. H. STRICKLER and W. W. WEBB. Two-photon laser scanning fluorescence microscopy. *Science*, 248(4951): 73–76 (1990).
- [14] D. EGGER, R. BOLTEN, C. RAHNER and K. BIENZ. Fluorochrome-labeled rna as a sensitive, strand-specific probe for direct fluorescence in situ hybridization. 111(4): 319–24 (1999).
- [15] J. ENDERLEIN. Tracking of fluorescent molecules diffusing within membranes. *Appl. Phys. B*, 71: 773–777 (2000).
- [16] J. FRANCK. Elementary processes of photochemical reactions. *Transactions of the Faraday Society*, 21: 536–542 (1925).
- [17] T. FÖRSTER. Zwischenmolekulare energiewanderung und fluoreszenz. *Annalen der Physik* 6, 437(1-2): 55–75 (1948).
- [18] W. GÖBEL, B. M. KAMPA and F. HELMCHEN. Imaging cellular network dynamics in three dimensions using fast 3d laser scanning. *NATURE METHODS*, 4(1): 73–79 (2007).
- [19] M. GÖPPERT-MAYER. Über elementarakte mit zwei quantensprüngen. *Annalen der Physik*, 401(3): 273–294 (1931).
- [20] L. HAYFLICK. The limited in vitro lifetime of human diploid cell strains. *Experimental Cell Research*, 37: 614–36 (1965).
- [21] R. HEIM, A. B. CUBITT and R. Y. TSIEN. Improved green fluorescence. *Nature*, 373: 663–664 (1995).
- [22] S. W. HELL and J. WICHMANN. Breaking the diffraction resolution limit by stimulated emission: stimulated-emission-depletion fluorescence microscopy. *Opt. Lett.*, 19: 780–782 (1994).
- [23] K. HENKEL. Die Mikrofibel. <http://www.mikroskopie-muenchen.de> (2003).

- [24] Z. L. HORVÁTH and Z. BOR. Focusing of truncated gaussian beams. *Optics Communications*, 222: 51–68 (2003).
- [25] A. JABŁONSKI. über den mechanismus der photolumineszenz von farbstoffphosphoren. *Nature*, 131(839): 38–46 (1935).
- [26] R.-P. JANSEN. mrna localization: message on the move. *Nature Reviews Molecular Cell Biology*, 2: 247–256 (2001).
- [27] W. KAISER and C. GARRETT. Two-photon excitation in $\text{CaF}_2: \text{Eu}^{2+}$. *Phys.Rev.Lett.*, 7: 229–231 (1961).
- [28] R. KALMAN. A new approach to linear filtering and prediction problems. *Journal of Basic Engineering*, 82(D): 35–45 (1960).
- [29] Z. KAM, D. A. AGARD and J. W. SEDAT. Three-dimensional microscopy in thick biological samples: a fresh approach for adjusting focus and correcting spherical aberration. *Bioimaging*, 5: 40–49 (1997).
- [30] A. KAPANIDIS, N. LEE, T. LAURENCE, S. DOOSE, E. MARGEAT and S. WEISS. Fluorescence-aided molecule sorting: Analysis of structure and interactions by alternating-laser excitation of single molecules. *PNAS*, 101: 8936–8941 (2004).
- [31] A. KÖHLER. Ein neues beleuchtungsverfahren für mikrographische zwecke. *Zeitschrift für Mikroskopie*, X: 433–440 (1893).
- [32] K. KIS-PETIKOVA and E. GRATTON. Distance measurement by circular scanning of the excitation beam in the two-photon microscope. *Microscopy Research and Technique*, 63: 34–49 (2004).
- [33] T. A. KLAR, S. JAKOBS, M. DYBA, A. EGNER and S. W. HELL. Fluorescence microscopy with diffraction resolution barrier broken by stimulated emission. *PNAS*, 97(15): 8206–8210 (2000).
- [34] V. LEVI, Q. RUAN and E. GRATTON. 3-d particle tracking in a two-photon microscope: Application to the study of molecular dynamics in cells. *Biophysical Journal*, 88: 2919–2928 (2005).
- [35] V. LEVI, Q. RUAN, K. KIS-PETIKOVA and E. GRATTON. Scanning fcs, a novel method for three-dimensional particle tracking. *Biochemical Society Transactions*, 31: 997–999 (2003).
- [36] E. LOMMEL. Die beugungserscheinungen einer kreisrunden öffnung und eines kreisrunden schirmchens. *Abh. Bayer. Akad. Math. Naturwiss. Kl.*, 15: 229–328 (1885).

- [37] D. MAGDE, E. ELSON and W. W. WEBB. Thermodynamic fluctuations in a reacting system - measurement by fluorescence correlation spectroscopy. *Phys. Rev. Lett.*, 29(11): 705–708 (1972).
- [38] T. H. MAIMAN. Stimulated optical radiation in ruby. *Nature*, 187: 493–494 (1960).
- [39] A. MARGEOT, C. BLUGEON, J. SYLVESTRE, S. VIALETTE, C. JACQ and M. CORRAL-DEBRINSKI. In *saccharomyces cerevisiae*, atp2 mrna sorting to the vicinity of mitochondria is essential for respiratory function. *The EMBO Journal*, 21(24): 6893–6904 (2002).
- [40] G. NOMARSKI and A. WEILL. Application à la métallographie des méthodes interférentielles à deux ondes polarisées. *Rev. Metall.*, 2: 121–128 (1955).
- [41] R. J. OBER, S. RAM, and E. S. WARD. Localization accuracy in single-molecule microscopy. *Biophysical Journal*, 86: 1185–1200 (2004).
- [42] M. OGRIS, S. BRUNNER, S. SCHÜLLER, R. KIRCHEIS and E. WAGNER. Pegylated dna/transferrin-pei complexes: reduced interaction with blood components, extended circulation in blood and potential for systemic gene delivery. *Gene Therapy*, 6(4): 595–605 (1999).
- [43] M. ORMO, A. CUBITT, K. KALLIO, L. GROSS, R. TSIEN and S. REMINGTON. Crystal structure of the *aequorea victoria* green fluorescent protein. *Science*, 273: 1392–1395 (1996).
- [44] J. B. PAWLEY, editor. Handbook of Biological Confocal Microscopy. *Springer*, 3 Ausgabe (2006).
- [45] W. RASBAND. Imagej, u. s. national institutes of health, bethesda, maryland, usa., <http://rsb.info.nih.gov/ij/> (1997-2007).
- [46] M. J. RUST, M. BATES and X. ZHUANG. Sub-diffraction-limit imaging by stochastic optical reconstruction microscopy (storm). *Nature Methods*, 3: 793–796 (2006).
- [47] A. SACCHETTI, V. SUBRAMANIAM, T. M. JOVIN and S. ALBERTI. Oligomerization of dsred is required for the generation of a functional red fluorescent chromophore. *FEBS Letters*, 525(1-3): 13–19 (2002).
- [48] M. J. SAXTON and K. JACOBSSON. Single-particle tracking: Applications to membrane dynamics. *Annu. Rev. Biophys. Biomol. Struct.*, 26: 373–99 (1997).
- [49] A. L. SCHAWLOW and C. H. TOWNES. Infrared and optical masers. *Phys. Rev.*, 112(6): 1940–1949 (1958).

- [50] M. SCHMID, A. JAEDICKE, T.-G. DU and R.-P. JANSEN. Coordination of endoplasmic reticulum and mrna localization to the yeast bud. *Current Biology*, 16(15): 1538–1543 (2006).
- [51] K. A. SHEPARD, A. P. GERBER, A. JAMBHEKAR, P. A. TAKIZAWA, D. H. P. O. BROWN, J. L. DERISI and R. D. VALE. Widespread cytoplasmic mrna transport in yeast: identification of 22 bud-localized transcripts using dna microarray analysis. *PNAS*, 100(20): 11429–11434 (2003).
- [52] O. SHIMOMURA, F. H. JOHNSON and Y. SAIGA. Extraction, purification and properties of aequorin, a bioluminescent protein from the luminous hydromedusa, *Aequorea*. *Journal of Cellular and Comparative Physiology*, 59(3): 223–239 (1962).
- [53] G. STOKES. On the change of refrangibility of light. *Philosophical Transactions of the Royal Society of London*, 142: 463–562 (1852).
- [54] H. STÜBEL. Die fluoreszenz tierischer gewebe in ultraviolettem licht. *Pflüger's Archiv für Physiologie.*, 142: 1–14 (1911).
- [55] P. A. TAKIZAWA and R. D. VALE. The myosin motor, myo4p, binds ash1 mrna via the adapter protein, she3p. *PNAS*, 97: 5273–5278 (2000).
- [56] J. C. WANG. Interaction between dna and an escherichia coli protein omega. *J Mol Biol.*, 55(3): 523–33 (1971).

Appendix: Materials and Assays

Equipment

Table 19.1: Technical Equipment Confocal Tracking Microscope

Equipment	Company
PMJ-A3A-3AF-633-4/125-3-5-1 fibre	AMS technologies
HPUC-2,A3A-633-P-5AS-12 coupler	AMS technologies
HPUCO-23AF-400/700-P-30AC collimator	AMS technologies
MMJ-3S3S-IRVIS-50/125-3-1:OZ fibre patchcord	AMS technologies
MMJ-3S3S-IRVIS-100/140-3-1	AMS technologies
Objective Heater ϕ 29.0mm Nikon	PeCon
SPCM-AQR-16 -14	EG&G;Laser Components AMS Tech
Sapphire 488	Coherent
JiveTM laser 25mW lab 561nm	Cobolt AB
Mirrors	Linos
ScanIM	Maerzhaeuser
633nm 5mW HeNe laser	Melles Griot
Optical Breadboard	Melles Griot
NI PCI-6036E	National Instruments
NI PCI-6733	National Instruments
2x BNC-2090	National Instruments
2x SH6868-EP	National Instruments
Plan Apo 60x/1.20 WI Objective	Nikon
LabTek 8well slide	Nunc
SPCM-AQR- CD-3017	Perkin Elmer
S-334.2SL Piezo Tip-Tilt Platform	Physik Instrumente
E-500.00 Chassis	Physik Instrumente
E-503.00S LVPZT amplifier	Physik Instrumente

...continued on next page

Table 19.1 – continued from previous page

Equipment	Company
E-509.S3 Sensor/Servo Controller, DMS	Physik Instrumente
E-808.90 Monitorcable for E-809	Physik Instrumente
MIPOS 100PL CAP	Piezosystem Jena
NV 40/1 CL	Piezosystem Jena
Adapter M25x0.75/W0.8x1/36" (RMS)	Piezosystem Jena
Adapter W0.8x1/36" for MIPOS 100	Piezosystem Jena
Max313-M 3-Axis NanoMax	Thorlabs
posts and postholders if not differently labelled	Coherent
optical components, cage, tubes, lenses	Thorlabs
BFH22-365-CUSTOM fibre	Thorlabs
M31L01 1m FC Patch cable 62.5 μ m	Thorlabs
LS3ZM2	Uniblitz
Glaskasten nach Hauser	VWR
Faerbegestell nach Hauser fuer 30-60 Objekttraeger	VWR
Zeiss Axiovert 200	Zeiss
1951 USAF Resolution Test Chart	Zeiss
EC Plan-Neofluar 63x/0.95 Korr	Zeiss
Eye Piece Reticular	Zeiss
TempControl 37-2 digital	Zeiss

Table 19.2: Filters used for Confocal Tracking Microscope

Identifier	Company
q630SPXR	AHF Analysentechnik
633-765DCRB	AHF Analysentechnik
50/50T VIS	AHF Analysentechnik
Mirror 98.5%	AHF Analysentechnik
z488RDC	Chroma
z488/561 Beamsplitter	Chroma
hq600/40	Chroma
z532/635	Chroma
hq695/100 Notch Filter	Chroma
hc562 Beamsplitter	Semrock
hc520/35 Notch Filter	Semrock

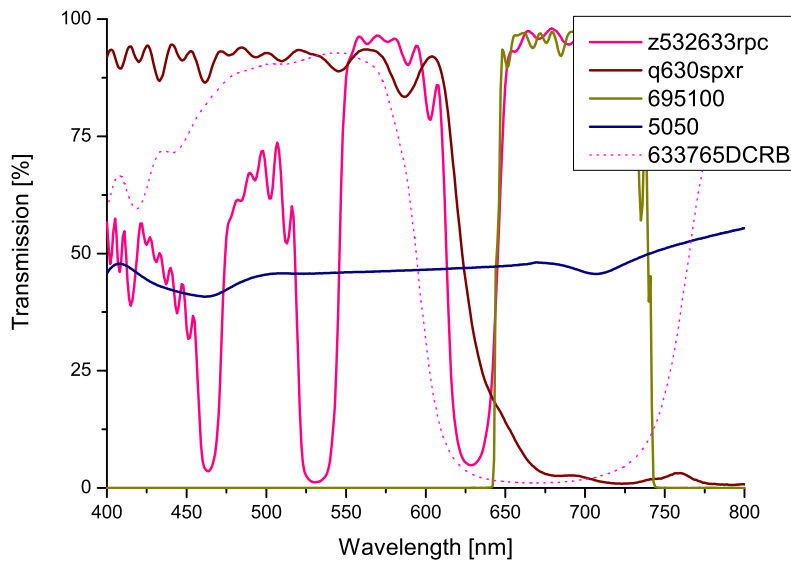


Figure 19.1: Transmission Spectra of Filters used for the Confocal Tracking

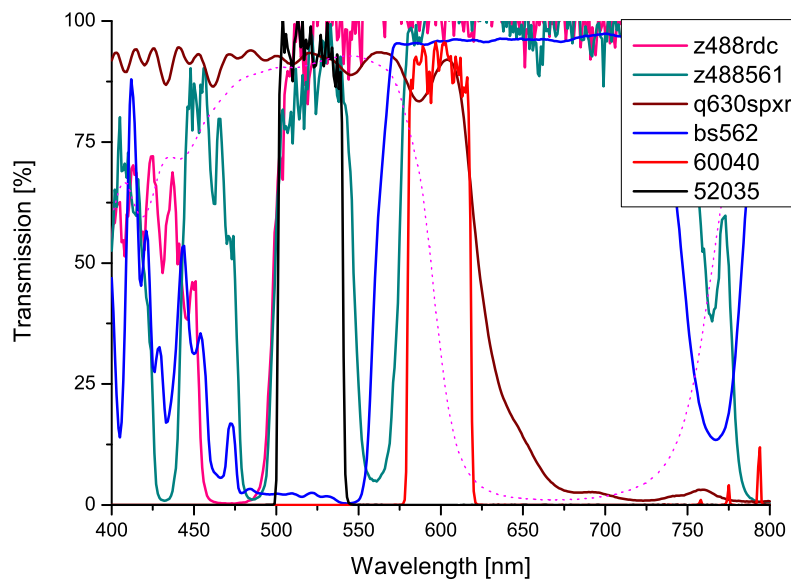


Figure 19.2: Transmission Spectra of Filters used for the Widefield Tracking

Table 19.3: Technical Equipment for Spinning Disc Microscope

Identifier	Company
TE2000E	Nikon
100x NA 1.49 Oil TIRF	Nikon
OptoSplit II	Cairn Research
DU-897 iXon+	Andor
Revolution System	Andor
CSU10	Yokogawa
Cube	Coherent
Sapphire	Coherent
Jive™ laser 25mW lab	Cobolt
NanoScanZ	Prior Scientific
AOTF	AA Opto-Electronic

Table 19.4: Filters used for Spinning Disc Microscope

Identifier	Company
Di01-T405/488/568/647	Semrock
NF01-405/488/561/635	Semrock
hc562 Beamsplitter	Semrock
hc513/17 Bandpass	Semrock
hq525/50 Bandpass	Chroma
et605/70 Bandpass	Chroma

Table 19.5: Fluorescent Probes and Samples

Identifier	Company
Atto 488	LS Labor Service
Cy3	Probes
Cy5	LS Labor Service
Syto Kit - 17 and 59-64	Invitrogen
Focalcheck Microspheres, 6 μ m, green/dark-red ring	Invitrogen
Focalcheck Microspheres Kit, 1.0 μ m	Invitrogen
Multi-fluorophor, Polystyrene Particles, 170nm	Spherotech/Kisker
TDI	Milli-Q Plus Filter
Fluorescing Microscope Slides	Chroma/AHF
FluoSpheres, 0.02 μ m, crimson fluorescent (625/645)	Invitrogen
GFP	Milli-Q Plus Filter

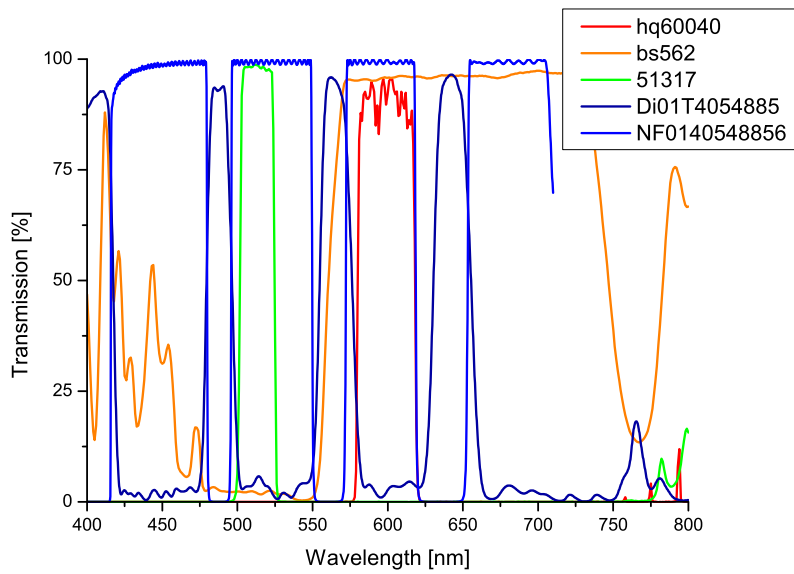


Figure 19.3: Transmission Spectra of Filters used for the mRNA Transport Experiments

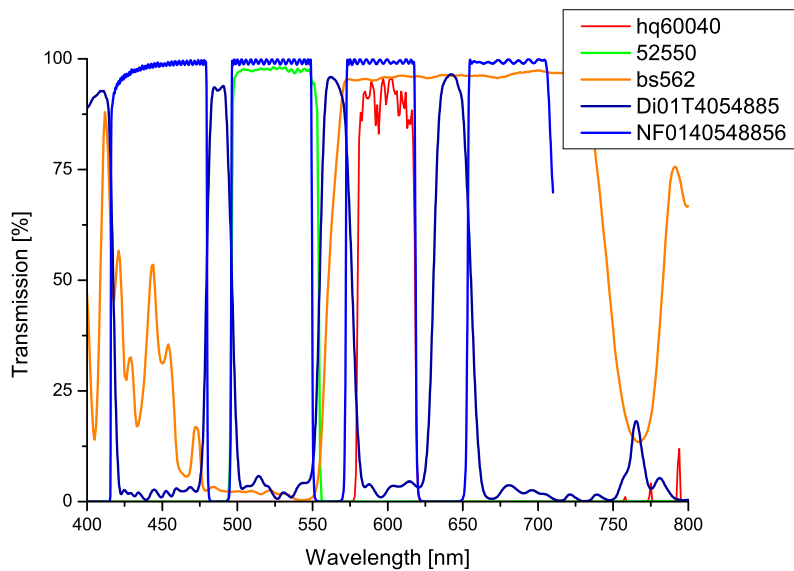


Figure 19.4: Transmission Spectra of Filters used for the PICH Experiments

Table 19.6: Consumables: Biochemistry and Cell Biology

Identifier	Company
Kottermann Wärmebad	BFi Optilas
HuH7 cells	JCRB 0403 Tokyo, Japan
kelvitron t Trockner	Semrock
IsoProp	Chroma
kelvitron t Trockner	Semrock
F-8782	Invitrogen
FP-0257-2	Spherotech
Ethanol 70%	LS Labor Service
Ethanol (reinst)	LS Labor Service
Glutaraldehyd 25% wässrige Lösung	Biochrom Sigma
Wasser	Milli-Q Plus Filter
MEM-EARLE Zellkulturmedium	Biochrom KAG
FCS	Biochrom AG
Trypsin/EDTA Lösung	PAN Systems
Isoton	Schärfe
PBS (w/o)	Biochrom AG
Helipur H plus N	Heiland
Deconex 11 universal	Borer Chemie

Table 19.7: Software and Programs

Identifier	Company
iQ 1.7	Andor
View5D plugin	www.nanoimaging.de/View5D/
MatLab 7	The MathWorks Inc.
Origin	Microcal
ImageJ 1.38x	National Institutes of Health
Labview 8.0	National Instruments
IMAQ Vision 7.0	National Instruments

Cookbook

Cleaning cover slides

To clean the glass slides for the spin coating the cover glasses of 50x20mm NO 1 were put on a holder (Dyeframe after Hauser). The holder was then covered with 600ml milipore simplicity 185 water mixed with 3 ml Helmanex II. The sample was heated to 83 degrees celsius and left for 30 minutes. Thereafter the heater was switched off and the cover glasses sonicated for another 3 minutes. The holder together with the cover glasses was then washed under deionized water and left for drying.

Spin Coating

For spincoating beads a cleaned cover glass was put on a spin coater. 20 μ l of the bead sample was injected on the cover glass rotating at 150 times per minute and left for at least 30 minutes until the glass was dry.

The autocorrelation sample

An Atto 647N sample with a 2nmol concentration was used for the system alignment. A cover glass of 24x32mm NO 1.5 was taken and shortly cleaned in a flame (IBS Integra Biosciences, Fireboy eco). Two double faced adhesive strips were put on the cover glass on the shorter edge in such a way, that a small gap of 2 mm was in the centre between the two strips. Another 20x20mm NO # 1.5 cover glass was also cleaned and put on the tape. A small channel remained in that way. Approximately 3.5 μ l of the 2nM Atto 647N sample was then filled into the channel and sealed with melted paraffin.

Syto Staining

1.5h prior experiment 200 μ l of medium was replaced with a 500nM Syto61 solution in DMSO. About 2h later, the Syto61 was uptaken by the cell and stained nucleic acids. To minimise background signal from particles in solution, the cells were washed twice with medium.

Beam Walking

Beam walking describes a method to adjust a laser with two mirrors. Hereby the mirror further apart was slightly adjusted out and the second corrected for the deviation. If the intensity of the beam was improved one repeats the process until the intensity decreased. By this means the beam is not only adjusted in the angular but also in the correct position. Only with two mirrors one can achieve a parallel shifting of a beam.

Single Mode Fibre Coupling

First the laser was roughly guided into the fibre by eye. Eventually the fibre itself could be unmounted and one could assure a centred and perpendicularly entering beam. Thereafter the fibre was softly mounted not reaching the endpoint of the coupler. The

focussed laser spot was then slightly out of focus and thus larger in size. By increasing the laser intensity to the maximum of the laser output of about 25mW the laser could easier hit the fibre core which is typically in the range of 8 to 10 */microm* for single mode fibres. Now the other end of the fibre was pointed on a piece of white paper to inspect for an already transmitted laser beam. It was hereby helpful to proceed in a dark room where the eye was already adapted to the light conditions, as the faint laser signal could be detected easier. The two mirrors on the entering site the laser could be adjusted to a maximum laser output on the other side by beam walking. If the maximum was reached the fibre was then further pushed into the coupler and the intensity maximisation repeated until the fibre finally hit the endpoint of the coupler.

Köhler Alignment

For the Köhler alignment the sizes of the two apertures, the position of the condensor or field aperture and the distance of the condensor to the sample has to be adjusted. The Köhler configuration alignment is dependent on the objectives and thus has to be repeated whenever the objective is changed. First a sample has to be mounted on the microscope and be focussed. It has to be considered to use an eye piece reticular in case of ametropia. Hereby the eye piece reticular is being adjusted with a corrector collar at the ocular to ensure a proper focus plane on the sample. When the sample is in focus, the field aperture is closed, so that the shape of the aperture can be seen. The condensor must then be moved along the optical axis, so that the aperture image is focussed. This diaphragm has then to be centred with screws attached to the aperture on the condensor. Subsequently the field aperture is opened, that the observed field is clearly visible and is not obstructed by the diaphragm. It should not be opened more than that to minimise additional straylight sources coming from illuminated parts other than those in the field of view. Now with the second aperture the NA of the incident light can be adjusted. It is suggested to open the aperture to 2/3s of the maximum opening.

DIC Alignment

A prerequisite of the Difference Interference Contrast Alignment is the proper alignment of the microscope according to Köhler. If the alignment and the correct parts for the DIC including the correct DIC prism is given, the adjustment is rather simple. First both prisms have to be taken out. The axis of the polariser and the analyser must be at 90 degrees, that no light is transmitted. Usually only the polariser can be rotated. To assure that position one either has to look for the least intense position if one looks through the ocular or to the back focal plane (take out ocular, or use Bertrand lens), a dim black cross has to appear. The DIC prisms are then inserted and finally the image post-adjusted with the polariser.

Abbreviations

<i>ACF</i>	Autocorrelation Function
<i>AOM</i>	Acousto-Optical Modulator
<i>AOTF</i>	Acousto-Optical Tunable Filter
<i>APD</i>	Avalanche Photo Diode
<i>ATP</i>	Avalanche Photo Diode
<i>CP</i>	Coat Protein
<i>CPU</i>	Central Processing Unit
<i>CW</i>	Continuous Wave
<i>DIC</i>	Differential Interference Contrast Microscopy
<i>DNA</i>	Deoxyribonucleic Acid
<i>E.Coli</i>	Escherichia Coli
<i>EGF</i>	Epidermal Growth Factor
<i>ER</i>	Endoplasmatic Reticulum
<i>EMCCD</i>	Electron Multiplying Charge Coupled Device
<i>FCS</i>	Fluorescence Correlation Spectroscopy
<i>FCCS</i>	Fluorescence Cross-Correlation Spectroscopy
<i>FFT</i>	Fast Fourier Transformation
<i>FISH</i>	Fluorescence In-Situ Hybridisation
<i>FPGA</i>	Field Programmable Gate Array
<i>FWHM</i>	Full Width at Half Maximum
<i>GFP</i>	Green Fluorescent Protein
<i>GPD</i>	Glucose-6-Phosphate Dehydrogenase.
<i>HBG</i>	HEPES Buffered Glucose
<i>HeLa</i>	Cervical Cancer Cells extracted from Henrietta Lacks
<i>HEPES</i>	2-(4-(2-Hydroxyethyl)-1-piperazinyl)-ethansulfonic acid
<i>HSV</i>	Herpes Simplex Virus
<i>ICCD</i>	Intensified CCD
<i>IR</i>	Infrared
<i>LASER</i>	Light Amplification by Stimulated Emission of Radiation

...continued on next page

— continued from previous page

<i>LMU</i>	Ludwig-Maximilians-Universität
<i>LSM</i>	Laser Scanning Microscope
<i>MET</i>	Methionine
<i>msALEX</i>	milisecond Alternating Laser Excitation
<i>MSD</i>	Mean Square Displacement
<i>NA</i>	Numerical Aperture
<i>NI</i>	National Instruments
<i>NLS</i>	Nuclear Localisation Signal
<i>ORF</i>	Open Reading Frame
<i>ORI</i>	Origin Of Replication
<i>PEI</i>	Polyethylenimine
<i>PEG</i>	Polyethylene glycol
<i>PEP</i>	Peptide
<i>PH</i>	Pinhole
<i>pH</i>	pH value (pondus or potentia hydrogenii)
<i>PICH</i>	Plk1-Interacting Checkpoint Helicase
<i>PLK</i>	Polo-Like Kinase
<i>PMT</i>	Photo Multiplier Tube
<i>POL</i>	Polymerase
<i>PP</i>	Phosphatase
<i>PSF</i>	Point Spread Function
<i>RFP</i>	Red Fluorescent Protein
<i>RNA</i>	Ribonucleic Acid
<i>RNP</i>	Ribonucleo Protein
<i>ROI</i>	Region Of Interest
<i>S/N</i>	Signal to Noise
<i>SAC</i>	Spindle Assembly Checkpoint
<i>SDM</i>	Spinning Disc Confocal Microscope
<i>SGO</i>	Shugoshin
<i>STED</i>	Stimulated Emission Depletion
<i>THR</i>	Threonine
<i>TIRF</i>	Total Internal Reflection Fluorescence (Microscopy)
<i>TTL</i>	Transistor-Transistor Logic
<i>UTR</i>	Untranslated Region
<i>UV</i>	Ultraviolet
<i>WI</i>	Water Immersion
<i>YFP</i>	Yellow Fluorescent Protein

Publications

Susanne Lange, Yoshihiko Katayama, Maria Schmid, Ondrej Burkacky, Christoph Bräuchle, Don C. Lamb, and Ralf-Peter Jansen, *Simultaneous transport of different localized mRNA species revealed by live-cell imaging*. *Traffic* (2008)

Lily Wang, Yoshihiko Katayama, Don C. Lamb, and Erich Nigg *PICH promotes centromere DNA resolution by Topoisomerase-II α in anaphase*. *Nature Cell Biology* (submitted)

Yoshihiko Katayama, Ondrej Burkacky, Don C. Lamb and Christoph Braeuchle, *A novel 3D tracking microscope*. in preparation

Acknowledgements

I am indebted for the enormous amount of support, encouragement and advice I have received during this thesis. I would like to thank Prof. Don C. Lamb for his dedicated supervision of my thesis and for supporting my scientific progress. Also I would like to thank him for the thorough correction of my thesis. I would also like to thank Prof. Christoph Bräuchle for giving me the opportunity to work in our very rewarding group. My gratitude belongs to Prof. Achim Hartschuh for the warm advices and also for reviewing my thesis.

I would also like to thank Prof. Regina de Vivie-Riedle and Prof. Jens Michaelis for their support at the end of my PhD.

This work would not have been possible without the help of all current and former members of the group of Prof. Bräuchle and subgroups. In particular Ondrej, Adam for their direct support of my work, but also Peter, Alex, Stephan, Tatas, Susanne, Andreas, Philipp, Nadia, Timo, Christophe, Florian, Johanna, Barbara, Stefan, Florian, Kevin, Karla, Agi, Caro, Anna, Julia, Malte, Sebastian and the other Sebastian. But also Bärbel, Robert, Asia, Wolfgang, Susanne, Johann, Gregor, Franziska, Martin, Martina, Jens, Thomas, John, Stefan, Thomas, Doro, Sergey, Vova, Peter, Monika, Matthias, Niko, Franziska, Ralf, Bente, Anna, Tanvi, Moritz, Wolfgang and Fr. Steger for an enjoyable working atmosphere and companionship throughout. I am deeply thankful for everyone's talent and backup.

The work was in close relationship with the people from the LFD, the Laboratory of Fluorescence Dynamics now at the University of California in Irvine from Prof. Enrico Gratton. It was a pleasure and an honour to work with you, Enrico, Susana, Chip, Courtney, Enrico, Jay, Michelle, Valeria, Antonius, Taras and also Hell, who is also former member of Bräuchle's.

Many collaborators have contributed to the work, in particular Susanne Lange and Prof. Jansen from the Gene Center in Munich, which resulted in an fruitful and enjoyable cooperation covering part II of this thesis. I am deeply grateful for their support and kind patience in leading me into yeast biology.

I would also like to thank Mrs. Wang from the Max-Planck Institute for Biochemistry of the group of Prof. Erich Nigg for the instructive cooperation which resulted in the work presented in part III.

I am much obliged for the contributions of many workers from the workshop. The mechanical workshop in particular Mr. Leeb, Mr. Straube, Mr. Hiermayer and Mr. Bartel. From the electronical workshop, Mr. Gersdorf, Mr. Bachmeier and Mr. Skritic.

I was lucky to have wonderful and talented interns namely Veronika Zinth, Tobias Blümke and Moritz Haag. Thank you for your help.

For smaller but nevertheless inspiring coworking, I would like to thank Mr. Zayhikov for the introduction to HPLC, Mr. Meyer for the synthesis of the DNA polyplexes and Mr. Senghaas for the introduction to their aquarium.

I am grateful to all the students who taught me thinking of better ways to teach and for nice and great experiences.

I'd like to express my gratitude to numerous companies:

Mrs. Nolde and Mr. Hegenbarth from Thorlabs, Mr. Sommerauer and Mr. Braunwarth from AHF Analysentechnik, Mr. Haunert from BFI Optilas, Mr. Pöttinger from Zeiss, Mr. Stüven from Olympus, Mr. Schwartz and Mr. Nettesheim from Nikon, Mr. Browne and Mr. Wainwright from Andor Scientific, Mr. Palumbo from ARP Datacon, Mr. Manus from Soliton, Mr. Hinz from Melles Griot, Mr. von Gegerfelt from Cobolt AB, Mr. Schneider from Piezosystem Jena and Mr. Jerger from Physik Instrumente.

This work was financially supported by the DFG Sonderforschungsbereich (SFB) 647, the Center for NanoScience (CeNS), the Nanosystems Initiative Munich (NIM) and the BioImaging Network (BIN)

Finally I bow before my friends and family for their continuous encouragement and happy moments. Thank you for so many wonderful laughs!